Brachiating Power Line Inspection Robot

Controller Design and Implementation

Presented by:
Lindokuhle Shongwe

Prepared for:
Professor E. Boje

Submitted to the Department of Electrical Engineering at the University of Cape Town in fulfilment of the academic requirements for a Master of Science degree in Electrical Engineering

February 21, 2021

Declaration

1. I know that plagiarism is wrong. Plagiarism is to use another's work and pretend that it is one's own.
2. I have used the IEEE convention for citation and referencing. Each contribution to, and quotation in, this report from the work(s) of other people has been attributed, and has been cited and referenced.
3. This report is my own work.
4. I have not allowed, and will not allow, anyone to copy my work with the intention of passing it off as their own work or part thereof.

Signature:... Signed by candidate .
Lindokuhle Shongwe

Date:. 01 March 2021 ...

Acknowledgements

The work presented in this dissertation would not be possible without the unwavering support of the key individuals and organisations.

To my supervisor, Professor E. Boje, your seemingly endless knowledge and ability to reason through every problem I brought to you has been a source of great inspiration. Our weekly meetings added a tremendous amount of value to this project; to my development as a researcher. It has been a journey, and I am truly grateful for all your guidance, support and mentorship.

To my parents and family, it is done! Thank you for your financial, emotional and spiritual support through the journey of this MSc. Your words of encouragement brought me great comfort and motivation to see this project through. Thank you for your endless sacrifices which have afforded me the education I have received over my academic career.

To my friends, who endured most of my bickering and whining throughout the past two years, thank you. Thank you for your words of support and believing in me when I no longer believed in myself.

To all my colleagues in the Mechatronics lab. It has been an honour to share the same lab space with you. Thank you for always lending a hand or sharing your knowledge whenever a problem arose - sometimes even abandoning your own research to help out.

This research would not have been possible without the support of the Mandela-Rhodes Foundation. The scholarship has, more than anything, inspired me to be the most authentic version of myself. Thank you for your guidance, support and continual investment in my aspirations and dreams of a better African continent.

Abstract

The prevalence of electrical transmission networks has led to an increase in productivity and prosperity. In 2014, estimates showed that the global electric power transmission network consisted of 5.5 million circuit kilometres (Ckm) of high-voltage transmission lines with a combined capacity of 17 million mega-volt ampere. The vastness of the global transmission grid presents a significant problem for infrastructure maintenance. The high maintenance costs, coupled with challenging terrain, provide an opportunity for autonomous inspection robots.

The Brachiating Power Line Inspection Robot (BPLIR) with wheels [73] is a transmission line inspection robot. The BPLIR is the focus of this research and this dissertation tackles the problem of state estimation, adaptive trajectory generation and robust control for the BPLIR.

A kinematics-based Kalman Filter state estimator was designed and implemented to determine the full system state. Instrumentation used for measurement consisted of 2 Inertial Measurement Units (IMUs). The advantages of utilising IMUs is that they are less susceptible to drift, have no moving parts and are not prone to misalignment errors. The use of IMU's in the design meant that absolute angles (link angles measured with respect to earth) could be estimated, enabling the BPLIR to navigate inclined slopes.

Quantitative Feedback Control theory was employed to address the issue of parameter uncertainty during operation. The operating environment of the BPLIR requires it to be robust to environmental factors such as wind disturbance and uncertainty in joint friction over time. The resulting robust control system was able to compensate for uncertain system parameters and reject disturbances in simulation.

An online trajectory generator (OTG), inspired by Raibert-style reverse-time symmetry[10], fed into the control system to drive the end effector to the power line by employing brachiation. The OTG produced two trajectories; one of which was reverse time symmetrical and; another which minimised the perpendicular distance between the end gripper and the power line. Linear interpolation between the two trajectories ensured a smooth bump-less trajectory for the BPLIR to follow.

Contents

List of Figures

List of Tables

Nomenclature

Abbreviations

F	Decision weighting factor
AWBT	Anti-windup bumpless transfer
BPLIR	Brachiating Power Line Inspection Robot
D	Duty Cycle
IMU	Inertial Measurement Unit
PWM	Pulse Width Modulation

Controller Design

F	Pre-filter
K	Feedback controller
P	Plant
X	High gain AWBT feedback
ζ	System zero dynamics
r_{CoM}	radial distance to centre of mass

System Model

$\mathbf{C}$	Coriolis matrix
$\mathbf{M}$	Mass matrix
$\mathbf{g}$	Gravity vector
$\boldsymbol{\phi}$	vector of external forces
$\boldsymbol{\tau}$	Torque vector
$\mathbf{f}$	Friction force vector
$\mathbf{q}$	Vector of generalised coordinates
η_g	Maximum gearbox efficiency
η_m	Maximum motor efficiency
ω_i	Angular velocity of i$^{\text{th}}$ link
ρ_{air}	Mass density of air
θ_i	Angle of i$^{\text{th}}$ link
$\tilde{f}$	Friction approximation
A	Cross sectional area
C_d	Drag coefficient
f_c	Coulomb friction
f_v	Viscous friction
g	Gravitational acceleration
I_i	Inertia of i$^{\text{th}}$ link
i_{ref}	reference current

K_m	Motor torque constant
L	Lagrangian
l_i	length of i^{th} link
l_{c_i}	Distance to CoM of i^{th} link

m_i	Mass of i^{th} link
T	Kinetic energy
V	Potential energy

State Estimation

$\mathbf{K}_k$	Kalman gain matrix
$\mathbf{M}_o$	Observability Matrix
$\mathbf{P}_k$	Error covariance matrix
$\mathbf{Q}_k$	Process noise covariance matrix
$\mathbf{R}_k$	Measurement noise covariance matrix
$\mathbf{V}_k$	Jacobian matrix of output map function w.r.t measurement noise
$\mathbf{W}_k$	Jacobian matrix of state transition function w.r.t process noise
$\tilde{\boldsymbol{\mu}}$	Accelerometer measurement vector
$\tilde{\boldsymbol{\mu}}$	Gyroscope measurement vector

$\hat{\mathbf{x}_k}$	*posterior* state estimate vector
$\hat{\mathbf{x}_k}^-$	*a priori* state estimate vector
$\boldsymbol{f}$	Continuous-time state transition vector function
$\boldsymbol{f}_d$	Discrete-time state transition vector function
$\mathbf{d}$	System vector output map
$\mathbf{z}$	Measurement vector
σ_{n_μ}	Accelerometer noise density
σ_{n_ω}	Gyroscope noise density
E	Expectation operator
r_i	Location of IMU module on i^{th} link

Chapter 1

Introduction

The 21st century has ushered in an era of unprecedented technological developments, especially in the fields of robotics and autonomous systems. These autonomous robotic systems aim to replicate what humans do, starting with what are typically referred to as dull, dirty and dangerous jobs. These are jobs which either have a significant amount of repetition, require humans to operate in inhospitable environments such as mine shafts, work at extreme conditions with a high probability of near-fatal accidents or all the above.

The oft-cited advantages of automation are that it will result in fewer casualties caused by negligence or incompetence. Automation will also reduce the need for humans to perform extreme tasks resulting in a cost reduction due to fewer accidents, fatalities and increased efficiencies.

Figure 1.1: Image showing two men performing high-voltage live-wire inspection and maintenance at a high altitude [55]

Commercial electrical energy systems, or power grids, have been central to the advancement of society in this and the previous century. Since their inception around 1881, they have grown and evolved into behemoths across the globe. They form the backbone of many, if not all modern economies. The commercialisation of electricity has contributed to the the growth of a vast, interconnected network of overhead transmission lines that transport power to the consumer.

Conservative figures, in 2014, estimated the total of circuit kilometres of high-voltage power lines at around 5.5 million globally [80]. These lines span across varying geographies in places that are remote, inaccessible and sometimes inhospitable. The environmental conditions pose challenges especially for inspection and maintenance of such an extensive network which often requires crewed helicopter missions.

It is impractical and costly for these crewed missions to monitor and inspect every circuit kilometre of overhead high-voltage lines across the world. As such, most utilities only perform inspection or repairs after failure events have occurred like runaway countryside fires [59].

The vast number of issues presents unique opportunities and challenges for robots to autonomously inspect and communicate the health of the power line to a central control centre. Such a robot is the focus of this research.

1.1 Motivation and Background to the Study

Robotics for power line inspection and maintenance is a relatively new application for autonomous systems. It promises cost reductions and efficiencies which far outstrip current best practices which entail manned helicopter missions. The basis for this project was the brachiating power line inspection robot presented by [70].

Brachiation is a form of locomotion employed by arboreal apes to swing from handhold to handhold in a canopy of trees. The proposed robot rides along a power line using actuated wrist motors and brachiates to overcome any obstacles it comes across while traversing the line.

The acrobot, which is similar to the Brachiating Power Line Inspection Robot (BPLIR), is used extensively in literature [20][27][28][30] as a benchmark system to demonstrate nonlinear control design. For the most part, the literature is concerned with the swing-up control problem which involves either driving the acrobot to, or stabilising it about, the vertically up unstable equilibrium point. Although this bodes well to demonstrate the

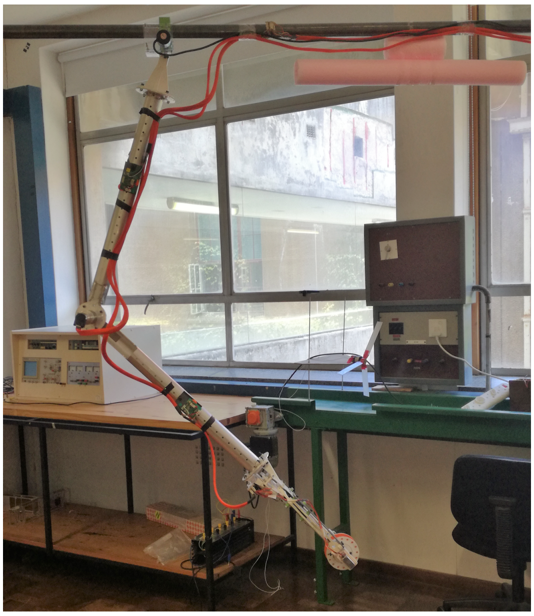

Figure 1.2: Image showing the existing mechanical prototype of a brachiating power line inspection robot

controllers, it does not deal with the problem of driving the acrobot from an unstable initial position to an unstable end position such as when brachiating.

Another consideration for this research is the issue of state estimation. Currently, encoders measure the angles of the links on the prototype shown in Figure 1.2. The main problem is that the relative encoders cannot provide full state measurement, i.e. relative encoders cannot directly measure the angle the fixed gripper makes with the power line (θ_1). This limitation means that the slope of the power line cannot be determined which compromises the commercial viability of the robot. Additionally, the use of encoders is impractical for the commercial robot because they are costly; suffer from mechanical wear-and-tear; and cannot be used to measure the incline on the line. To overcome these limitations an alternative state estimation scheme is designed, which is more practical and cost-effective with no moving parts.

Lastly, the topic of robust trajectory generation in the presence of uncertain model parameters and friction is addressed. A trajectory or path planner is proposed which can overcome uncertain friction to perform brachiation on both a horizontal and inclined line.

1.2 Aims of the study

This research aimed to develop:

1. a system to estimate the state of a two-linked brachiating robot using inertial mea-

surement modules

2. a robust trajectory generator which can dynamically adjust online to ensure a successful brachiation manoeuvre
3. a robust discrete-time feedback control system which can drive the system along a trajectory despite model uncertainty

1.3 Objectives of the study

The objectives of the study were to firstly develop and modify the acrobot model to approximate the dynamics of the BPLIR. The modification involves adjusting the friction model with a trade-off between numerical stiffness and accuracy. This system model is central to the design of a robust controller and a trajectory generator hence calibration is performed to ensure that the plant-model mismatch is minimised.

Secondly, the state estimator uses a kinematic model instead of a dynamic one to provide robustness to physical parameter variation. The kinematic model of the system in conjunction with a Kalman filter and Inertial Measurement Unit (IMU) measurements was used to estimate the system state. The aim was to develop a state estimator that is independent of physical parameters and their variation.

Lastly, a robust control architecture is designed, which can achieve objectives despite parameter variations in the system model. The designed controller is used in tandem with a designed adaptive trajectory generator to enable the BPLIR to perform robust brachiation.

1.4 Purpose of the study

The purpose of the study was to develop a robust brachiation framework for a horizontal and inclined power line. Each aspect of the system design incorporates robustness to achieve an overall robust brachiation manoeuvre.

The developed state estimator uses low-cost Inertial Measurement Units (IMUs) that are easily deployable in a commercial setting with no significant maintenance costs. The designed state estimator is robust by being independent of physical parameters, i.e. it has sole dependence on the kinematics. Another objective was estimating the incline of the structural member or overhead power line, something that is not possible with encoders.

The trajectory generator was designed to work in a setting where environmental factors could alter the feasible path. As such it was designed to be adaptive and flexible with the purpose of dynamic trajectory generation which can provide a reliable reference command to the BPLIR controller despite disturbance torques from friction, aerodynamic drag or other disturbances from the environment.

Finally, the focus of this research is the discrete-time control algorithm implemented at run-time on a micro-controller, namely the STM32F4 Discovery Board. Robustness to parameter variation was at the centre of the design; hence a quantitative feedback design (QFT) approach was taken to develop a robust discrete time control algorithm.

The QFT control design aims to compensate for the worst-case parameter variations in the system model. Parameter variation generated a family of plants, $P_i \in \mathbf{P}$, which could describe the motion of the system. The task was finding a single robust controller that can compensate for all plant variations while meeting the specifications for reference tracking, disturbance rejection and minimising input torque.

The outcome of the research will aid in the development of a commercial high-voltage power line inspection robot. It aims to provide a base off which subsequent researchers may look at the problems of out-of-plane swings and the swing-up problem which are central to the problem of inspection over vast distances.

1.5 Scope and Limitations

The scope of the project encompassed the following objectives:

- develop a state estimation algorithm that can track the state of a two-link robot in a planar brachiation manoeuvre
- design a trajectory generator for a planar brachiation manoeuvre
- design a robust controller for a planar two-link brachiating robot
- test the designed subsystems in the lab using the prototype [73]

The scope of the project was mainly limited to a 2D horizontal and inclined swing case, with 3D motion not being modelled or considered. The existing mechanical prototype [73] was utilised. As such, no major mechanical work was performed on the experimental setup; the only aspect which this project changed was the location of the electronics. Instead of having the electronics mounted on the prototype, they were moved to a bench for easier access and control. The motors and associated motor controllers were kept the same.

1.6 Research Questions

The following research questions were asked and answered during the study:

1. Can a kinematic state estimator be designed using low-cost IMUs and be robust to physical parameter variation?
2. Can a robust trajectory generator and robust controller ensure that the end-effector or gripper always reaches the line despite uncertainty in the friction, aerodynamic drag and other parameters?

1.7 Plan of Development

The dissertation begins by reviewing the literature of power line inspection, brachiation, state estimation and robust nonlinear control in Chapter 2.

The methodology detailed in Chapter 3 discusses how the algorithms were developed in a practical sense and shed light on some of the experimental considerations which were made. The full system model was developed and calibrated in Chapter 4 including the friction and motor models.

The kinematic state estimator, robust controller and trajectory generator are presented in Chapters 5, 6 and 7 respectively. Each of these chapters presents the development of the algorithms in question. Simulation and experimental results are presented to validate the theory.

The discussion, conclusions and recommendations follow in Chapters 9 and 10. The layout of the dissertation is shown in Figure 1.3

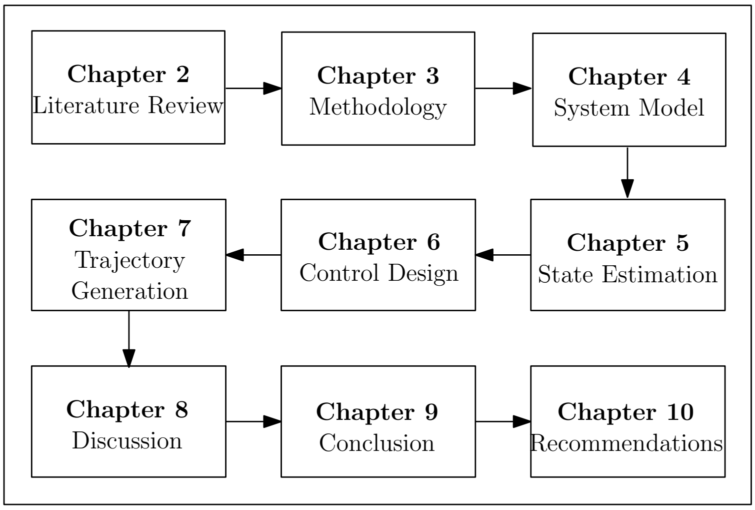

Figure 1.3: Flow chart illustrating the layout of the dissertation

Chapter 2

Literature Review

2.1 Biomimicry

Nature has been a source of inspiration for engineers. This is due to the variety and depth of the complex interlinked systems across the planet. Nature offers insights for engineers who seek to solve complex problems such as locomotion, flight [47] and structured materials, just to name a few [50]. The fascination with nature's solutions has even pioneered a new science called biomimicry.

Biomimicry or biomimetics is a relatively new and growing field of science that analyses nature's best ideas and adapts them for human use [29]. It is impractical to replicate nature's processes exactly given the large scale and complexity of these systems. The need for practicality has led to a departure from the pure science of biomimicry which aims to replicate nature, to bio-inspired design [69]. The bio-inspired design approach adapts certain natural phenomena for the purposes of applied science.

The advantages of bio-inspired design are that it is concerned with the replication of certain aspects of nature's engineering solutions and not an exact replication. The reductionist thinking approach [50] has led to a faster pace of innovation especially in the field of locomotion and bio-robotics [10][62][71]. The subjects of research are wild animals which have distinct ways of navigating their natural environment. This has inspired roboticists around the world to develop novel approaches for underactuated robots such as legged robotics, with central works like [10] inspiring aspects of this project.

Figure 2.1: A snapshot of a video showing an orangutan successfully brachiating along a power line at a considerable height [76]

Brachiation or arm swinging is a form of arboreal locomotion which is used by primates to move between structural members such as tree limbs using only their arms [49]. During brachiation, the forelimbs alternately support the body. Brachiation has fascinated researchers and academics because of the perceived effortlessness of the manoeuvre and the promise of energy efficiency [48].

Brachiating robots, fall in a broad category of underactuated robots that can walk, catch and hop. They require an oscillatory exchange of kinetic and potential energy in a gravity field [42]. Brachiation is attractive for its promise of energy-efficient manoeuvring but has not been applied to any commercial use cases in literature except as laboratory experiments. These brachiating robots (approximated as a double pendulum in literature) have employed brachiation for the task of grasping onto a structural member such as a horizontal ladder, whereby the end configuration of the robot is important. This problem is similar to the application discussed in this dissertation. However, in the current work, the emphasis shifts to reaching the power line or end point with zero velocity to avoid collisions despite uncertain model parameters such as friction.

Most, if not all, the experiments have explored brachiation purely as a laboratory project with no commercial application [22][26]. Patel et al. [70] presented an application for a brachiating power line inspection robot with wheels, whereby brachiation is only for obstacle avoidance during power line inspection. The designed BPLIR introduces a novel gripper which can support the robot during a swing by clasping onto the line. After successfully overcoming an obstacle, the BPLIR uses actuated wrist motors to ride along the line until it meets another obstacle efficiently.

2.2 Power Line Inspection

Power line inspection is of utmost importance for the reliability and stability of an electric power transmission and distribution network [58]. The faults on the power lines usually occur on conductors and insulator strings [38]. Mechanical damage caused by Aeolian vibrations results in strands breaking and the conductor losing its strength which can lead to overheating. Insulator strings are also prone to mechanical damage due to weather and corrosion [38]. Mitigating against these faults requires constant, thorough inspection and maintenance to preserve the integrity of the power system.

During an inspection, it is also necessary to check for vegetation on and beneath power lines, pylons and other power line equipment [58]. Trees and vegetation can hook onto power line equipment and damage the line during high winds as the tree or vegetation sways. Excessive vegitation can also result in short circuits occurring between different phases of the power line, especially during heavy rain. Hence it is always essential to keep vegetation in check to avoid costly damage, loss of supply and earth faults.

Power line inspection poses an ideal problem to be solved by autonomous robots because of the relatively uniform structure of transmission networks. The essential functionality required of autonomous inspection robots is automatic power line tracking, automatic visual inspection, acquisition and transmission of high-resolution images [58]. These images can be of either the line infrastructure or vegetation of the surroundings which are processed by machine vision systems or technicians.

Also, these robots need to overcome obstacles on the line such as spacer dampers, vibration-dampers, suspension clamps, compression dead-ends and jumper cables [70]. Secondly, the robots need to have a good range of operation which will allow them to inspect lines which span over vast distances. Lastly, they need to be manoeuvrable and robust to environmental disturbances such as wind gusts and rain.

The two new approaches to the power line inspection problem are small crewless aerial vehicles (UAVs) and climbing robots. Aerial vehicles take the form of drones or other such robots which fly over the power line while being operated by a technician. They are generally applicable over short distances because of battery constraints and the inefficiency of vertical take-off and landing vehicles. The most notable of these inspection vehicles are the DJI M200 series which has a range of 7 kilometres, a maximum flying time of 38 min and a maximum payload of 2kg [79]. The quick take-off and landing of UAVs make them ideal for augmenting human-crewed inspection missions whereby technicians can perform the inspection without requiring to be on the line physically. However, a UAV is not a long-range multi-day autonomous solution to power line inspection. Instead, UAV's are the miniaturisation of current best practice, i.e. crewed helicopter missions.

Climbing robots such as the LineScout [52], Expliner [57] and UKZN Power Line Inspection Robot [64] are recent developments in the power line inspection space. The main capabilities of these robots are that they can negotiate power line infrastructure successfully, albeit slowly and deliberately, with obstacle negotiation sequences which require two or more minutes. They are also capable of carrying large payloads such as imaging equipment which is advantageous for attaining high-fidelity information about the health of the line. The common trait of these robots is that they are bulky, weighing up to 100kg in the case of the Linescout [52] and mechanically complex in the sense that they require many high-powered actuators. The need for a low DOF, long-range autonomous solution was the motivation for a brachiating power line inspection robot (BPLIR) with wheels [70]. The advantage of the BPLIR is that it can use actuated gripper motors to traverse stretches of obstacle-free overhead power line and can employ a relatively simple, low torque but dynamic brachiation to overcome obstacles.

2.3 Modelling

Dynamic system modelling is an important task when designing feedback controllers. The two main approaches used for modelling dynamic systems are black-box modelling and white-box modelling. Each of these modelling techniques has its advantages and disadvantages which will be touched on briefly.

White-box modelling refers to precise mathematical formulation such as Euler-Lagrange approach [51]. Euler-Lagrange dynamics is a reformulation of classical mechanics based in Newton's three laws of motion. Lagrange mechanics produces dynamic system equations despite conservative or non-conservative forces acting on the system. The resulting equations are in standard manipulator form for a kinematic chain. An advantage of this approach is that the designer has a more in-depth understanding of the system and is better equipped to debug potential issues with the robot.

As the complexity for systems increases, black-box modelling techniques are increasingly utilised to model dynamic systems. The approach involves applying a known input signal to the system, monitoring the output and determining a transfer function, if the system is linear. The transfer function describes the frequency behaviour of a linear system. Generally, nonlinear systems cannot be described by a single transfer function; however, they can be described by a family of transfer functions which capture the local linear behaviour at multiple operating points [77].

Developments in machine learning techniques, particularly feed-forward neural networks, have also been gaining prominence in nonlinear system identification[23]. The literature explores multiple neural network architectures which are useful in system identification, namely multi-layer perceptron, the radial basis function network and the functional link network. The complexity vs benefit of these advanced techniques made them unsuitable for this application. The complexity arises from the enormous amounts of data required to train and tune a neural network for system identification. It is also a black-box approach which means that any malfunctions may not be debugged adequately [19].

Kinematic models, or geometric descriptions of robot links using a coordinate system, are well established for robot calibration [32], state estimation [67] and even control [21] [66]. The advantages of kinematics are that they are independent of dynamic parameters which are often uncertain and time-varying [37]. In the proposed state estimator, the kinematic system representation is used to overcome physical parameter variation.

Friction modelling and the compensation for friction effects has been a topic of considerable mainstream interest in motion control research [54]. Friction modelling is still an ongoing area of research because modelling nonlinear friction effects is challenging, given its highly nonlinear nature. This nonlinear behaviour is captured in models which attempt to describe the dynamic behaviour of friction [24][39]. Friction modelling is vital in understanding systems given that inadequate compensation or modelling of friction can result in excessive steady-state tracking errors, oscillations and limit cycles [33].

2.4 State Estimation

In many engineering applications, it is necessary to estimate the internal states of a system to achieve tight control of its dynamic behaviour [65]. State estimation is a fascinating area of research spurred by the seminal papers of R.E. Kalman [4] and D.G Luenberger [5]. The initial focus of the research was in monitoring the state of linear systems. However, this has come to encompass nonlinear systems with developments such as the extended Kalman filter - perhaps the most widely used nonlinear filter.

To date the most popular nonlinear state estimators are the extended Kalman filter [35] and the unscented Kalman filter [31]. The extended Kalman filter applies the Kalman filter to a nonlinear system by linearising state error dynamics and output error behaviour of the nonlinear models about the current estimate. Linearising nonlinear dynamics has two main drawbacks. The first is the computational cost of calculating Jacobian matrices, especially for high-order models. The second drawback is the possibility of filter instability, especially if the assumption of local linearization about the current estimate is violated [31].

The Luenberger observer [14], developed around the same time as the Kalman filter, is another solution to the state estimation problem. It works by applying a fixed gain to the error between the model and the observed measurement. The Luenberger gain is calculated by specifying observer error dynamics via eigenvalue placement. When the observer gain is high, the linear Luenberger observer converges quickly to the system states if measurement errors are small. This high gain can result in peaking, a phenomenon observed in which the initial state estimator error can be prohibitively large [43]. One extension of the Luenberger observer to nonlinear systems [12] works much the same way as the extended Kalman filter in that the system is linearised and the linear Luenberger observer applied.

2.5 Trajectory Generation and Control

Nakanishi et al. [42] details the methodology used to control a Brachiating Robot (BR) by employing I/O linearization and task encoding via target dynamics. The task of the controller becomes one of forcing the system response to mirror or converge on the dynamic behaviour of the target system. The target dynamics which the BR is encoded to mimic are the dynamics of a pendulum (virtual oscillator). The choice to use a pendulum is supported by bio-mechanics literature which showed that the motion of a pendulum gives a relatively good approximation of the slow brachiation of arboreal apes [9].

The notion of target dynamics is a slight variant on the standard technique of plant inversion or feedback linearization. The feedback linearization scheme results in the system output being directly proportional to the actuator input, which is usually an external reference signal. In the case of [42], the reference signal was generated internally by the system. This approach is useful for encoding the brachiation manoeuvre implicitly but does not give much flexibility to impose a robust outer-loop control structure.

Another drawback of using I/O linearization and target dynamics is the need for a highly calibrated model for reliable brachiation to be achieved. High fidelity, continuous calibration is not practical due to the proposed Power-Line Inspection Robot suffering environmental uncertainty and operational wear-and-tear, which may alter the parameters of the system model over time. The uncertainty in the plant parameters renders the designed controller very susceptible to disturbances. The adverse controller performance is further compounded by the effects of plant-model mismatch. Overall, the combined effects of plant-model mismatch and uncertainty in plant parameters results in a low-quality controller which fails to accomplish the task of brachiation.

An under-actuated system is one where there are more degrees of freedom than actuators. Underactuated system controllers have been designed using collocated or non-collocated feedback linearization (CPFL & NCPFL) [44]. CPFL involves the linearization of the system dynamics, which are directly actuated (active). NCPFL refers to the linearization of the system dynamics, which are not directly actuated (passive).

Spong [27] covers feedback linearization for a two-link acrobot and shows that NCFL is possible given a condition which he refers to as ”Strong Inertial Coupling”. Strong inertial coupling allows the use of the integrator back-stepping formalism to linearise and ultimately control the passive joints. Given that the linearization focuses on one or the other (passive or active), knowledge of the internal or zero dynamics of the system is crucial to understanding the behaviour of the overall system.

Nakanishi et al. [42] show that a lossless mechanical oscillator which incorporates an even and convex artificial potential function can encode the brachiation task quite successfully. The authors show that the use of an artificial potential function of the form of Hooke’s Spring Law potential is computationally convenient. A Lyapunov-style energy function is incorporated as part of the target dynamics to achieve successful swing-up control. This differs from [27] who opted to generate a trajectory which was dependent on the motion of the passive joint and successfully stabilised the two-link robot in the vertically upright position.

The area of most interest to the project discussed in [42] is the application of Raibert-style reverse time symmetry [10]. In a nutshell, reverse time symmetry refers to state trajectories which are mirrored in time (forward time motion is equivalent to reverse time motion) about the vertically down position. This concept of reverse time symmetry produces neutral orbits - trajectories which require relatively simple feedback control for reference tracking. The ceiling consists of all the robot configurations where the end-effectors displacement from the line is zero.

The neutral orbit, in the frictionless case, traces out a trajectory which will go through the vertically down position from a given ceiling point and end at the opposite ceiling point. The problem posed in [42] was one of finding a control law such that the closed-loop dynamics of the system admitted this reverse time symmetry. The task involved finding the requisite frequency ($\omega_{pendulum}$) of a virtual pendulum or oscillator that the system can emulate to achieve successful brachiation given an arbitrary span on the power line. The span of the brachiating robot being the distance between the end-effector and the pivot point when the robot is on the line.

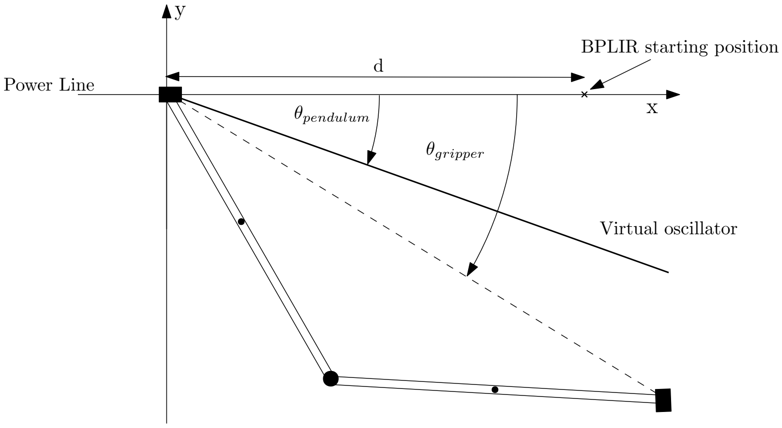

Figure 2.2: Image illustrating the angular relation between the virtual pendulum and the brachiating robot.

The search to find the natural frequency culminated in an involved two-dimensional root-finding procedure for a function whose evaluation entails integrating the dynamics of the system. Integration of the system dynamics is not a trivial feat considering that the system equations are 2-dimensional and nonlinear. The approach used in the paper was a numerical method to approximate a mapping (λ) between the virtual pendulum (oscillator) frequency $\omega_{pendulum}$ and the initial span d using the secant method.

$$\lambda(d) = \omega \tag{2.1}$$

The downside to using target dynamics to encode brachiation into the closed-loop dynamics of the system is the lack of oversight the designer has in ensuring that the control action required remains within a given set of constraints. In addition, the numerical approach used to find the appropriate virtual pendulum frequency is impractical when the system parameters are unknown or uncertain.

A more robust method, albeit computationally intense, is to use nonlinear optimisation techniques to determine the optimal solution given system constraints and a cost function [6]. Additional trajectories would be generated under different friction conditions until a bank of feasible trajectories is developed. A look-up table would then facilitate online selection of the appropriate trajectory. Kelly [75] focuses on transcription methods for solving an optimal control problem which converts a continuous problem into a nonlinear programming problem.

The two broad classes of transcription methods are shooting methods and simultaneous methods. In summary, a single-shooting approach is a method for solving a boundary value problem. Single-shooting iterates through trajectories, reaching one that has the desired end-effector configuration and satisfies the dynamic constraints. Multiple shooting extends this idea by dividing the space into n discrete segments and solving the single-shooting problem for each segment.

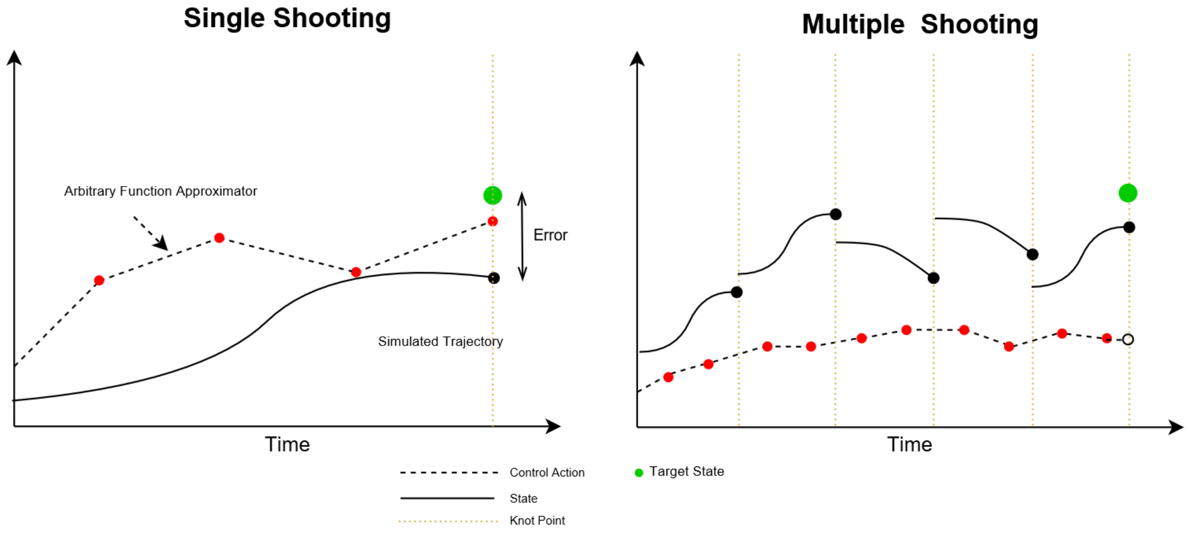

Figure 2.3: A graph illustrating the differences between single vs multiple shooting for trajectory generation

The shooting methods for trajectory generation are computationally intensive and require multiple iterations to converge on a solution. Due to the computational burden imposed by nonlinear programming techniques, it is impractical to utilise them online for trajectory generation. Additionally, model-based optimisation techniques require an accurate system model to achieve optimal performance. In the BPLIR application, an accurate model cannot be guaranteed because of the time-varying nature of individual model parameters such as friction.

2.6 Robust Control

The control of a dynamic system with varying or uncertain parameters has been a focus for a subset of control design, namely *robust control*. The term robust control refers to the problem of designing controllers for systems with uncertain and time-varying parameters, dynamics and unknown input disturbances. The advantage of robust control design is that it deals with uncertainty explicitly. This explicit design means that only a single controller needs to be designed which is capable of meeting client specifications when system behaviour varies.

A robust frequency domain control design developed by Bode [3] is steeped in the stability criterion pioneered by Nyquist [1] and the concept of large loop gain developed by Black [2]. Black showed that with sufficiently high gain, the effect of any parameter variations will be negligible. Further research done by Bode exposed the limitations in relying on high loop gain to achieve control. Bode's sensitivity integral (2.2) quantifies some of the limitations in feedback control of linear parameter invariant systems. .

$$\int_0^\infty ln|S(j\omega)|d\omega = \pi \sum p_k \tag{2.2}$$

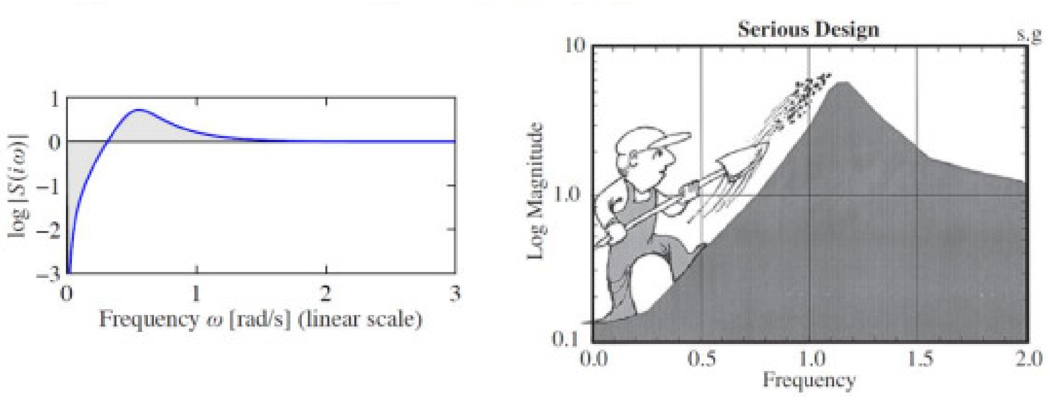

(a) Bode integral formula

(b) Control design process

Figure 2.4: Interpretation of the *waterbed effect* illustrating the sensitivity function plotted against frequency (left) and an artists interpretation of the control design process (left). Image sourced from [61]

The result, coined the "*waterbed effect*", showed that if the sensitivity to disturbance of a feedback control system is decreased at some frequency range, then it will increase at another frequency range. The resultant research produced *classical sensitivity design* whereby the Nyquist chart and Bode plots are used extensively for *Loop Shaping.* The concept of sensitivity design is still prevalent today particularly for quantitative feedback control theorists.

Quantitative Feedback Theory for SISO systems is an approach developed by Horowitz [8], which is based on loop-gain shaping and plant uncertainty representation by 'templates'. These templates are the set of all plant models produced by quantified variations in the uncertain parameters. The loop-shaping of QFT is performed in the Nichols chart, primarily where the sensitivity function is shaped to meet frequency-domain sensitivity specifications. A 2-DOF scheme incorporates robust reference tracking whereby the pre-filter, designed using Bode plots, shapes the tracking behaviour of the system to meet specifications [45]. The QFT approach for SISO systems was extended to MIMO systems by Yaniv, and Horowitz [11] and is still an ongoing area of research.

Modern, robust control techniques such as H^{∞} techniques are some of the later additions to a long list of robust control methodologies. In the H^{∞} formulation, a control designer expresses the control problem as a mathematical optimisation problem and then finds the controller that solves this optimisation. The phrase H^{∞} control comes from the Hardy space in which the optimisation takes place [53]. The H^{∞} norm, which is the subject of minimisation, is the maximum gain in any direction and at any frequency. For SISO systems, this is effectively the maximum magnitude of the frequency response [53].

Model uncertainty is often best handled by optimal/robust control strategies such as Quantitative Feedback Control as well as H^{∞}, which incorporate the uncertainty of the dynamic models directly into the controller formulation. The optimal controllers are not well-established for nonlinear systems because they were developed predominantly for linear systems. To overcome issue of nonlinearity, [36] proposes replacing the nonlinear plant using a set of linear time-invariant plants and any error associated is considered as a state-dependent disturbance.

2.7 Summary of Literature

This chapter aimed to provide a brief introduction to the major works which had an impact on the project. The research areas covered have been state estimation, modelling robust control and trajectory generation.

System modelling discussed approaches to modelling dynamic nonlinear systems. These encompassed white-box modelling techniques such as the Euler Lagrange formulation. Black-box approaches encompass transfer functions and feed-forward neural networks. The two approaches trade-off insight for simplicity whereby the white-box modelling will offer more insight into the system whilst black-box modelling only offers and input-output relation.

State estimation detailed two state estimators, namely the Luenberger observer and the Kalman filter. The Kalman filter is chosen as the filter o choice in subsequent chapters because of sensor fusion. Sensor fusion combines multiple measurements to improve the accuracy of an estimate.

Trajectory generation and robust control of brachiating robots is an under-developed area of research with only a handful of authors exploring the field. The main contribution has been by [10] who presented reverse-time symmetry for control of legged robotics. This reverse-time symmetry is leveraged in this project to inform the design of a trajectory generator. The controller design is informed by quantitative feedback theory which offers the advantage of guaranteed closed-loop performance despite variations in the system parameters.

This project aims to leverage the literature in the application of a brachiating power line inspection which incorporates all these aspects.

Chapter 3

Methodology

This research addresses two main concerns:

- state estimation of a dynamic system with model uncertainty and parameter variation
- adaptive trajectory generation and robust controller design

This chapter explains the research, design and implementation process that was followed in this dissertation to solve the above problems and to answer the research questions stated in Section 1.6. The overarching design philosophy dictates the progression and ultimately success of the project.

The design methodology followed in the development of this dissertation is the V-model [41] illustrated in Figure 3.1. The V-Model is a unique, linear development methodology used during the development life cycle of a product. The V-Model focuses on a fairly typical waterfall-esque method that follows strict, step-by-step stages.

At a conceptual level, a commercial power line robot is a partially autonomous system with the following core operations:

1. Efficient locomotion and obstacle avoidance along a high-voltage overhead power line.
2. Autonomous machine vision for navigation and visual inspection which can discern the health of a high-voltage power line.
3. Communication technologies to transmit status messages regarding the state of the power line and the robot.
4. Energy scavenging technology which will enable the BPLIR to charge its batteries using energy from the power line.

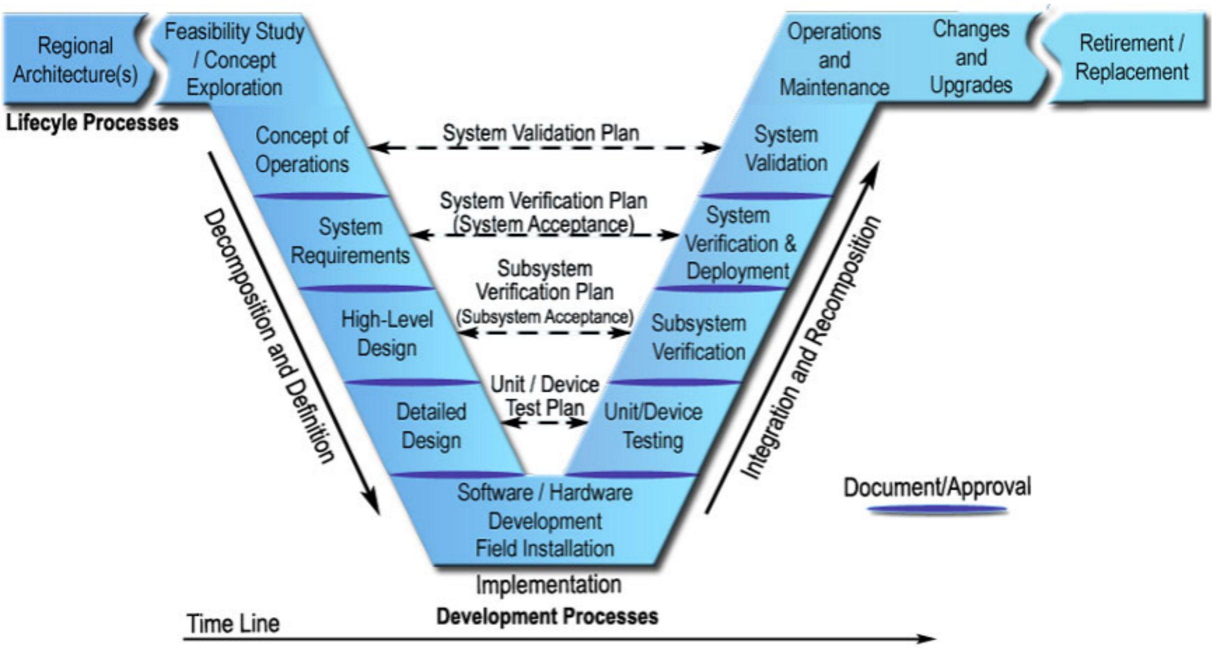

Figure 3.1: Image illustrating the Systems Engineering "V" Diagram [41] which can be utilised in a typical design process such as the design of a robotic control system. It is follows strict step-by-step stages to accomplish the objectives of a product design

This project is concerned mainly with point #1, which is efficient locomotion and obstacle avoidance along a high-voltage overhead power line. The BPLIR [70] can traverse an over-head power line using actuated wrist motors located on the grippers and was able to perform a pre-programmed swing on a horizontal line. The BPLIR will relay visual feedback information to a central control unit during traversal of the over-head line.

When the BPLIR comes across an obstacle on the power line, it will stop, grip firmly on the line with one gripper and brachiate past the obstacle. This brachiation manoeuvre is what is central to this dissertation. There are four key challenges which need solutions to facilitate successful brachiation and general locomotion. These are system modelling or identification, state estimation, trajectory generation and robust control.

3.1 Modelling

The acrobot model, formulated using Lagrange dynamics, modelled the dynamics of the BPLIR if it is limited to 2D. Future work is planned to add revolute wrist joints to enable out-of-plane swing for 3D locomotion. The contact forces which the gripper makes with the line were assumed to be negligible in the dynamic model. The generalised external forces were assumed to be the input torque of the system and any other torque disturbances acting on the dynamics. These torque disturbances, encountered in the operating environment include friction, aerodynamic drag and other unmodelled torque disturbances.

Friction modelling was performed offline with the parameters of viscous and Coulomb friction detailed in [70]. This friction model which is not Lipschitz continuous serves as a benchmark for the proposed candidate friction function which utilised an arctangent function to approximate the discontinuity at the origin. The fundamental trade-off in designing the candidate function was between numerical stiffness and accuracy. As the accuracy of the approximation increased, the derivative close to the origin approached a singularity.

The friction model, in conjunction with the dynamic plant model, were simulated in SIMULINK. An essential step in the design process is the periodic calibration of the model and the prototype. Performing continuous calibration minimises the discrepancy between the model and the physical system (Figure 4.7 shows the result of calibration on the simulated model vs the experimental model).

The need for continuous model validation motivated the design decision to work in a piece-wise fashion with ongoing model validation at each step. Hence, the experimental setup was periodically subjected to a known input signal, and the output monitored. The simulation was subjected to a comparable input signal, and the outputs of the simulation and prototype were compared to determine the magnitude of plant-model mismatch. The plant model mismatch was quantified for later use in QFT controller design.

3.2 State Estimation

The discrete-time extended Kalman filter algorithm is a useful tool for state estimation. The Kalman filter was the ideal state estimator because it can incorporate sensor fusion. Sensor fusion is the process of using multiple sensory inputs to improve the accuracy of a state estimator. The iNemo IMU modules designed by [72] produce 3D gyroscope, accelerometer and magnetometer data at a BAUD rate of 9600bps. This data was transmitted via USART because it only requires two wires for full-duplex transmission and there is no need for a clock signal.

In the initial design phase, the Kalman Filter parameters were tuned offline. The rotary encoders mounted on the BPLIR provided the ground truth, which provided a reference to evaluate the performance of the filter. The state estimator uses a kinematic model of the system which was derived using rectangular coordinates. This choice was sufficient because the BPLIR operated solely within a 2D plane with no singularities along the trajectory. Hence, there was no need for advanced coordinate systems such as quaternions. The kinematic model was validated manually using simulation data that was used to produce an animation which was then matched visually to a video of the experiment. The encoders were used as a ground truth measurement to check whether the kinematic simulation lined up with the experiment.

The initial error covariance, measurement and process noise covariance were determined through calculation and tuning. The resulting offline steady-state error covariance matrix provided the initial error covariance in the final version of the online filter. The measurement and process noises were calculated from the respective datasheets and improved upon using theoretical experiments. The experiments involved propagating a small error term through the kinematic model to determine how it affects the final readings.

3.3 Trajectory Generation

The development of a trajectory generated was rooted in the concept of reverse-time-symmetry [10]. In developing the trajectory generation algorithm, special considerations for the friction effects were taken. The central development platform for the trajectory or path planner was MATLAB's SIMULINK whereby a calibrated simulation of the experimental system acted as a testbed.

The arctangent function served as a candidate for prototype trajectory because it is easier to work with trigonometric relations. The testing of the algorithm occurred in SIMULINK with random alterations to the friction parameters within a range of 20% of the calibrated parameters. The varying friction parameters simulate the effects of an uncertain operating environment and dynamic model.

Parameterising the path using the passive angle resulted in a time-independent path. This path is a gain term on the position of link one and results in a neutral or reverse-time symmetrical trajectory for the horizontal case. The STM32F4 was operated in open loop, i.e. with no applied torque to the motor. The open-loop tested whether the trajectory generated worked as expected on the real hardware vs the simulation. Iterative adjustment of a closed-loop gain of increasing magnitude tested the feasibility of trajectory tracking for a neutral orbit. Results from these open and closed-loop tests served as further calibration of the system model and a precursor to robust brachiation.

Control design or loop-shaping ensures that the system tracks the desired reference signal.

In this case, the internal motor controller module provided the inner loop controller with satisfactory current tracking capabilities. The robust control problem involved mostly pre-filter F and outer-loop controller K design for a class of plant responses $P_i \in \mathbb{P}$. The derivation for the range of variation in plant models was determined using input step tests from the outer loop of the PFL. The step test provided quantifiable evidence for the gain uncertainty for the outer-loop plant.

The frequency-domain provided the design environment for a pre-filter whereby pole and zero placement tuned the responses of the upper and lower bound plant variation. Comparisons between design and simulated responses determined whether the designed controller was sufficient for stabilising the experimental system.

The brachiation manoeuvre served as a test for the robustness of the designed controller. The final brachiation test integrated the prior designed components of state estimation, trajectory tracking and control to determine whether the project was a success.

3.4 Electrical Subsystem

A functioning electrical system is essential to any mechatronics project. The subsystems of the electrical system are human-machine interfaces, actuation, sensing and computation with communications facilitating data transfer between the various systems. Due to the number of interconnected components, electrical system development has multiple potential points of failure.

Actuators are components of a machine that are responsible for moving and controlling a mechanism or system, for example, by opening a valve. They are the mechanisms which convert the electrical system into a mechanical system. Sensors, or transducers, are responsible for converting physical phenomenon into digital or analogue electrical signals to represent a specific quantity, for example measuring the velocity of a link. The embedded system is responsible for receiving, processing and performing calculations on data to fulfil a specific result, such as filtering noise from a signal. Moreover, human-machine interfaces are the link or the means through which an operator or technician may be able to operate and control a physical system. The interconnections of these various systems are shown below in Figure 3.2

Integrating various electrical subsystems, components and software to produce reliable results is an involved process. Continuous debugging and checks need to be performed to determine whether the subsystems work individually and as an integrated product. As

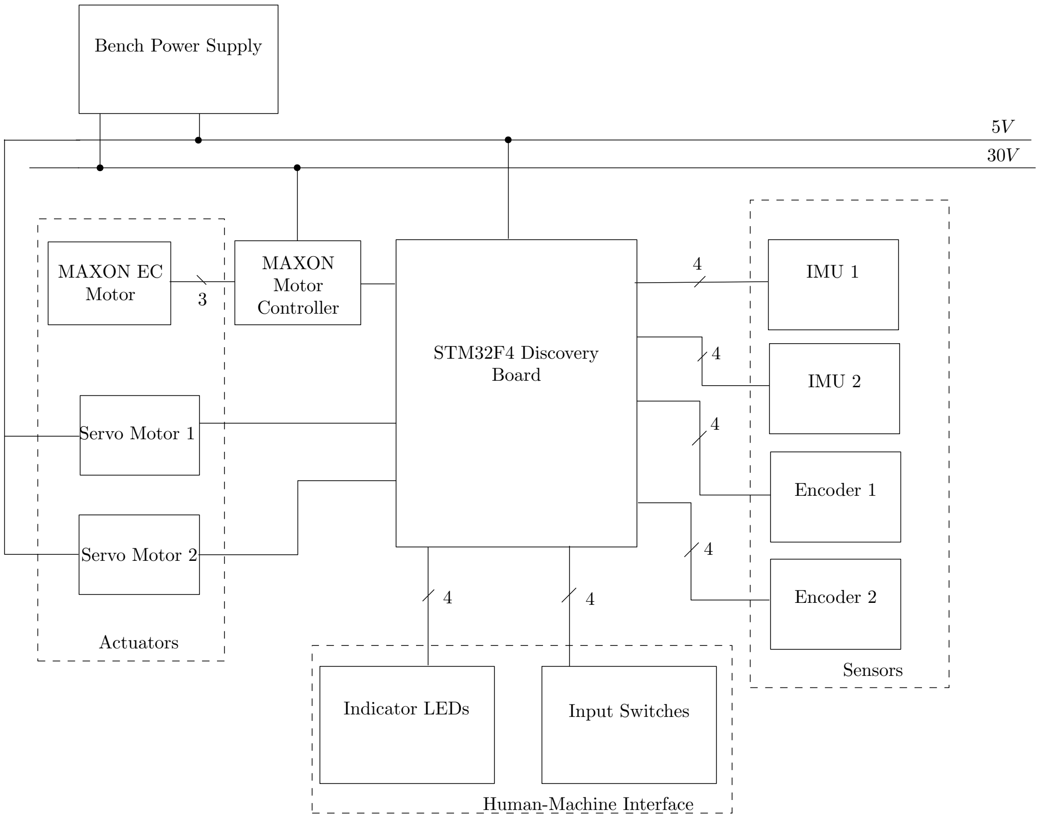

Figure 3.2: Block diagram illustrating the electrical components of the prototype

such, systematic design is the best way to go about electrical & software development, particularly spiral design [15] shown in Figure 3.3.

The spiral design model focuses on getting each feature or component of the software or hardware system to work, each with its own validation cycle. Iterative validation minimises errors throughout the development process and ensures that the integration of the system goes smoothly.

The spiral design process begins with Step 1 "Determining the objectives" of the design with a view of what the final product must achieve. Step 2, "Identify and resolve risks" helps the designer to identify potential failure cases or obstacles which need to be overcome for the design objective to be achieved. Step 3 involves the development and testing of a Minimal Viable Product (MVP) which is a physical prototype developed to meet the design objective. Step 4 is retrospective with the purpose of identifying any shortcomings in the design and potential areas for improvement. The process is repeated and for each iteration, the design progressively becomes better until it meets all criteria specified for the final product.

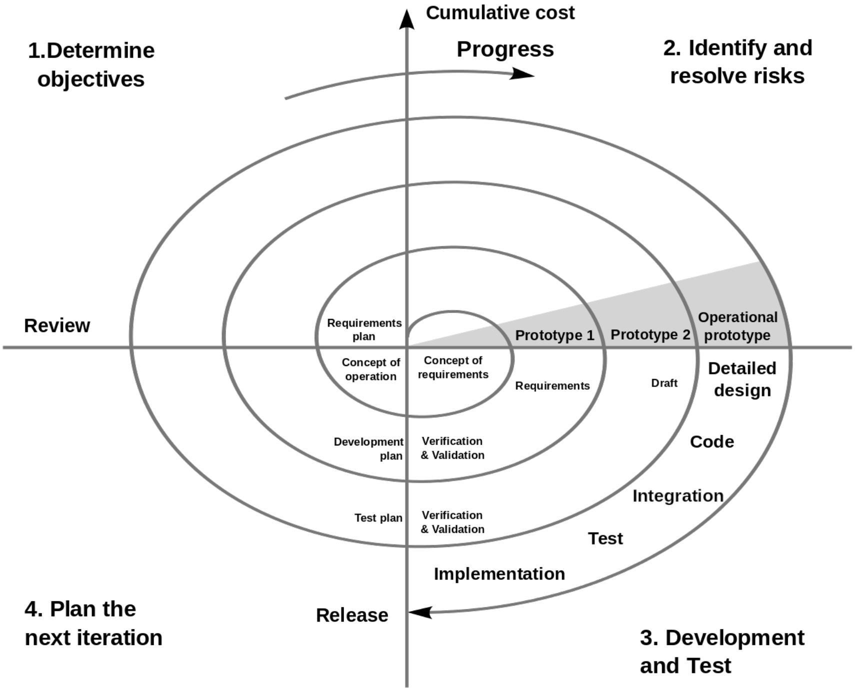

Figure 3.3: Graphical illustration of the spiral design methodology showing iterative design through project phases

3.5 Summary

This chapter has presented the methodology used in each subsequent chapter of the dissertation. The methodology is a guiding principle or ideology in the design process to produce a successful design with minimal error.

There are two main models which were explored, namely the V model and the spiral model. The V model breaks the project into three distinct areas of development, namely state estimation, trajectory generation and robust control. The spiral design methodology develops the capabilities with continuous validation to ensure that the designs work.

A key design challenge with utilising the spiral model was deciding when the design is sufficient. In engineering systems, there is always room for improvement, and the spiral design methodology does run the risk of over-design whereby more features are added. Hence anchoring the overarching design with the v-model and development using the spiral model ensured strict adherence to specification and time.

Chapter 4

System Model

4.1 Introduction

System modelling or identification is the process whereby a mathematical model is derived to describe the dynamic behaviour of a physical system and calibrated against measured data. That is useful in the design, testing and deployment of control systems to meet client specifications. A great deal of work in the control of underactuated systems has been in the context of low-dimensional system models [60]. System models capture the essence of a physical system without including all the real-world complexity of the natural world. That is advantageous as it reduces the computational cost of simulating the dynamics of the system in open and closed-loop, which in turn facilitates prompt iteration through controller designs.

Dynamical systems, however complex, can often be broken up into smaller subsystems which interconnect in cascade and parallel. Cascading is useful because an overarching system model can be found mathematically by cascading a series of relatively simple components. The dynamics of the BPLIR are thought of as a cascade between an electro-mechanical (motor) and mechanical (acrobot) subsystem, as shown in figure 4.1. The system models for each will be derived using a black-box and white-box approach, respectively.

The mechanical subsystem model will be derived using the Euler-Lagrange derivation, which requires a description of the system energy using generalised coordinates. The assumptions made in this model derivation are that the contact forces of the BPLIR on the line do not affect the dynamics of the BPLIR. The line is considered a rigid body locally around the domain of operation of the BPLIR hence bending, vibration and swaying are not considered. A Lipschitz continuous friction approximation is presented in later subsections to increase simulation accuracy.

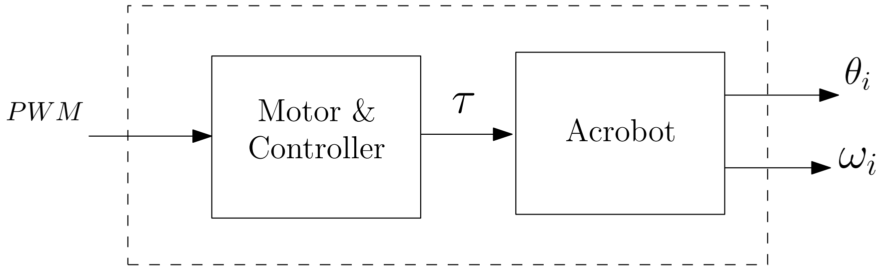

Figure 4.1: High level overview of the interconnected subsystems which constitute the BPLIR

The electro-mechanical subsystem consists of an OEM motor controller, accompanying motor and gearbox. The model will be determined by stimulating the system with a variety of input signals and observing the time-behaviour of the output signals. The observed output provides a mapping or transfer function between the inputs and outputs of the system. This style of modelling is known as black-box modelling and is useful if there is no knowledge of the underlying workings of the system like a manufactured component.

The complete model will be constrained based on the limitations of the physical system. Comparison between the simulations and experimental data will optimise the plant parameters to minimise the mean square error between the plant and the model. Finally, a new batch of experimental data will verify the suitability of the optimised system model to simulate the dynamics of the BPLIR.

4.2 The Acrobot

The acrobot model approximates the dynamics of the PLIR due to the physical similarities of the two systems. It is a planar two-link robotic arm with an actuated elbow as depicted in Figure (4.2). The most common control task in literature is concerned with the swing-up task of the acrobot where the robot is driven to the vertically up position and stabilised. The swing-up task is unlike the brachiating application that has commercial application especially for power line inspection.

The equations of motion for the acrobot are derived using the method of Lagrange [17], for which we will be concerned mainly with the planar swing case using the generalised coordinates $\mathbf{q} = [\theta_1\ \theta_2]^{\mathbf{T}}$ and the states $\mathbf{x} = [\mathbf{q}^{\mathbf{T}},\ \dot{\mathbf{q}}^{\mathbf{T}}]^{\mathbf{T}}$. The generalised coordinates refers to the parameters that describe the configuration of the system and the number of coordinates is equivalent to number of degrees of freedom of the system. Typically, generalised coordinates are selected to provide the minimum number of independent coordinates that define the configuration of a system, which simplifies the formulation of

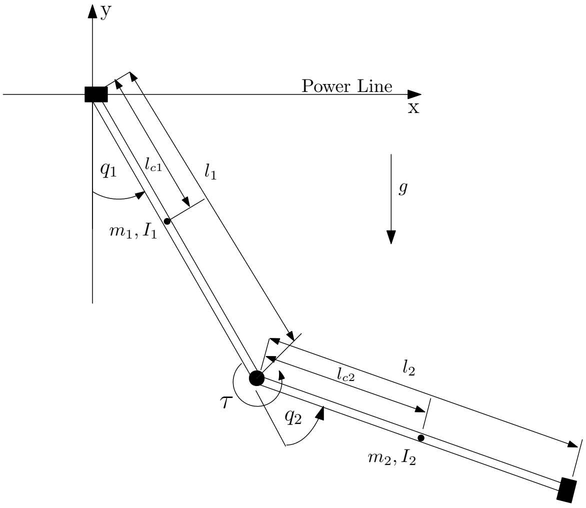

Figure 4.2: A graphical representation of the acrobot

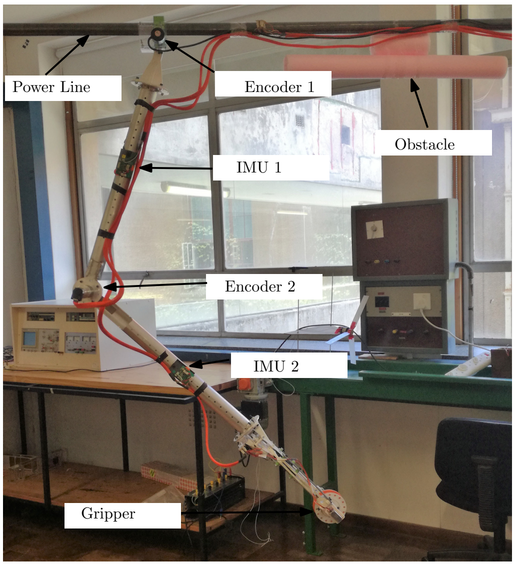

Figure 4.3: A snapshot of the experimental setup in the lab

Lagrange's equations of motion. The Lagrangian (L) is formulated using the kinetic (T) and potential (V) energy of the system expressed in generalised coordinates,

$$L = T(\mathbf{q}, \dot{\mathbf{q}}) - V(\mathbf{q}) \tag{4.1}$$

This is then used to solve (4.2) where $\boldsymbol{\phi}$ represents the vector of external forces acting on the system.

$$\frac{d}{dt}\Big(\frac{\partial L}{\partial \dot{q}_i}\Big) - \frac{\partial L}{\partial q_i} = \phi_i \tag{4.2}$$

The external forces which are accounted for in the model are friction $\mathbf{f}(\dot{\mathbf{q}})$ in the joints and the torque input (τ) from elbow motor.

$$\boldsymbol{\phi} = \boldsymbol{\tau} - \mathbf{f}(\dot{\mathbf{q}})$$

The kinetic and potential energy in the system is found by considering the horizontal and vertical components of the systems motion as well as the rotational energy

$$\begin{aligned} T(\mathbf{q}, \dot{\mathbf{q}}) = {} & \frac{1}{2}m_1(l_{c_1}\dot{q}_1)^2 + \frac{1}{2}I_1\dot{q}_1^2 + \frac{1}{2}I_2(\dot{q}_1 + \dot{q}_2)^2 + \frac{1}{2}m_2(l_1\dot{q}_1)^2 + \frac{1}{2}m_2(l_{c_2}(\dot{q}_1 + \dot{q}_2))^2 \\ & + m_2 l_1 l_{c_2}\dot{q}_1(\dot{q}_1 + \dot{q}_2)c_2 \end{aligned} \tag{4.3}$$

$$V(\mathbf{q}) = -m_1 g l_{c_1} c_1 - m_2 g(l_1 c_1 + l_{c_2} c_{12}) \tag{4.4}$$

Note: $c_1 = cos(q_1), \quad c_{12} = cos(q_1 + q_2), \quad s_1 = sin(q_1), \quad s_{12} = sin(q_1 + q_2)$

Equations (4.3)(4.4) are substituted into (4.1) to find an expression for the Lagrangian for use in (4.2) to find the dynamic equations for the system that can be expressed in the standard manipulator form as shown in (4.5). The full derivation of the system model is available in Appendix A.1.

$$\begin{bmatrix} \dot{\mathbf{q}} \\ \ddot{\mathbf{q}} \end{bmatrix} = \begin{bmatrix} \dot{\mathbf{q}} \\ \mathbf{M}(\mathbf{q})^{\mathbf{-1}}(-\mathbf{C}(\mathbf{q},\dot{\mathbf{q}})\dot{\mathbf{q}} - \mathbf{g}(\mathbf{q}) - \mathbf{f}(\dot{\mathbf{q}}) + \boldsymbol{\tau}) \end{bmatrix} \tag{4.5}$$

where $\mathbf{M}(\mathbf{q}) \in \mathbb{R}^{\mathbf{nxn}}$ is the inertia matrix, $\mathbf{C}(\mathbf{q},\dot{\mathbf{q}}) \in \mathbb{R}^{\mathbf{nxn}}$ is the Coriolis matrix, $\mathbf{g}(\mathbf{q}) \in \mathbb{R}^{\mathbf{n}}$ is the gravity vector, $\boldsymbol{\tau} \in \mathbb{R}^n$ denotes the actuation vector and $\mathbf{f}(\dot{\mathbf{q}}) \in \mathbb{R}^n$ represents the velocity dependent disturbance torque vector due friction and other disturbances.

$$\mathbf{M}(\mathbf{q}) = \begin{bmatrix} m_1 l_{c_1}^2 + I_1 + I_2 + m_2 l_1^2 + m_2 l_{c_2}^2 + 2 m_2 l_1 l_{c_2} c_2 & I_2 + m_2 l_{c_2}^2 + m_2 l_1 l_{c_2} c_2 \\ I_2 + m_2 l_{c_2}^2 + m_2 l_1 l_{c_2} & I_2 + m_2 l_{c_2}^2 \end{bmatrix} \tag{4.6}$$

$$\mathbf{C}(\mathbf{q},\dot{\mathbf{q}}) = -m_2 l_1 l_{c_2} s_2 \begin{bmatrix} \dot{q}_2 & \dot{q}_2 + \dot{q}_1 \\ \dot{q}_1 & 0 \end{bmatrix} \tag{4.7}$$

$$\mathbf{g}(\mathbf{q}) = \begin{bmatrix} m_1 g l_{c_1} s_1 + m_2 g (l_1 s_1 + l_{c_2} s_{12}) \\ m_2 g l_{c_2} s_{12} \end{bmatrix} \tag{4.8}$$

$$\boldsymbol{\tau} = \begin{bmatrix} \tau_1 \\ \tau_2 \end{bmatrix} \tag{4.9}$$

4.3 Friction Modelling

Friction appears in all mechanical systems and has a significant impact on control. The successful design of mechatronic systems requires an understanding of the effects of friction as well as compensation techniques [33]. Generally, the models which are described in literature approximate friction and do not provide a *neat* solution. These approximations are not ideal, given that for the BPLIR, friction is the largest contributor to the uncertainty in the system dynamics. The sources of friction include, but are not limited to, external wind resistance and state-dependent, stiction and gearbox friction. The resulting uncertainty is due to the varying nature of the friction parameters and the lack of a well-defined mathematical model.

A basic model of the system friction, illustrated in Figure4.4, is comprised of two components, coulomb (f_c) and viscous (f_v) friction which oppose the movement of the i^{th} joint. Coulomb friction (f_c) is a model which describes friction as a force independent of the velocity once motion occurs. The model improves through the addition of viscous friction f_v and aerodynamic drag (air resistance), which represents the force due to friction as dependent on the velocity of the moving body.

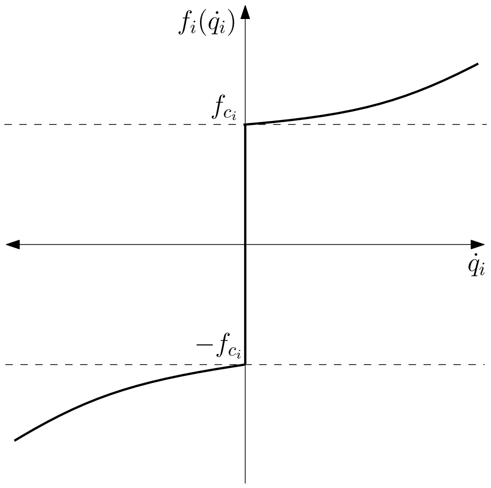

Figure 4.4: Friction model incorporating viscous and coulomb friction

$$f(\dot{q}_i)_i = f_{c_i} sgn(\dot{q}_i) + f_{v_i}\dot{q}_i + \frac{1}{2}\rho_{air} C_d A \dot{q}_i^2 \tag{4.10}$$

The friction model described in (4.10) is not Lipschitz continuous at the origin as the derivative is undefined, which presents numerical challenges when simulating the system. An alternative approach ignores Coulomb friction in simulation and focuses on the viscous friction such as in [73]. Although this solves the problem of Lipschitz continuity, it results in sizeable plant-model mismatch which in turn adversely affect the performance of the closed-loop system.

Equation (4.11) presents an alternative approximation of friction (4.10) using a Lipschitz continuous function. The objective is to develop a function which is Lipschitz continuous, and which provides an acceptable trade-off between accuracy and numerical stiffness which can cause simulation issues. The proposed friction model is modelled after the arc-tangent function given the similarities in the curvature compared to the friction model and the minimal use of parameters.

$$\tilde{f} = f_v \dot{q}_i + f_c \frac{2}{\pi} tan^{-1}(\dot{q}_i/b) + \frac{1}{2}\rho_{air} C_d A \dot{q}_i^2 \tag{4.11}$$

Shown above in (4.11) is the candidate function to approximate the friction of the system. The tuning parameters b corresponds the steepness or numerical stiffness of the candidate function. The coefficient b was constrained to 0.01 to regulate the numerical stiffness of the function which compromises on the accuracy of the approximation. The results in Table 4.1 show that the proposed approximation offers a reduction in the RMSE by 92% over the linear approximation over a frequency range of $-40\ rad/s \leq \dot{q} \leq 40\ rad/s$. The simulation was constrained to 40 rad/s because it is well outside the domain of operation

Table 4.1: RMSE comparison of different friction models to approximate (4.10)

	Candidate function	**Viscous friction only**
RMSE	0.0272	0.35

of the BPLIR of $\pm 20 rad/s$.

The task of this section was presenting a Lipschitz continuous function which can approximate the discontinuous model (4.10). In the subsequent sections, calibration of the actual plant and against the model improves the accuracy of simulations.

4.4 Motor Model

The purpose of this section is to determine the model of the motor subsystem shown below in Figure 4.5. The section focuses on the determination of an input-output relation from input current reference (i_{ref}) to torque output $K_m i_{meas}$, where K_m is the motor torque constant. This transfer behaviour will inform design decisions for the controller in subsequent sections. Black-box or white-box modelling is useful in determining the input-output relationship of an unknown plant.

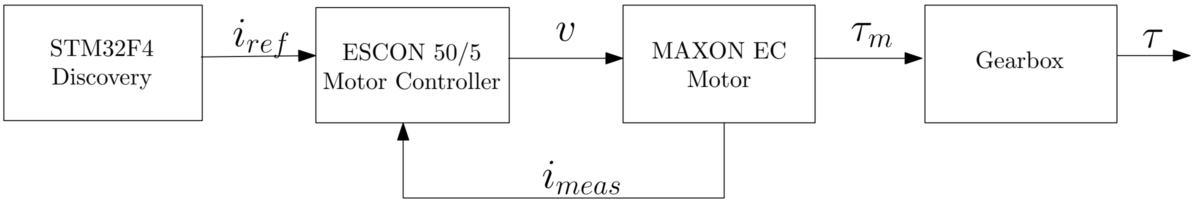

Figure 4.5: Block diagram model of the motor subsystem

White-box modelling involves determining the differential equations from first principles using the datasheet information. Black-box modelling is the process of applying a range of PWM inputs and observing the output current behaviour of the motor, which in this case would be the motor current draw.

The decision to use black-box modelling was preferred since the manufacturer compiles the datasheet under strict and controlled laboratory conditions which are not entirely consistent with the experimental setup of the BPLIR.

For a start, in the experimental setup, the motor is cascaded with a gearbox that drives the BPLIR linkages. The cascaded subsystem causes a significant amount of loading on the motor that can alter the dynamic response. The loading on the motor due to gearbox and linkage loading on top of friction creates a dead-band non-linearity.

The dead-band means that the motor must produce torque with magnitude greater than $|\tau_{min}|$ to overcome the gearbox and linkage friction before motion occurs. The dead-band is the range of inputs to which have a magnitude which is below $|\tau_{min}|$. Dead-bands create dead-time and for certain conditions, excessive and persistent oscillations.

Secondly, the motor connects to an ESCON 50/5 Motor Controller that has operational limitations [73] that will be explored further in this section. In summary, the controller is sensitive to i^2R heating and will initiate safety interlocks to prevent damage to the motor and the associated motor controller. These interlocks cause a reduction in output current to levels which are deemed safe by the motor controller. At this point, the motor controller overrides the outer-loop controller and ignores any further current commands.

The experimental setup in the lab is illustrated in Figure 4.5. The STM32F4 microcontroller provides a current reference signal, in the form of a PWM command to the motor controller (ESCON 50/5 module). The mapping between the duty cycle (D) and reference current is given by (4.13). The ESCON module is configured using the accompanying software package (ESCON Studio) to operate as a closed-loop current controller. The controller varies the applied motor voltage such that the error between the current reference and measured current converges to zero. The exact structure of the internal control loops is not accessible; hence black-box modelling was performed. It should be noted that the relationship between motor current and torque quite simply be expressed by (4.12) however, this is only applicable when the motor is in its linear region of operation.

$$\tau = K_m N \eta_g \eta_m i \tag{4.12}$$

A series of step tests were performed whereby the current reference was varied, and the output motor controller current was measured. ESCON Studio, the accompanying software for the motor, logged the corresponding motor current. The logging capacity of ESCON Studio is limited to 341 samples with a maximum sampling period of 10ms. Hence the minimum sampling period was used except for the ramp input test that required 20ms (see Figure 4.6).

$$i_{ref} = \begin{cases} 15 & D \geq 90\% \\ \frac{15}{80}D - \frac{15}{8} & 10\% \leq D \leq 90\% \\ 0 & D \leq 10\% \end{cases} \tag{4.13}$$

The observation from the results shown in Figure 4.6 is that the step response from cur-

Table 4.2: Motor, gearbox and motor controller parameters according to the datasheets and experimental values

Unit	Parameter	Datasheetvalue	Actual value	Unit
Motor	Nominal voltage	48	30	V
	Nominal current	3.68	-	A
	Stall current	124	-	A
	Nominal torque	0.0929	-	Nm
	Stall torque	3.43	-	Nm
	Motor torque constant ($\mathrm{K_m}$)	0.634	-	Nm/A
	Maximum motor efficiency (η_m)	90	-	%
Gearbox	Gearbox ratio (N)	74	-	-
	Max. gearbox efficiency (η_g)	72	-	%
Motor Controller	Max. current	15 (< 20 sec)	15 (< 2.675 sec)	A
	Max. continuous current	5	5	A

rent command ($\mathrm{i_{ref}}$) to instantaneous output current occurs within one sample (10ms). The instantaneous current output suggests that the time constant of the current response is less than or equal one sampling period or 10ms.

Another observation from the response is that the controller cannot maintain high current for long periods because of i^2R heating. The internal controller was able to maintain a maximum current of 15A for only 2.675 seconds before dropping back below to 5A.

This restrictive behaviour means that the controller algorithm must also be conservative and use less than the rated torque as far as possible to avoid motor controller safety features from being activated. The safeguards result in a mismatch between the desired current signal and the actual motor current, which in turn produces unpredictable system behaviour.

4.5 Model Calibration

Model calibration is a process which seeks to minimise the discrepancy between the system model and the physical plant. The primary sources for these discrepancies in the system model are the dynamic parameters such as mass, inertia and friction. Geometric parameters which contribute to the uncertainty are the link lengths and the centres of mass for the links. Of these uncertain parameters, friction is the most significant contributor. Its large variety of mathematical models [7][34] only capture noticeable effects at the expense of a general solution.

In Section 4.3 the approximation (4.11) only relates a candidate function to a math-

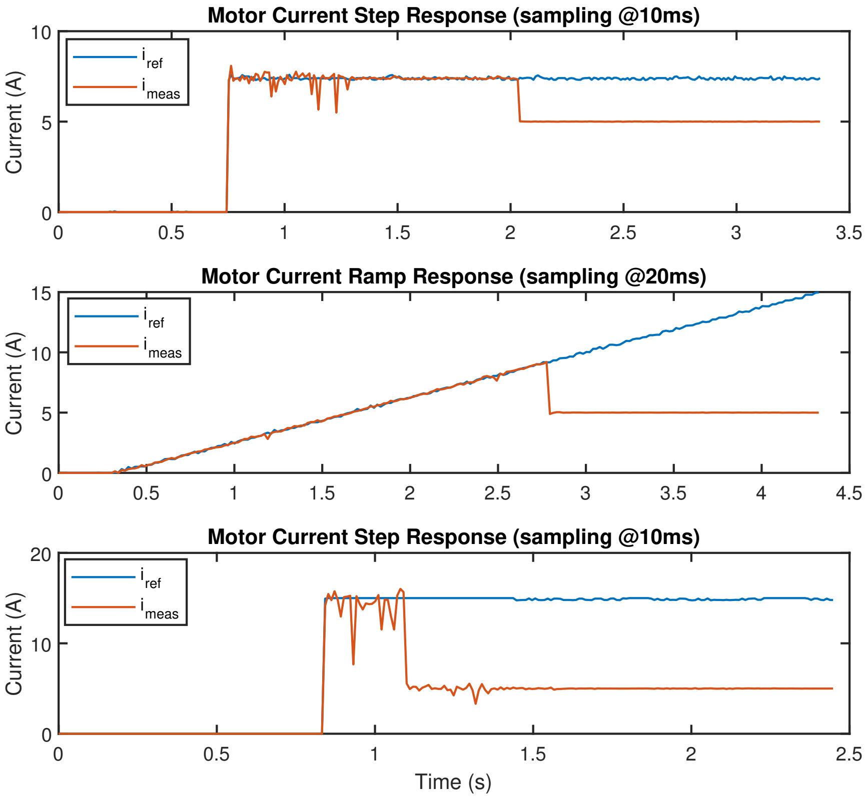

Figure 4.6: Image illustrating a subset of the step tests performed on the motor with reference currents ranging from half the maximum current (top), a ramp input (middle) and maximum current (bottom)

ematical friction function which comprises of viscous and Coulomb friction only. The next step is to incorporate the friction model into the dynamic model of the system and conduct plant-model calibration. A free swing test [0,18]s followed by a constant input torque test [18,30]s was performed, logged, and the data from each compared to simulation data. The model was calibrated by varying the parameters to minimise the mean square error between the simulated model and logged data.

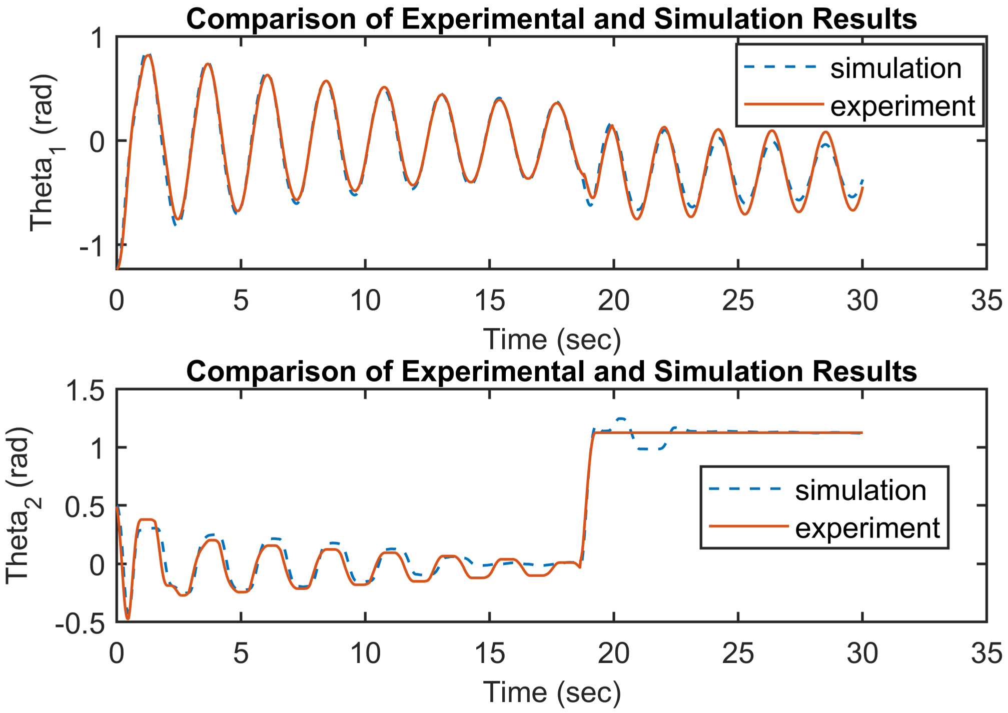

Figure 4.7: Comparison between calibrated simulation model and real data for a free swing and constant torque input of 5.8 Nm applied @$t = 18.63s$

Figure 4.7 shows that the friction approximation (4.11) is enough when the PLIR is swinging freely in a pendulous motion. However, when a torque input is applied the dynamic behaviours of the model deviates from the real system. This deviation is due to a deficiency in the friction approximation such as the inability to simulate discontinuities. The uncertainty is mainly due to time-varying friction and gearbox effects (Table 4.3 illustrates the effect of the gearbox whereby $f_{c_2} \geq 61 f_{c_1}$).

Parameter	Value	Parameter	Value	Unit
f_{v_1}	0.1706	f_{v_2}	0.0765	$Nm.(rad/s)^{-1}$
f_{c_1}	0.0124	f_{c_2}	0.7681	Nm
l_1	0.9091	l_2	1.2451	m
l_{c_1}	0.2167	l_{c_2}	0.5459	m
m_1	3.2287	m_2	1.5155	kg
I_1	0.1539	I_2	0.2191	$kg.m^2$

Table 4.3: Final optimised (w.r.t RMSE) model parameters for the BPLIR physical system

Although optimisation of the plant-model error is implemented, uncertainties in the model will inform the need to implement robust feedback control. Robust feedback control will result in desired tracking performance and disturbance rejection despite changes in the dynamic model. It is noted that the optimised parameters differ from the design plant parameters detailed in [73]. This mismatch occurs because the optimiser has lumped certain effects, and this may be inconsistent with the physical prototype. Despite this, the optimised model can accurately describe the dynamics of the plant to within a margin of 20%, which is useful for simulation purposes.

4.6 Dead-Band Modelling

A dead-band is a range of input values that results in a zero output. Therefore, any input signal which has a magnitude within the dead-band results in a loss of control over the dynamic system occurs. Modelling of a dead-band is a relatively simple process. A ramp input is applied to the system, and the output is monitored to check when motion occurs. The input value magnitude, which starts motion is then the edge of the dead-band. It is essential to model the dead-band in the forward and reverse direction because it may be an asymmetrical non-linearity [77], hence there will be a lower bound and upper bound on the dead-band.

Compensation for dead-band involves input conditioning, i.e. if the input is within the dead-band, apply an adjustment to push it outside the dead-band region. Hence the minimum permissible motor current command will induce a torque that is on the edge of the dead-band hence the system is always in the linear region.

The system was subjected to a ramp input with a mild gradient until the link velocity jumped to a non-zero value. The data were analysed for a range of ramp inputs and the current required to initiate movement was approximately 0.63A. This current threshold corresponds to a minimum torque of

$$\tau_{min} \approx 0.82336 \tag{4.14}$$

The minimum torque presented in (4.14) deviates from the value for the Coulomb friction (see Table 4.3) in the second link f_{c_2} by approximately 6%. This deviation was considered within a reasonable rage of the true value hence it was accepted.

4.7 Effects of Partial Feedback Linearisation

In subsequent chapters, collocated feedback linearization makes the control problem more tractable. Section 6.2 discusses further details on feedback linearization and its application. It will suffice, for this chapter, to know that feedback linearisation results in a transformed single-input multiple-output system with state variables ($\mathbf{z}$) (see Figure 4.8

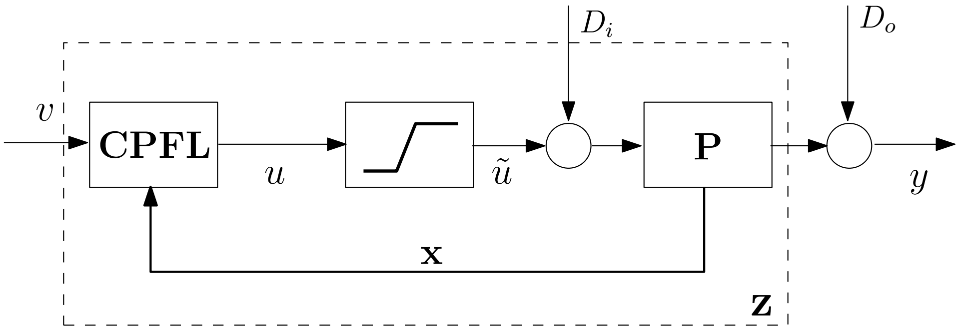

Figure 4.8: Block diagram illustrating the transformed open-loop system after applying collocated partial feedback linearization

) where

$$\frac{d}{dt}\begin{pmatrix} z_1 \\ z_2 \\ \dot{z}_1 \\ \dot{z}_2 \end{pmatrix} = \begin{pmatrix} \dot{z}_1 \\ \dot{z}_2 \\ \zeta(z_1, z_2, v) - n_{11}f_1 - n_{12}f_2 \\ -n_{21}f_1 - n_{22}f_2 + v \end{pmatrix} \tag{4.15}$$

where v is the input to the transformed system parameterised by state variables $\mathbf{z}$.

After applying partial feedback linearization, the control problem becomes designing an outer loop controller for the transformed system to satisfy the technical specifications (see section 6.3). The need for accurate control necessitates a further step in the modelling process which explores the full effects of feedback linearization without friction compensation. The uncertain effects of friction motivate the need to design a quantitative feedback outer loop controller which can achieve the desired behaviour regardless of model variation.

The open-loop transfer behaviour from the input signal v (see Block Diagram in Figure 4.8) to the output link angles were monitored at a sampling rate of 100 Hz for varying step tests with v as an input. The output responses of the step inputs are shown in Figure 4.9 whereby the angle of the links (θ_1 and θ_2) is the measured output.

The step tests, with v adjusted for each test, were performed multiple times for varying step sizes and showed that the system exhibits a 2^{nd} order response for θ_1, a delayed 1^{st} order response for θ_2. The responses each have a dead-time (T_d) and gain variation. Dead-time corresponds to a delay between the application of an input signal and the response of the output signal.

The response exhibits a high degree of damping on link two, whereby there is no overshoot

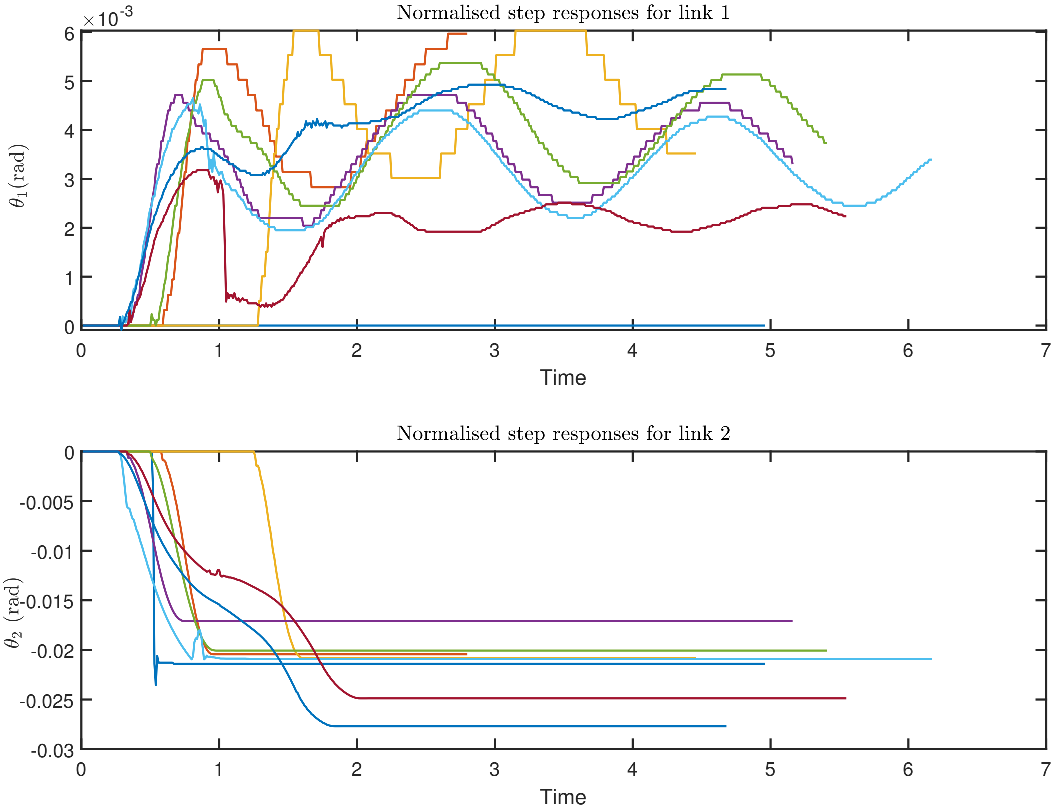

Figure 4.9: Image illustrating the normalised angular position step response results for the link angles θ_1 (top) & θ_2 (bottom) for the partially feedback linearised subsystem

on the output. The damping is expected since the joint of the second link experiences loading from friction, the linkage and the gearbox. The response for θ_2 is modelled after first-order continuous systems with an uncertain time constant and amplitude.

$$T_{\frac{y}{v}} = \frac{-k}{sa+1} e^{-sT_d} \tag{4.16}$$

where $a \in [0.19, 0.22],\ k \in [0.013, 0.035]\ \mathit{and}\ T_d = [0.15, 0.3]$.

The oscillations in θ_1's response were more pronounced than in link two and are attributed to the reduced amount of friction in the link. The bounding transfer functions for θ_1 are not necessary for this report. It is enough to note that the model is stable hence the control system design is centred on actuating θ_2.

4.8 Conclusion

This chapter presented a model which describes the motion of the PLIR based the acrobot. The equations of motion were derived using the Euler-Lagrange formulation. The formulation produced the system equations in the standard kinematic manipulator form.

A Lipschitz continuous friction model balances the trade-off between numerical stiffness and approximation accuracy in simulating the friction in the links. The resultant model was compared to real system data, and the mean square error between the model and data minimised by optimising the system parameters.

The motor model was found using black-box modelling techniques. The motor controller provided desirable closed-loop performance when controlling the motor current without compensation. This performance comes at a cost because the controller is conservative and activates safeguards which disregard reference commands that exceed the continuous rated current when activated.

Although rigorous calibration was conducted, the plant-model mismatch was still present (maximum of 20% from Figure 4.7) in the final system model. This mismatch is due to the changing or uncertain model parameters of the system, such as the unmodelled friction effects. The quantifiable friction variations inform the need for robust feedback control to compensate for this mismatch and other uncertainties which are present in the system.

The uncertainty resulting from partial feedback linearization was quantified in, and it was shown that the effect of friction on the PFL is a damped response. In link two, this reduces the model to an approximate first-order system (4.16), and in link one, it results in a dampened second-order system which is stable (see Figure 4.9). Both subsystems are non-minimum phase because of the input-output delay.; hence there is a fundamental limitation that exists in the achievable tracking performance and disturbance rejection.

In future, an online calibration procedure can ensure that the plant-model mismatch is minimised despite long periods of operation of the PLIR. The online calibration will then counteract parameter drift or uncertainty over extended periods of operation. A more thorough model of the friction can be investigated, which may incorporate the drag on each link and the reaction forces on the line. An alternative motor controller is worth investigating to allow the BPLIR to perform more aggressive manoeuvres.

Chapter 5

State Estimation

5.1 Introduction

There is a general observer design problem in systems theory. It focuses on how to reconstruct the internal states of a system given knowledge of the outputs. The internal state variables are the smallest possible subset of system variables that can represent the entire state of the system at any given time.

The internal states may not be measurable due to constraints such as instrumentation costs. It may also be impractical to add sensors to a plant which operates in harsh environmental conditions whereby the lifespan and quality of instrumentation deteriorate over time. State estimation algorithms such as the Kalman filter can discern sensor measurements accurately in the presence of process, measurement and state noise.

The basic idea of a state estimator, shown in Figure 5.1, is to use a model of the system to *predict* or determine an *a priori* estimate of the states of the system. The estimates

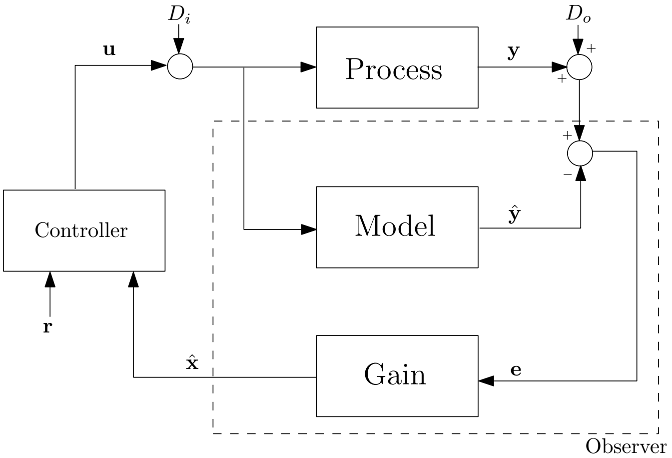

Figure 5.1: A block diagram illustrating the general structure of a state observer

are compared to *measurements* of the process outputs and the *error* is calculated. This error is then subjected to a *gain* to correct the discrepancies and ensure that the estimate converges on the real value resulting in a more accurate *posterior* estimate. The gain calculation is the main design problem which is solved differently depending on the state estimation algorithm used.

Linear state observers which utilise pole placement, such as the Luenberger observer offer a solution to the problem. The convergence of the filter estimate to the underlying value in this approach is contingent on the appropriate choice of observer poles. The rate of convergence of the filter estimate to the underlying value is dependent on the noise magnitude and model accuracy, i.e. fast convergence if the noise is small and the model accurate. As a rule of thumb, these observer poles must be at least twice as fast as the open-loop poles of the plant [5]. The problems which arise with this type of state observer are the noise-bandwidth trade-offs which can lead to compromised state estimates. Erroneous state estimates then have adverse effects on the overall closed-loop performance of the feedback control system.

The Kalman filter and its extension, the extended Kalman filter (EKF), are one of the most widely used state estimators for linear and nonlinear systems, respectively. It offers performance improvements on fixed-gain observers such as the Luenberger observer. It offers an optimal solution (for the linear case) in the sense that it minimises the estimated error covariance at each time step. The main design advantage of the Kalman filter is that the noise in the system is modelled explicitly; however, the drawback is an increase in computational cost.

Successful brachiation requires accurate state estimation to negotiate around obstacles effectively. Generally, state estimation algorithms rely on a dynamic model which requires knowledge of physical and geometric parameters. Physical or dynamic parameter dependence makes the observer vulnerable to variations and uncertainties, which results in erroneous estimation. Inaccurate state estimation, in turn, does not guarantee the robustness of the closed-loop system in the observer-based control feedback scheme. A kinematic-based approach can offer increased robustness due to its sole dependence on geometric parameters, the uncertainty of which is considerably less [16].

The two-link robot has two 6-DOF Inertial Measurement Units (IMUs) that measure the 3-D acceleration ($\boldsymbol{\mu}$) and angular velocity ($\boldsymbol{\omega}$) of the links. IMUs have a better price-performance ratio in comparison to rotary encoders. Another advantage is that mounting an IMU compared to a rotary encoder is a simple mechanical procedure. Lastly, IMUs can measure q_1, the angle at the attached gripper with respect to the inertial frame.

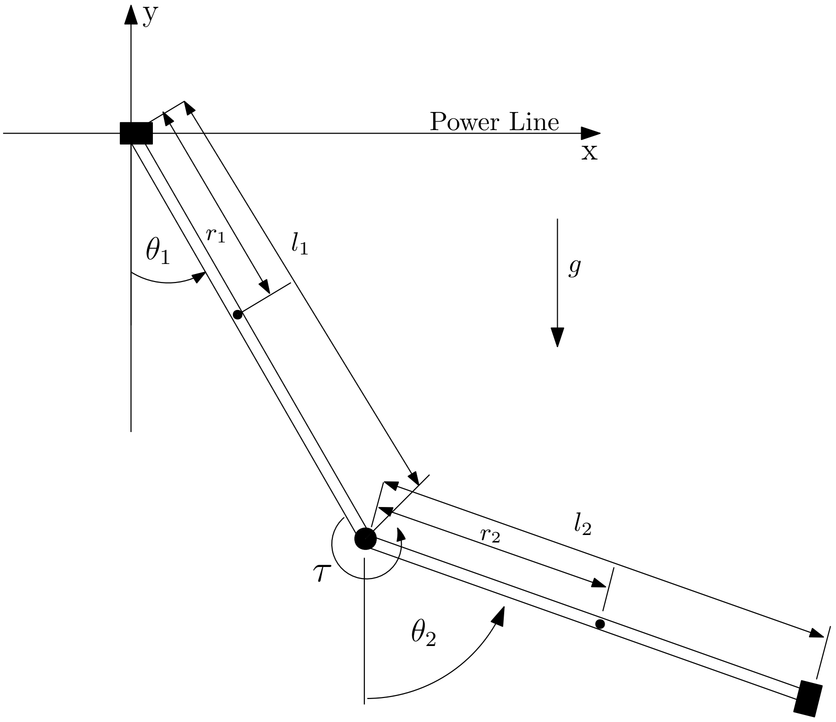

Figure 5.2: Image illustrating the kinematic representation of the acrobot

The mechanical simplicity, cost and measurement performance are the motivations for developing a state estimation algorithm which utilises low-cost MEMS. The kinematic equations of the system will be used to calculate the *a prior* state estimate, $\hat{\mathbf{x}}^-$ which serves as the model estimate.

This chapter is structured as follows. Section 5.2 focuses on the derivation of the kinematic model of the BPLIR, which incorporates IMU readings. Section 5.3 focuses on the observability of the system. Section 5.4 presents the extended Kalman to determine the system state. Section 5.5 present the results of the filter and Section 5.6 concludes the applications and performance of the filter compared with encoder readings.

5.2 Kinematic Model

In this section, the discrete-time nonlinear kinematic system model equations (5.3)(5.4) serve as the prediction equations in the state estimator are derived from the continuous-time equations (5.1)(5.4)

$$\frac{d}{dt}\mathbf{x} = f(\mathbf{x}, \mathbf{u}) \tag{5.1}$$

$$\mathbf{y} = h(\mathbf{x}) \tag{5.2}$$

First, the continuous-time kinematic model (5.1)(5.4) is discretised using an explicit Euler discretisation. This assumption is reasonable because the sampling rate (T_s) is fast, and the dynamics are not stiff.

$$\mathbf{x}_{k+1} = \boldsymbol{f}_d(\mathbf{x}_k, \mathbf{u}_k) = T_s\boldsymbol{f}(\mathbf{x}_k, \mathbf{u}_k) + \mathbf{x}_k \tag{5.3}$$

$$\mathbf{y}_k = h(\mathbf{x}_k) \tag{5.4}$$

where $\mathbf{x} \in \mathbb{R}^n$, $\mathbf{u} \in \mathbb{R}^m$, $\mathbf{y} \in \mathbb{R}^p$ are the state, input and output respectively where the time dependence is implied. The mappings $f : \mathbb{R}^{m+n} \to \mathbb{R}^n$, $h : \mathbb{R}^n \to \mathbb{R}^p$ describe the state transition and the output map.

The kinematic model for prediction equations for the system is developed based on Figure 5.2 using the angles relative to the inertial frame. The following notation will be used to shorten the length of the equations; $s_i = \sin(\theta_i),\ c_i = \cos(\theta_i),\ s_{ij} = \sin(\theta_i - \theta_j)\ and\ c_{ij} = \cos(\theta_i - \theta_j)$.

A rotation matrix is introduced, which rotates from the body frame (**B**) into the inertial/world frame (**O**).

$${}^o_b\mathbf{R}_i = \begin{pmatrix} c_i & -s_i \\ s_i & c_i \end{pmatrix} = {}^b_o\mathbf{R}_i^{-1} \tag{5.5}$$

Given a coordinate system with an origin at link one as seen in Figure 5.2, it can be shown that the location of the IMUs is expressed by (5.6)(5.7).

$$\begin{pmatrix} x_1 \\ y_1 \end{pmatrix} = r_1 \begin{pmatrix} s_1 \\ -c_1 \end{pmatrix} \tag{5.6}$$

$$\begin{pmatrix} x_2 \\ y_2 \end{pmatrix} = \frac{l_1}{r_1}\begin{pmatrix} x_1 \\ y_1 \end{pmatrix} + r_2 \begin{pmatrix} s_2 \\ -c_2 \end{pmatrix} \tag{5.7}$$

Differentiating (5.6)(5.7) twice with respect to time yields

$$\begin{pmatrix} \ddot{x}_1 \\ \ddot{y}_1 \end{pmatrix} = {}^o_b\mathbf{R}_1 \begin{pmatrix} \dot{\omega}_1 \\ \omega_1^2 \end{pmatrix} r_1 \tag{5.8a}$$

$$\begin{pmatrix} \ddot{x}_2 \\ \ddot{y}_2 \end{pmatrix} = \frac{l_1}{r_1}\begin{pmatrix} \ddot{x}_1 \\ \ddot{y}_1 \end{pmatrix} + {}^b_o\mathbf{R}_2 \begin{pmatrix} \dot{\omega}_2 \\ \omega_2^2 \end{pmatrix} r_2 \tag{5.8b}$$

The 3-axis accelerometer readings ($\boldsymbol{\mu}$) are related to the kinematic acceleration in (5.8) by

$$\begin{pmatrix} \ddot{x}_i \\ \ddot{y}_i \end{pmatrix} = {}^o_b\mathbf{R}_i \begin{pmatrix} \mu_{x_i} \\ \mu_{y_i} \end{pmatrix} - \begin{pmatrix} 0 \\ g \end{pmatrix} \qquad i = 1, 2 \tag{5.9}$$

Substituting (5.9) into (5.8) it can be shown that the nonlinear kinematic state space model is given by

$$\frac{d}{dt}\begin{pmatrix}\theta_1\\ \theta_2\\ \omega_1\\ \omega_2\end{pmatrix} = \begin{pmatrix}\omega_1\\ \omega_2\\ \frac{1}{r_1}(\mu_{x_1} - gs_1)\\ -\frac{l_1}{r_1 r_2}c_{21}(\mu_{x_1} - gs_1) + \frac{1}{r_2}(\mu_{x_2} - gs_2 - l_1\omega_1^2 s_{21})\end{pmatrix} \tag{5.10}$$

The output map of the system is selected for maximal use of the available sensor outputs. Given that the body acceleration measurements along links 1 and 2 are not used in the state transition, they will be incorporated into the outputs, y_3 and y_4 respectively.

$$\mathbf{y} = \begin{pmatrix}\omega_1\\ \omega_2\\ \omega_1^2 r_1 + gc_1\\ e\end{pmatrix} \tag{5.11}$$

where,

$$e = \frac{l_1}{r_1}c_{21}(\omega_1^2 r_1 + gc_1) + \frac{l_1}{r_1}\omega_2^2 r_2 + (1 - \frac{l_1}{r_1})gc_2 - \frac{l_1}{r_1}s_{21}\mu_{x_1}$$

And the corresponding measurements are given by the IMU sensor readings

$$\mathbf{z}_k = \begin{pmatrix}\omega_1\\ \omega_2\\ \mu_{y_1}\\ \mu_{y_2}\end{pmatrix} = \begin{pmatrix}gyro_1\\ gyro_2\\ accelerometer_1\\ accelerometer_2\end{pmatrix} \tag{5.12}$$

5.3 Observability analysis

Observability is a measure of whether the states of a system can be inferred from knowledge of its external outputs [63]. It can offer insights into the expected performance of the observer, which can aid the design process. A linear system of order n is observable if

$$rank[\mathbf{M}_O] = rank\begin{pmatrix}C^T\\ C^T A\\ \vdots\\ C^T A^{n-1}\end{pmatrix} = n \tag{5.13}$$

A linear time-varying (LTV) state transition model (5.14a) can be found by taking the appropriate Jacobian of (5.10) w.r.t the state and inputs along the trajectory $\mathbf{x}^*$,$\mathbf{u}^*$

$$\frac{d}{dt}\mathbf{x} = \mathbf{A}(t)\mathbf{x} + \mathbf{B}(t)\mathbf{u} \tag{5.14a}$$

$$\mathbf{y} = \mathbf{C}(t)\mathbf{x} + \mathbf{D}(t)\mathbf{u} \tag{5.14b}$$

where the continuous time-varying state matrices $\mathbf{A}(t) \in \mathbb{R}^{n\times n}$, $\mathbf{B}(t) \in \mathbb{R}^{n\times m}$, $\mathbf{C}(t) \in \mathbb{R}^{p\times n}$ and $\mathbf{D}(t) \in \mathbb{R}^{p\times m}$ are given by

$$\mathbf{A}(t) = \frac{\partial}{\partial \mathbf{x}}\boldsymbol{f}(\mathbf{x},\mathbf{u})\Big|_{\mathbf{x}*,\mathbf{u}*} \quad \mathbf{B}(t) = \frac{\partial}{\partial \mathbf{u}}\boldsymbol{f}(\mathbf{x},\mathbf{u})\Big|_{\mathbf{x}*,\mathbf{u}*}$$

$$\mathbf{C}(t) = \frac{\partial}{\partial \mathbf{x}}\mathbf{h}(\mathbf{x},\mathbf{u})\Big|_{\mathbf{x}*,\mathbf{u}*} \quad \mathbf{D}(t) = \frac{\partial}{\partial \mathbf{u}}\mathbf{h}(\mathbf{x},\mathbf{u})\Big|_{\mathbf{x}*,\mathbf{u}*}$$

A linear observability analysis can be applied to the linear time-varying system, (5.14a)(5.14b) which is expanded in (5.15). This is possible because the LTV model is slowly time-varying and can be approximated "frame by frame" as a linear system. Hence the local linearization along the trajectory is enough to determine the observability of the system.

$$\frac{d}{dt}\mathbf{x} = \begin{pmatrix} 0 & 0 & 1 & 0 \\ 0 & 0 & 0 & 1 \\ -\frac{g}{r_1}c_1 & 0 & 0 & 0 \\ a_{41} & a_{42} & -\frac{2l_1}{r_2}\omega_1 s_{21} & 0 \end{pmatrix}\mathbf{x} + \begin{pmatrix} 0 & 0 \\ 0 & 0 \\ \frac{1}{r_1} & 0 \\ -\frac{l_1}{r_1 r_2}c_{2-1} & \frac{1}{r_2} \end{pmatrix}\mathbf{u} \tag{5.15a}$$

$$\mathbf{y} = \begin{pmatrix} 0 & 0 & 1 & 0 \\ 0 & 0 & 0 & 1 \\ -gs_1 & 0 & 2\omega_1 r_1 & 0 \\ c_{41} & c_{42} & 2\frac{l_1}{r_1}c_{(2-1)}\omega_1 r_1 & 2\frac{l_1}{r_1}\omega_2 r_2 \end{pmatrix}\mathbf{x} + \begin{pmatrix} 0 & 0 \\ 0 & 0 \\ 0 & 0 \\ 0 & 0 \\ -\frac{l_1}{r_1}s_{21} & 0 \end{pmatrix}\mathbf{u} \tag{5.15b}$$

where the quantities a_{ij}, b_{ij}, c_{ij} and d_{ij} are evaluated along the trajectory $\mathbf{x}^*$,$\mathbf{u}^*$ and are given by,

$$a_{41} = -\frac{l_1}{r_1 r_2}s_{21}s_1 g + \frac{l_1}{r_1 r_2}c_{21}c_1 + \frac{l_1}{r_2}\omega_1^2 c_{(2-1)}$$

$$a_{42} = \frac{l_1}{r_1 r_2}s_{21}s_1 g - \frac{l_1}{r_2}\omega_1^2 c_{(2-1)}$$

$$c_{41} = \frac{l_1}{s_1}s_{2-1}(\omega_1^2 r_1 + gc_1) - g\frac{l_1}{r_1}c_{2-1}s_1$$

$$c_{42} = -\frac{l_1}{r_1} s_{2-1}(\omega_1^2 r_1 + g c_1) + g\frac{l_1}{r_1} s_2 - g s_2$$

Breaking the problem into two parts results in a more tractable showcase of observability. First, reducing the output map to the angular velocity only, $y = [y_1, y_2]^T$ exposes points along the trajectory which are not observable without y_3 and y_4, i.e. they do not satisfy (5.13). The task of determining or proving observability becomes one of showing that by increasing the measurements, these previously unobservable points along the trajectory become observable, which in turn implies the entire trajectory is observable. First, we introduce a reduced-order output map.

$$\mathbf{y}_r = \mathbf{C}_r\mathbf{x} + \mathbf{D}_r\mathbf{u} \tag{5.16}$$

where $\mathbf{D}_r = \mathbf{0}$ and

$$\mathbf{C}_r = \begin{pmatrix} 0 & 0 & 1 & 0 \\ 0 & 0 & 0 & 1 \end{pmatrix}$$

If the observability matrix $\mathbf{M}_{\mathrm{Or}}$ is formulated using $\mathbf{C}_{\mathrm{r}}$ instead of $\mathbf{C}$ as it was for (5.13) then it can be shown using MATLAB's symbolic toolbox that

$$rank[\mathbf{M}_{O_r}] \neq n, \qquad \begin{cases} a_{31} = 0 & or \\ a_{42} = 0 \end{cases} \tag{5.17}$$

The next output map which will be analysed will include gyroscope and accelerometer measurements such that the new output map $\mathbf{C}$ becomes

$$\mathbf{C} = \begin{pmatrix} 0 & 0 & 1 & 0 \\ 0 & 0 & 0 & 1 \\ c_{31} & 0 & c_{33} & 0 \\ c_{41} & c_{42} & c_{43} & c_{44} \end{pmatrix} \tag{5.18}$$

It can be shown that,

$$rank[\mathbf{M}_O] = n, \qquad \begin{cases} a_{31} = 0 & or \\ a_{42} = 0 \end{cases} \tag{5.19}$$

Given that the output map (5.18) now produces a full rank observability matrix when evaluated at

$$a_{31} = 0 \quad or \quad a_{42} = 0$$

It can then be concluded that the system (5.15) is fully observable across the entire state space.

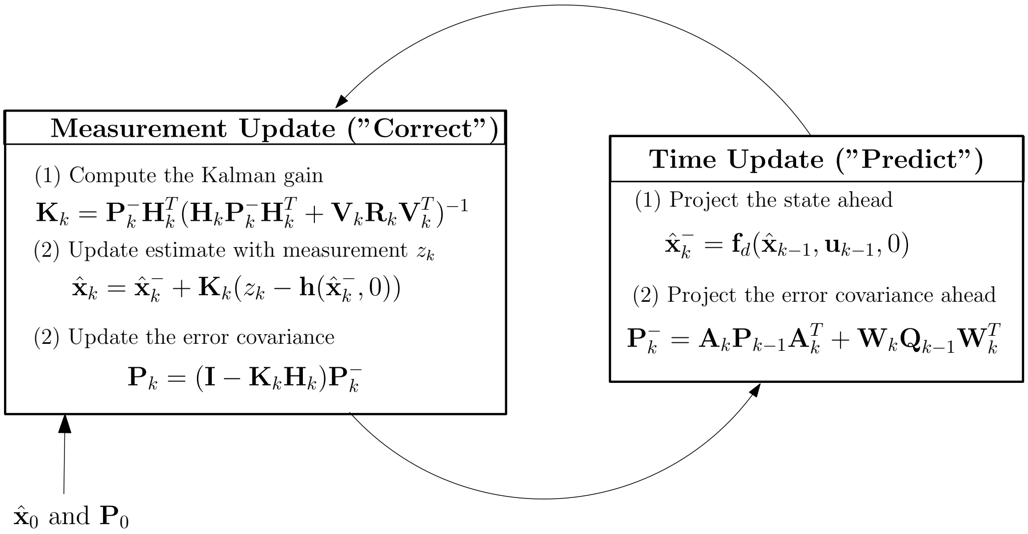

Figure 5.3: A complete operational overview of the Kalman Filter

5.4 Extended Kalman filter

The extended Kalman filter in this section is designed to operate on a discrete-time process governed by the nonlinear process difference equation (5.20a) and the corresponding measurement (5.20b). The discrete-time model (5.20) is found by applying an explicit Euler discretisation on (5.10) . This discrete model is denoted by $\boldsymbol{f}_\mathrm{d}$.

$$\mathbf{x}_k = \boldsymbol{f}_d(\mathbf{x}_{k-1}, \mathbf{u}_{k-1}) + \mathbf{w}_{k-1} \tag{5.20a}$$

$$\mathbf{z}_k = \mathbf{h}(\mathbf{x}_k) + \mathbf{v}_k \tag{5.20b}$$

The random variables $\mathbf{w}_\mathrm{k}$ and $\mathbf{v}_\mathrm{k}$ represent the state and measurement noise respectively. They are assumed to be independent with a Gaussian noise distribution. The noisy accelerometer readings ($\tilde{\mu}$) and gyroscope ($\tilde{\omega}$) data is described by

$$\tilde{\mu}_k = \mu_k + n_\mu \tag{5.21}$$

$$\tilde{\omega}_k = \omega_k + \omega_{bias} + \omega_{temp} + n_\omega \tag{5.22}$$

The main sources of noise in (5.20) are the accelerometer measurement which incorporates misalignment in the IMU and the gyroscope measurement. It is presumed that the rate gyro bias ω_bias, and temperature-dependant drift ω_{temp} are known and compensated for then (5.23) is used to find the *a priori* state estimate, $\hat{\mathbf{x}}^-$. The error covariance matrix, $\mathbf{P}^-$, is found by solving (5.24).

$$\hat{\mathbf{x}_k}^- = \boldsymbol{f}_d(\hat{\mathbf{x}}_{k-1}, \mathbf{u}_{k-1}) \tag{5.23}$$

$$\mathbf{P}_k^- = \mathbf{A}_k \mathbf{P}_{k-1} \mathbf{A}_k^T + \mathbf{W}_k \mathbf{Q}_{k-1} \mathbf{W}_k^T \tag{5.24}$$

where

$$\mathbf{A}_k = \frac{\partial \boldsymbol{f}_d}{\partial \mathbf{x}}\bigg|_{(\hat{\mathbf{x}}_{k-1},\mathbf{u}_{k-1},0)} \qquad \mathbf{W}_k = \frac{\partial \boldsymbol{f}_d}{\partial \mathbf{w}}\bigg|_{(\hat{\mathbf{x}}_{k-1},\mathbf{u}_{k-1},0)} \tag{5.25}$$

The process noise covariance $\mathbf{Q}_{\text{k-1}}$ is calculated from the noise density function, which is available in the datasheet [78]. Since the sensors are identical, it follows that respective noise covariance terms are also identical. Substituting the noise model (5.21) into (5.20a) and isolating the noise terms, it follows that the process noise covariance matrix is given by (5.26) with uncorrelated noise terms.

$$\mathbf{Q} = \mathbf{E}(n_\mu n_\mu^T) = \sigma_{n_\mu}^2 \mathbf{I}_{4\times 4} \tag{5.26}$$

And the matrix $\mathbf{W}_{\text{k}}$ is found by solving (5.27), where we assume the main sources of noise are due to the accelerometer signals:

$$\mathbf{W}_k = \frac{\partial \boldsymbol{f}}{\partial \mathbf{w}}\bigg|_{(\hat{\mathbf{x}}_{k-1},\mathbf{u}_{k-1},0)} = \begin{pmatrix} 0 & 0 & 0 & 0 \\ 0 & 0 & 0 & 0 \\ 0 & 0 & \frac{1}{r_1} & 0 \\ 0 & 0 & -\frac{l_1}{r_1 r_2} c_{21} & \frac{1}{r_2} \end{pmatrix} \tag{5.27}$$

(5.28) then follows from (5.27) and (5.26).

$$\mathbf{W}_k \mathbf{Q}_{k-1} \mathbf{W}_k^T = \sigma_{n_\mu}^2 \begin{pmatrix} 0 & 0 & 0 & 0 \\ 0 & 0 & 0 & 0 \\ 0 & 0 & {\frac{1}{r_1}}^2 & -\frac{l_1}{r_2} c_{21} (\frac{1}{r_1})^2 \\ 0 & 0 & -\frac{l_1}{r_2} c_{21} (\frac{1}{r_1})^2 & p \end{pmatrix} \tag{5.28}$$

where p is given by

$$p = (-\frac{l_1}{r_1 r_2} c_{2-1})^2 + (\frac{1}{r_2})^2$$

The update stage (5.29)-(5.31) calculates the Kalman gain, *posterior* state estimate $\hat{\mathbf{x}}$, and the *posterior* error covariance matrix $\mathbf{P}_{\text{k}}$.

$$\mathbf{K}_k = \mathbf{P}_k^- \mathbf{C}_k^T (\mathbf{C}_k \mathbf{P}_k^- \mathbf{C}_k^T + \mathbf{V}_k \mathbf{R}_k \mathbf{V}_k^T)^{-1} \tag{5.29}$$

$$\hat{\mathbf{x}}_k = \mathbf{x}_k^- + \mathbf{K}_k \Big(\mathbf{z}_k - \mathbf{h}(\hat{\mathbf{x}}_k^-) \Big) \tag{5.30}$$

$$\mathbf{P}_k = (\mathbf{I} - \mathbf{K}_k \mathbf{C}_k) \mathbf{P}_k^- \tag{5.31}$$

where

$$\mathbf{C}_k = \frac{\partial \mathbf{h}}{\partial \mathbf{x}}\bigg|_{(\hat{\mathbf{x}}_{k-1},0)} \qquad \mathbf{V}_k = \frac{\partial \mathbf{h}}{\partial \mathbf{v}}\bigg|_{(\hat{\mathbf{x}}_{k-1},0)} \tag{5.32}$$

Given a set of measurements given by (5.33)

$$\mathbf{z} = \begin{pmatrix} \tilde{\omega_1} \\ \tilde{\omega_2} \\ \mu_{y_1} \\ \mu_{y_2} \end{pmatrix} = \begin{pmatrix} gyro_1 \\ gyro_2 \\ accelerometer_1 \\ accelerometer_2 \end{pmatrix} \tag{5.33}$$

The measurement noise covariance matrix **R**, is calculated using the gyroscope measurement model (5.22) assuming ω_{bias} and $\omega_{temperature}$ are known and compensated for through sensor calibration.

$$\mathbf{R}_k = \mathbf{E}(n_\omega n_\omega^T) = \begin{pmatrix} \sigma_{n_\omega}^2 & 0 & 0 & 0 \\ 0 & \sigma_{n_\omega}^2 & 0 & 0 \\ 0 & 0 & \sigma_{n_\mu}^2 & 0 \\ 0 & 0 & 0 & \sigma_{n_\mu}^2 \end{pmatrix} \tag{5.34}$$

It follows from (5.32)(5.34) that **R** is unchanged because

$$\mathbf{V}_k = \mathbf{I}_{4\times 4} \tag{5.35}$$

The initial covariance estimate is calculated using the noise density as function of sampling frequency in the datasheet. The noise density of the 3-D acceleration and 3-D angular rate, is shown in Table 5.1.

Symbol	**Parameter**	**Value**	**Unit**	**@100Hz**
σ_{n_μ}	Acceleration noise density	220	$\mu g/\sqrt{Hz}$	0.02156^2
σ_{n_ω}	Rate noise density	0.03	dps/$\sqrt{Hz}$	(0.0166^2)

Table 5.1: Noise density parameters of the accelerometer (LSM303DLHC) & gyroscope (L3GD20)

The parameters in Table 5.1 were used to calculate the covariance matrices (5.39)(5.40) with sampling frequency ($\mathrm{f_s}$) of 100Hz.

$$\sigma_{n_\mu}^2 = \left(220 \times 10^{-6} \times 9.8 \times \sqrt{f_s}\right)^2 = (0.02156\ m.s^{-2})^2 \tag{5.36}$$

$$\sigma_{n_\omega}^2 = \left(0.03 \times \frac{\pi}{180} \times \sqrt{f_s}\right)^2 = (0.0166\ rad/s)^2 \tag{5.37}$$

In calculating the error covariance for the accelerometer readings, it is reasonable to assume that misalignment is a greater error source than the noise associated with the device itself. To illustrate this fact, we assume that there exists a maximum $2.5^\circ \approx 0.0436\ rad$ misalignment of the accelerometer when the BPLIR is vertically down and stationary. This will result in a measurement error ϵ of

$$\epsilon = g \sin 2.5^\circ \approx 0.427 \tag{5.38}$$

The misalignment error magnitude necessitates an adjustment to the noise covariance term for the accelerometer to account for this misalignment. It was assumed that the misalignment error would be comparable to 2.5° hence the covariance was adjusted to

$$\sigma^2_{n_\mu} \approx (0.427\ \frac{m.s^{-2}}{sample})^2 \tag{5.39}$$

$$\sigma^2_{n_\omega} \approx (0.02\ \frac{rad/s}{sample})^2 \tag{5.40}$$

5.5 Results

The results in this section document three broad classes of motion. Shown in Figure 5.4 are the results for the angular position estimate and Figure 5.5 is the associated error performance compared to encoder ground truth. In each case, the state estimator output is plotted against encoder data, and the accuracy is bench-marked against an integral of the gyroscope signal (GYR) where,

$$GYR = \int_{n=0}^{\infty} \omega_i \quad , i = 1, 2 \tag{5.41}$$

The experiments performed on the PLIR tested; in each case, an aspect of the below-mentioned motion:

1. *Free response* swing whereby the PLIR was raised to an arbitrary height and released.
2. A disturbance torque or *knock* applied to the PLIR in motion.
3. The motor was *actuated* which resulted in a torque on the links
4. A *catch* brings the PLIR to a stationary state to simulate it gripping onto the line

In this context, a combined test refers to each of the above motions being evaluated sequentially during a single swing. Another test which was performed was evaluating

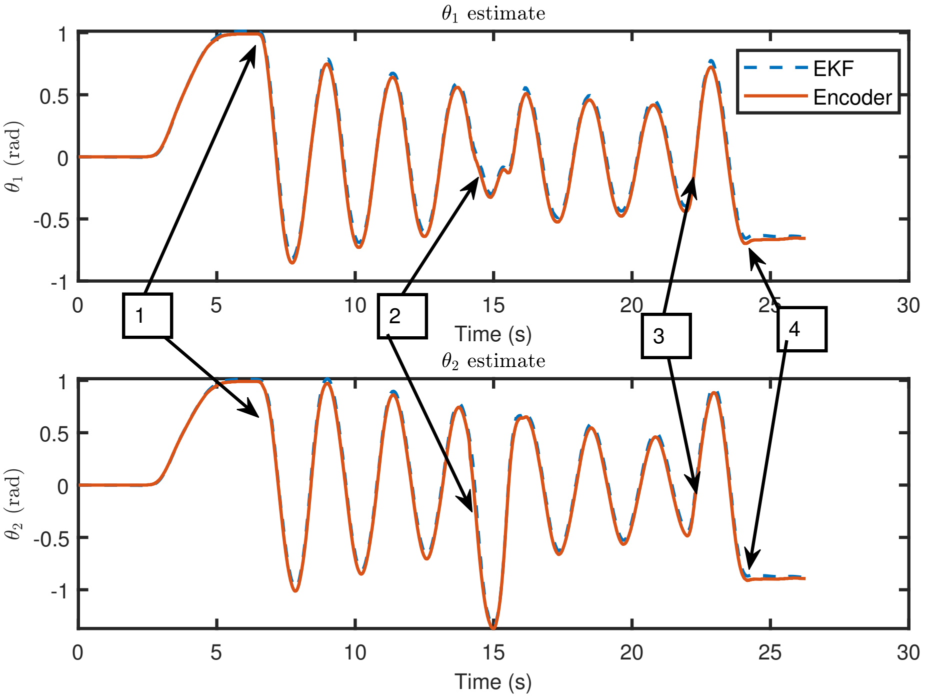

Figure 5.4: Kinematics-based extended Kalman Filter results based on a combined test whereby multiple test scenarios are performed in one test. The numbers correspond to the experiment scenarios detailed above. (1 $rad \approx 58°$)

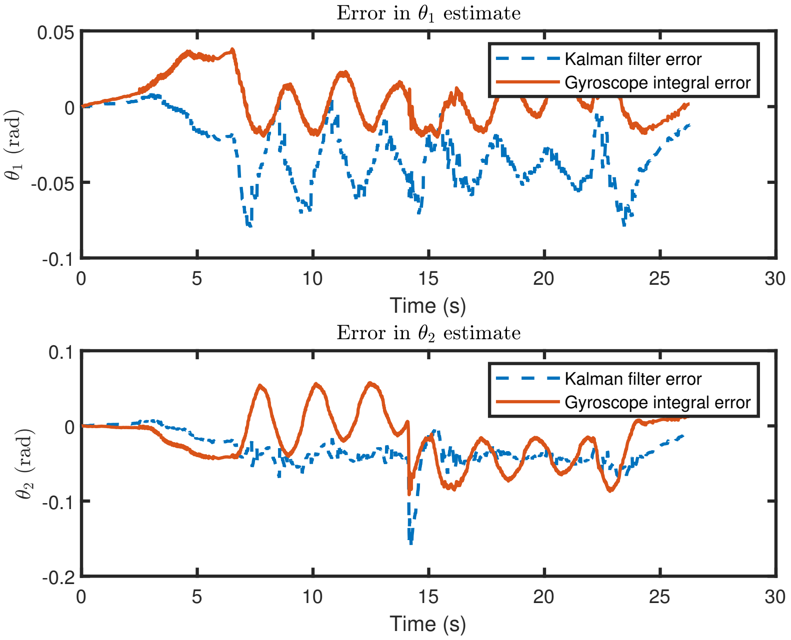

Figure 5.5: Error comparison of K-EKF vs GYR signals based on a combined test. (0.05 $rad \approx 2.9°$)

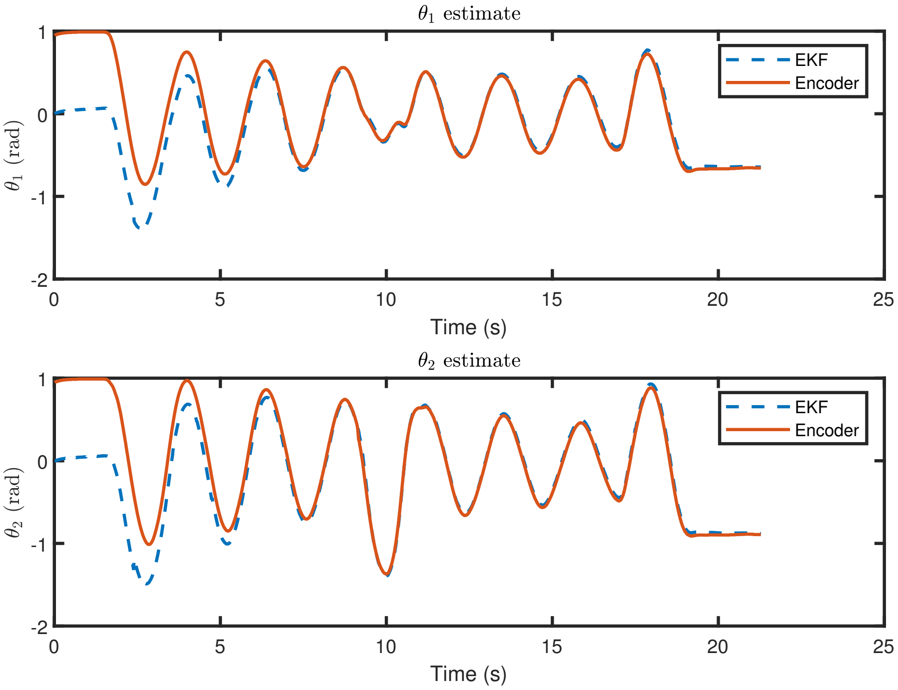

Figure 5.6: Comparison of K-EKF vs "ground truth" encoder signals based on a combined test and erroneous initial conditions. (1 $rad \approx 58°$)

whether the EKF can correct for erroneous initial conditions. The estimators capability to correct of erroneous initial conditions is shown in Figure 5.6 and 5.7.

5.6 Conclusions

The estimator designed in this section made use of a kinematic model to describe the motion of the links constrained to a 2D space. This approach has been shown to be robust against parameter uncertainty due to its independence from the dynamic parameters such as mass, inertia, friction etc.

The tests results show that the estimator is more consistent than integrating the gyroscope signal. Results in Figure 5.6 and 5.7 show that the filter can correct for any initial conditions, whereas the gyroscope integral (GYR) maintains the initial error.

This chapter illustrated through simulation and real data that the kinematic model, in conjunction with an extended Kalman filter, produces reliable, accurate state estimation. The computational cost of the filter is not a cause for concern given the relatively cheap cost of computation. In practice, the STM32F4 could iterate through the filter within the sampling frequency of 100Hz.

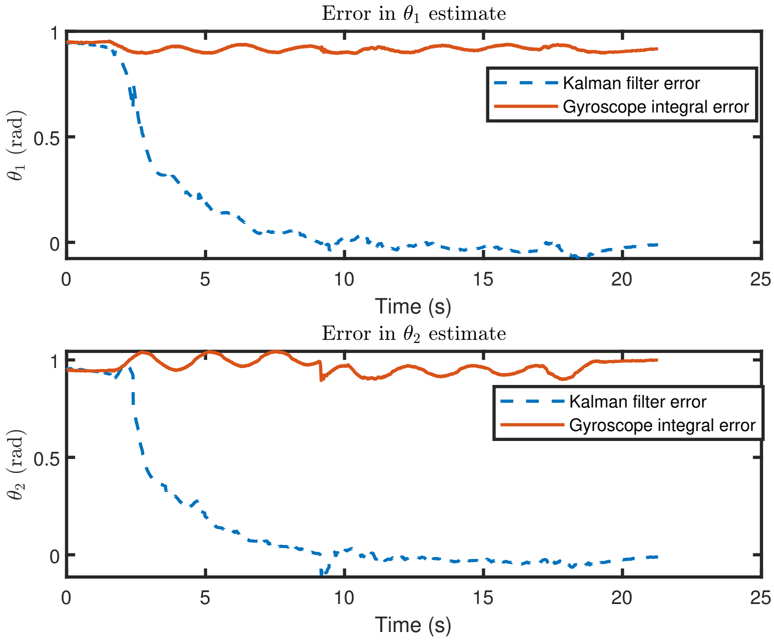

Figure 5.7: Error comparison of K-EKF estimate vs GYR signals using the combined test and erroneous initial conditions. ($0.05\ rad \approx 2.9^\circ$)

Future work should focus on estimating the bias and drift of the gyroscope signals. Drift and bias estimation will ensure that the estimation scheme developed in this section is commercially viable; given the vast distance which the PLIR will traverse in practice. The commercial system requires a 3D state estimator as a prerequisite for out-of-plane motion.

Chapter 6

Control Design

6.1 Introduction

Brachiating robots fall under a general class of under-actuated machines which can juggle, bat, catch, hop and walk. This class of robots share a requirement for oscillatory exchange between kinetic and potential energy in a gravitational field [42]. Under-actuated robots present a unique challenge because there are fewer actuators than degrees of freedom. Partial feedback linearization [27] and energy-regulation techniques [56][28] are prevalent in literature where the swing-up problem is solved. The swing-up problem involves applying torque to drive the robot to the vertically up position, which is typically a stable equilibrium. Once sufficiently close to the vertical equilibrium, i.e. in the basin of attraction, the control action switches from swing-up to stabilisation about the equilibrium typically using a linear controller.

Brachiation, on the other hand, involves driving the system to an unstable equilibrium point at which the gripper must attach to the structural member to prevent the robot from swinging back. An inability to reach the end-point and attach to the structural member fails the task of brachiation and can result in a disastrous fall. Software interlocks which ensure that the attached gripper can only open if the other gripper is attached can mitigate against this. This chapter addresses the issue of uncertain friction in the physical system and disturbances from the environment, both of which may result in a failed brachiation manoeuvre. Without the necessary software interlocks, this can translate to the PLIR falling off the line at great heights which would inevitably result in irreparable damage to the physical system shown in Figure 4.2. The problem of detachment before reaching the end-point is solved by a software interlock which prevents the fixed gripper from opening before confirmation that the free gripper has reached the line.

The work by [13] proposed a control architecture requiring accurate modelling of aerodynamics and manipulator dynamics. This approach, although successful, is not feasible for the BPLIR where the dynamics of the system are uncertain due to disturbance torques such as friction. [26] introduced the brachiation control problem and demonstrated the validity of learning a feed-forward torque signal to effect successful under-actuated control of dynamically dexterous manoeuvres. The approach has the added advantage of not requiring a model. However, it requires long training times for the system to learn the appropriate feed-forward signal. The long training times can be problematic given that the operating environment of the PLIR is dynamic, hence each subsequent swing is unique requiring a new learning cycle. The time-varying parameters would, in turn, require additional training cycles for every swing which would adversely affect the traversal time of the PLIR. It is also impractical to train the BPLIR online while it is in operation because of energy constraints. Another concern is that a feed-forward signal may not be impractical to learn in a fast-changing environment with wind and other environmental factors.

Perhaps the most significant contributions to this chapter come from [42][10] whereby [42] adopted biomechanically inspired design, to the encoding of the brachiation task via a lower-dimensional target and their systematic use of reverse-time symmetry (RTS). Reverse-time symmetry [10] is used in conjunction with a non-collated partial feedback scheme which encodes the task of brachiation to that of a virtual oscillator which admits reverse-time symmetry. Encoding a task via a reverse-time symmetrical oscillator is inspired by [10] , whose emphasis on solving tasks by recruiting natural orbits, which [10] showed reduces the effort of commanding any specific task to the selection of one or two key parameters.

The task which is of importance to this work is robust brachiation with uncertain friction parameters and model parameters. The uncertainty in the parameters simulates the real-world conditions in which the PLIR will be operating. There are a few assumptions about the physical structure of the system and its operation to simplify the design process. Firstly, the PLIR is symmetrical; therefore, any additional payload will maintain the symmetrical mass distributions of the system. Secondly, the robot performs brachiation while the fixed gripper is stationary. It is clamped firmly to the structural member which restricts any translational or out-of-plane motion. The single fixed point justifies the use of an acrobot model. Lastly, it assumed that any torque disturbances due to wind are slowly time-varying for the duration of a swing; hence, they are assumed constant.

This chapter partitions the design task into several sections. The first sections introduces collocated partial feedback linearization (CPFL) and explores the effects of plant/model

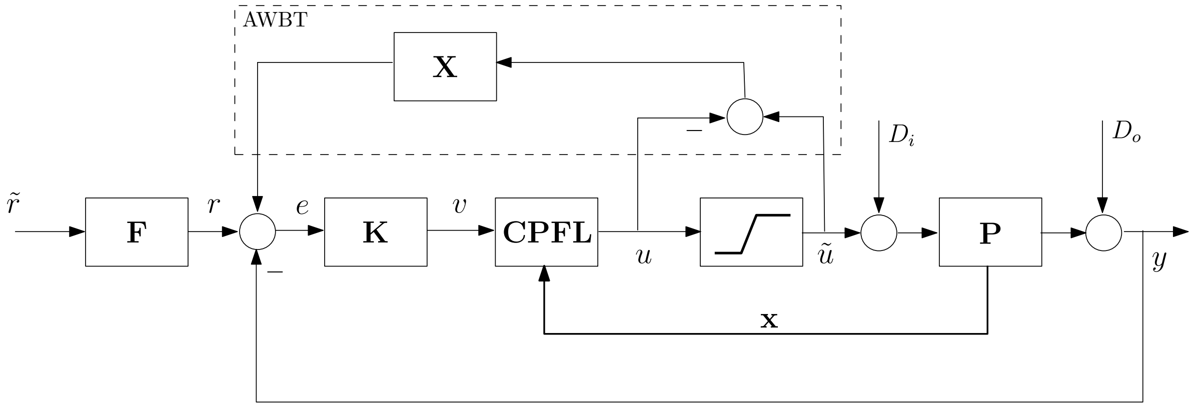

Figure 6.1: A block diagram illustrating the architecture the proposed control system

mismatch. The second section presents a discussion on the input torque limitation, which is inherent to the system, and the proposed conventional anti-windup (CAW) architecture to deal with the effects of it. The subsequent sections derive the technical specifications and present the design of a discrete-time quantitative feedback (QFT) controller. Finally, the results are presented for the plants with varying parameters.

6.2 Feedback Linearisation

Feedback linearization is a technique which transformations the nonlinear dynamic equations of a system to a linear input-output map [44]. This mapping must be a diffeomorphism if the transformed system is an equivalent representation of the original system. An outer-loop linear control strategy for the *transformed* system is then applied to achieve the desired performance specifications. Consider the general system of equations,

$$\dot{\mathbf{x}} = f(\mathbf{x}) + \mathbf{g}(\mathbf{x})\mathbf{u} \tag{6.1}$$

$$\mathbf{y} = h(\mathbf{x}) \tag{6.2}$$

where $\mathbf{x} \in \mathbb{R}^{\mathbf{n}}$ is the state vector, $\mathbf{u} \in \mathbb{R}^{\mathbf{p}}$ is the vector of inputs, and $\mathbf{y} \in \mathbb{R}^{\mathbf{m}}$ is the vector of outputs. It follows [44] that if the states of the transformed system $\mathbf{z}$ are the output $\mathbf{y}$ and the first $(n-1)$ derivatives then,

$$z = T(\mathbf{x}) = \begin{pmatrix} y \\ \dot{y} \\ \vdots \\ y^{n-1} \end{pmatrix} = \begin{pmatrix} h(x) \\ L_f h(x) \\ \vdots \\ L_f^{n-1} h(x) \end{pmatrix} \tag{6.3}$$

a feedback linearising control law (6.4) can be derived for a given output map $h(\mathbf{x})$ as ,

$$u = \frac{-{L_f}^n h(x) + v}{L_g L_f^{n-1} h(x)} \tag{6.4}$$

where Eq. (6.5) describes the Lie Derivative of h(x) along f(x),

$$L_f h(x) = \frac{\partial h(x)}{\partial x} f(x) \tag{6.5}$$

and Eq. (6.6) describes the n^{th} Lie derivative of h(x) along f(x),

$$L_f^n h(x) = \frac{L_f^{n-1} h(x)}{\partial x} f(x) \tag{6.6}$$

The challenge is the under-actuated nature of the system. Since under-actuated systems are not fully feedback linearisable [60][27], the focus is on *partial feedback linearisation* (PFL) whereby the directly actuated degree of freedom is linearised.

An important analysis is the effect that uncertain plant parameters have on the feedback linearization and ultimately the closed-loop performance of the plant. To do this we will first leverage the approach described in [60] and modify it to incorporate uncertain model parameters. Given the system model (4.5) and taking only the second-order derivative, the dynamics of link two are expressed by,

$$\ddot{q}_2 = n_{21}(-c_1 - g_1 - f_1) + n_{22}(-c_2 - g_2 - f_2) + n_{22}\tau \tag{6.7}$$

where n_{ij} represents elements of the mass matrix inverse, whilst c_i ,g_i and f_i represent elements of the Coriolis, gravity and friction vectors respectively. Special care should be taken not to confuse c_i with the shorthand for $\cos q_i$ employed in previous chapters.

Applying (6.5) to (6.7) results in

$$\tau = \frac{1}{n_{22}}(n_{21}(c_1 + g_1 + f_1) + n_{22}(+c_2 + g_2 + f_2) + v) \tag{6.8}$$

where v is an additional outer-loop control term (see Figure 6.1). If the friction,f_i, is not accounted for in the feedback linearisation law (6.8) i.e. $f_1 = f_2 = 0$, the resulting feedback linearised dynamics of the system are described by

$$\frac{d}{dt}\begin{pmatrix} z_1 \\ z_2 \\ \dot{z}_1 \\ \dot{z}_2 \end{pmatrix} = \begin{pmatrix} \dot{z}_1 \\ \dot{z}_2 \\ \zeta(z_1, z_2, v) - n_{11}f_1 - n_{12}f_2 \\ -n_{21}f_1 - n_{22}f_2 + v \end{pmatrix} \tag{6.9}$$

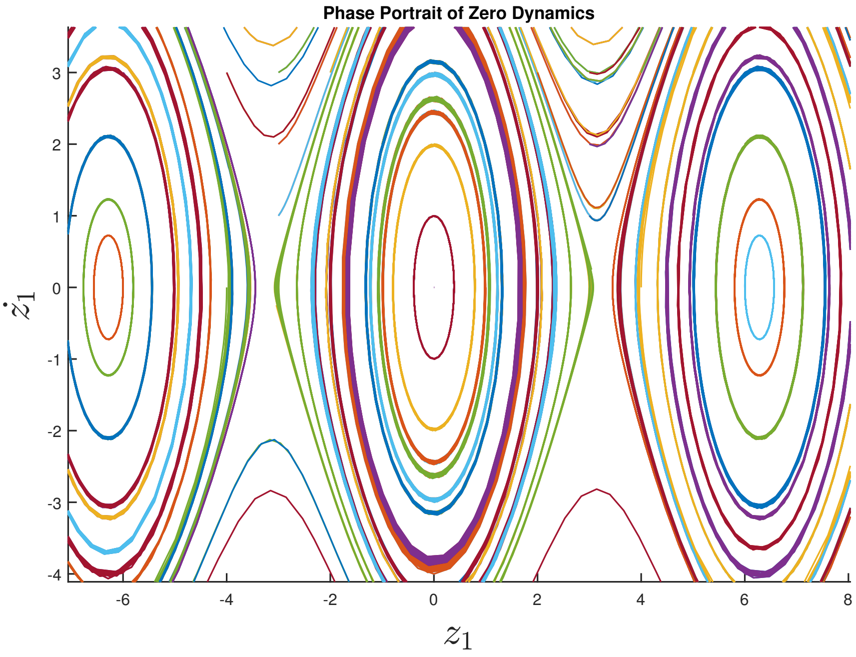

Figure 6.2: Phase portrait of zero dynamics with no friction showing the various limit cycles

Where the term $\zeta(z_1, z_2, v)$ describes the zero dynamics of the system discounting friction, where

$$\zeta(z_1, z_2, v) = (c_1 + g_1)(\frac{n_{12}n_{21}}{n_{22}} - n_{11}) + \frac{n_{12}}{n_{22}}v \quad ; n_{22} \neq 0 \tag{6.10}$$

The concept of zero dynamics of a nonlinear system was introduced about thirty years ago as nonlinear analogue of the concept of transmission zero of a system [68]. Zero dynamics also refer to the unforced internal dynamics of a system or "free response". In each instance, it is important to ensure that the internal dynamics are stable to determine global asymptotic stability of a system which in turn determine whether feedback control will be effective at meeting specifications.

Stability is an important factor to consider especially for PFL whereby friction is not accounted for. The system is expected to converge on a zero-energy state because of the non-conservative nature of the friction which will ensure the system energy is extracted, generally in the form of heat, until the system has zero energy.

The phase portrait for the zero dynamics of the system are shown below for the two cases; a) a friction-less system with arbitrary initial conditions and; b)friction incorporated into the system model using the approximation (4.11).

The friction-less case is illustrated above in Figure 6.2. In this instance, the system

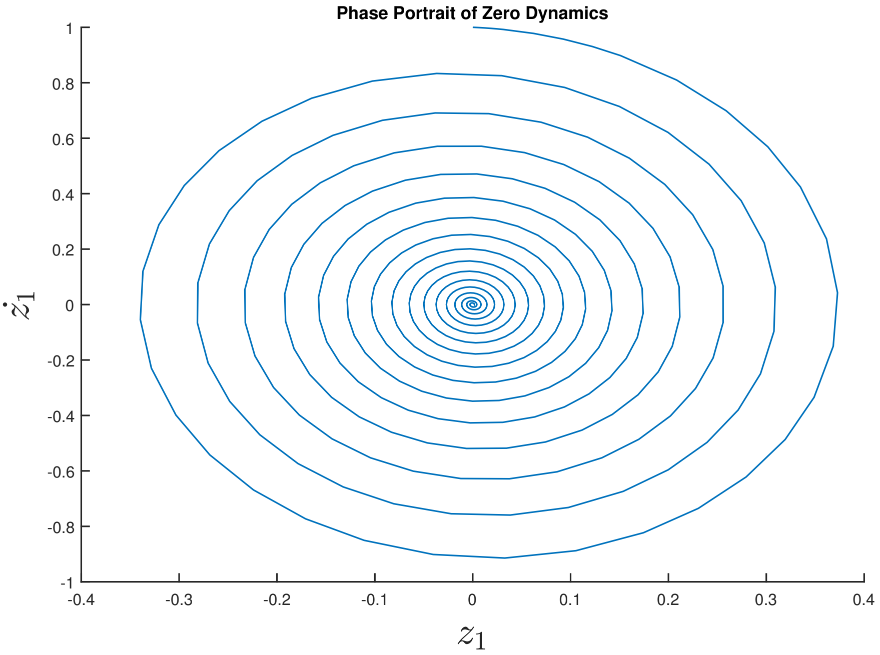

Figure 6.3: Phase portrait of zero dynamics with friction showing the stable focus at the origin

enters a limit cycle regardless of initial conditions. The absence of friction results in a marginally stable system in Lypanov sense oscillating about the equilibrium point at the origin which corresponds to the vertically down position.

Figure 6.3 shows the effects of the non-conservative nature of friction. The trajectory of the zero dynamics regardless of the initial conditions converges on zero. Hence the system, with friction, is exponentially stable with a stable focus at the origin.

The phase portraits show that the system is stable for collocated PFL with or without friction. The uncertain parameters of the system are, to a certain degree, regarded as an additional friction term. Hence, the system is stable regardless of parameters variation. The next step in the design is to ensure that the system tracks the reference signal despite the uncertain friction parameters.

6.3 Technical Specification

Technical specifications inform the design of a feedback controller. In this section, the technical specifications for the closed-loop system are determined based on the system shown in Figure 6.4.

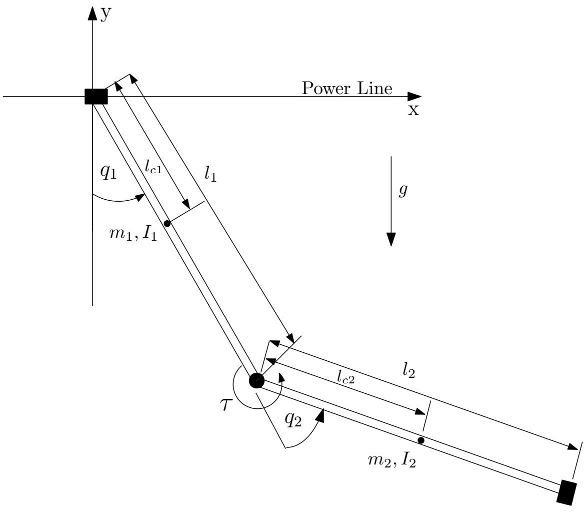

Figure 6.4: A graphical representation of the acrobot

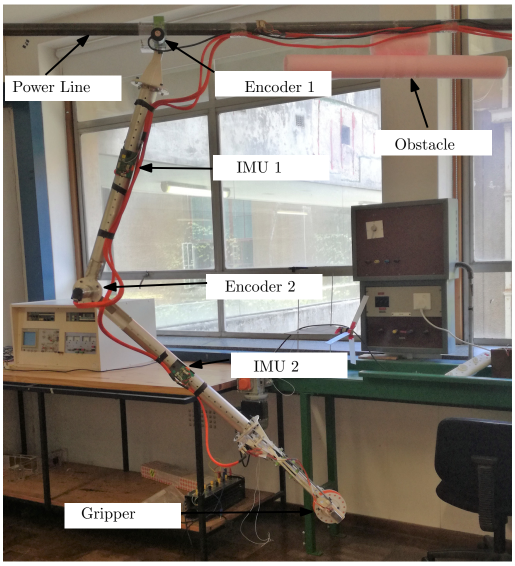

Figure 6.5: A snapshot of the experimental setup in the lab

Closed-loop Speed

The speed of the closed-loop response is desired to be faster than the open-loop (OL) dynamics for the feedback control system to have adequate control over the system [77]. The first step is to work out the open-loop speed of the system. The approximation of the system as a simple pendulum was useful in determining the OL speed. The period of a simple pendulum with radial distance (r_{CoM}) to the centre of mass from the pivot is

$$T = 2\pi\sqrt{\frac{r_{CoM}}{g}} \tag{6.11}$$

The location of the centre of in a mass of the PLIR (see Figure 6.4) is given by,

$$x_{CoM} = \frac{m_1 l_{c1} sin(q_1) + (l_1 sin(q_1) + l_{c2} sin(q_1 + q_2))m_2}{m_1 + m_2} \tag{6.12a}$$

$$y_{CoM} = \frac{m_1 l_{c1} cos(q_1) + (l_1 cos(q_1) + l_{c2} cos(q_1 + q_2))m_2}{m_1 + m_2} \tag{6.12b}$$

Equation (6.11) shows that the period of the simple pendulum is proportional to r_{CoM}, the distance to the centre of mass. From (6.12) it is seen that the radial distance to the centre of mass is given by,

$$r_{CoM} = \sqrt{x_{CoM}^2 + y_{CoM}^2} \tag{6.13}$$

To find the fastest open-loop period it is required that the minimum of (6.13) is computed. Minimising x_{CoM} and y_{CoM} it can be shown that the radial distance is minimised when $q_2 = \pi$ which corresponds to the PLIR folding into itself. Evaluating the radial distance at $q_1 = 0$ for simplicity, the minimum radial distance is

$$|r_{CoM}|_{min} = \frac{m_1 l_{c1} + (l_1 + l_{c_2})m_2}{m_1 + m_2} \tag{6.14}$$

Substituting the optimised parameters from Table 4.3 into (6.14) and then into (6.11) the fastest time period for the system is found to be

$$T_{min} = 1.57s \tag{6.15}$$

The period is the time it takes for the BPLIR to swing back to the starting position; hence the time for a half swing is expected to be half the period $\frac{T_{min}}{2}$. The technical specification for the closed-loop response is designed to be at least twice as fast as the open-loop period. Therefore, the desired settling of the closed-loop system for the fastest open-loop response speed is

$$\tau_{settling} \leq 0.39s \tag{6.16}$$

Due to the system rarely operating in a configuration which requires this fast response. The designed specification was relaxed to $\tau_{settling} = 0.53s$ which corresponds to a time-constant of $\tau \approx 0.13$.

Steady State Error

The task of brachiation involves driving the BPLIR to an unstable point. The instability makes it difficult to ensure zero steady-state error because, during a swing motion, there is no stable state. However, tight trajectory tracking is necessary for ensuring that brachiation is successful.

The uncertain system response model derived in (4.16) shows that the gain for θ_2 varies between $[0.19, 0.35]$ which represents a 30% deviation from the median. It is reasonable to design the inner-loop to provide a worst-case steady-state position tracking error of 10% on the closed-loop. The response time and steady-state error result in the following closed-loop tracking specifications.

$$\left|\frac{0.9}{(\frac{s}{10})^2 + 0.15s + 1}\right| \leq \frac{FL}{1+L} \leq \left|\frac{1.1}{(\frac{s}{26})^2 + 0.077s + 1}\right| \tag{6.17}$$

In tandem with this tracking specification, the robust stability margin is

$$\left|\frac{1}{1+L}\right| \leq 3dB \; \forall \omega \tag{6.18}$$

where L represents the loop gain.

Control Effort

The OEM motor has inherent limitations on the capabilities of the hardware to produce continuous torque throughout the trajectory. The theoretical torque limit, $|\tau_{max}|$, is 20Nm however, in the practical setup the actual bound was around 15Nm.

Translating the inner-loop torque limit required an analysis of the partial feedback linearization. The inner-loop torque specification is translated into an outer loop v_{max} specification by implementing the inverse of partial feedback linearization. The equation to be solved for is (6.4) using the optimised model parameters and the maximum input torque of 20Nm. Hence

$$|v_{max}| = |\tau_{max} n_{22} - n_{21}(c_1 + g_1 + f_1) - n_{22}(c_2 + g_2 + f_2) \tag{6.19}$$

The solution of (6.19) found that the magnitude of the outer-loop signal must be limited to,

$$|v_{max}| \leq 220\ Nm$$

The outer-loop control signal limit v_{max} was computed over a region of the state space bounded by,

$$\begin{gathered} -\frac{\pi}{2} \leq q_1 \leq \frac{\pi}{2} \\ -\pi \leq q_2 \leq \pi \\ -4 \leq \omega_1 \leq 4 \\ -4 \leq \omega_2 \leq 4 \end{gathered}$$

The state space bounds were determined using offline trajectory generation. The outer-loop limit v_{max} is state dependant and varies depending on the configuration of the system. Therefore, in addition to designing for $v_{max} < 220$, an anti-windup framework is discussed in Section 6.4.1 which deals with the inevitable case of actuator saturation.

If we assume a unit step in the reference signal $\tilde{r}$ shown in Figure 6.1, the frequency design specification for control action is then

$$\left|\frac{FK}{1+L}\right| \leq 220 \tag{6.20}$$

6.4 Design

This section presents a 2 degree-of-freedom robust controller design. The controller is designed using quantitative feedback theory [36] [74] and the QFT MATLAB Toolbox

[46]. The idea is to design a single controller which can stabilise plants $P_i \in \mathbf{P}$ under all parameter variations.

Pre-filter [45] design ensures that the tracking behaviour of the system is within specifications. The controller is designed using continuous-time techniques with the effects of discretisation approximated by,

$$P_z(w) \approx P_s(w)(1 - \frac{wT_s}{2}) \tag{6.21}$$

The discrete (z) to continuous (w) plant conversion are related by the bi-linear transform.

$$z = \frac{1 + w\frac{T}{2}}{1 - w\frac{T}{2}} w = \frac{2}{T}\frac{z-1}{z+1} \tag{6.22}$$

Applying (6.21) to (4.16) results in a continuous-time approximate of the discrete-time system.

6.4.1 Actuator Constraints

All real-world systems have actuator constraints. For the BPLIR, these are physical limitations on the maximum torque which can be generated by the motor. This constraint can be represented as a nonlinear operator, $\mathbf{N}$, as illustrated in Figure (6.6).

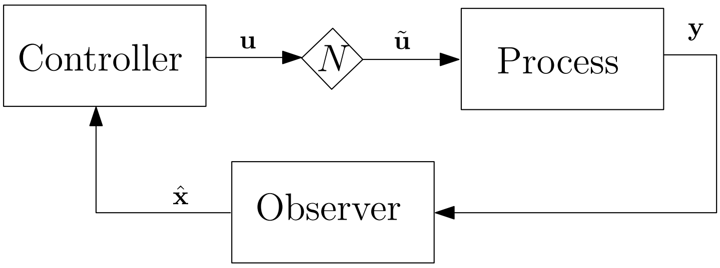

Figure 6.6: A block diagram which illustrates how the input nonlinearity acts on the closed-loop system.

As a result of the nonlinearity, the actual plant input $\tilde{\mathbf{x}}$ will be different from the output of the controller. *Controller windup* is interpreted as an inconsistency between the controller output and the states of the controller. Anti-reset windup [18] or back-calculation & tracking [33] is an effect observed in PI and PID controllers designed for SISO systems with a saturating actuator.

In short, if the error signal is large, the control signal gets saturated at the high limit of u_{max}. If this continues for a sustained period, the integrator will continue to accumulate the error causing the control signal to become more saturated.

The control signal will thus not leave the limit u_{max} until the error reverses for a sufficient period to decrements the prior accumulated error [18]. The adverse effect of this integral windup is in the form of large overshoots in the output and possible instability.

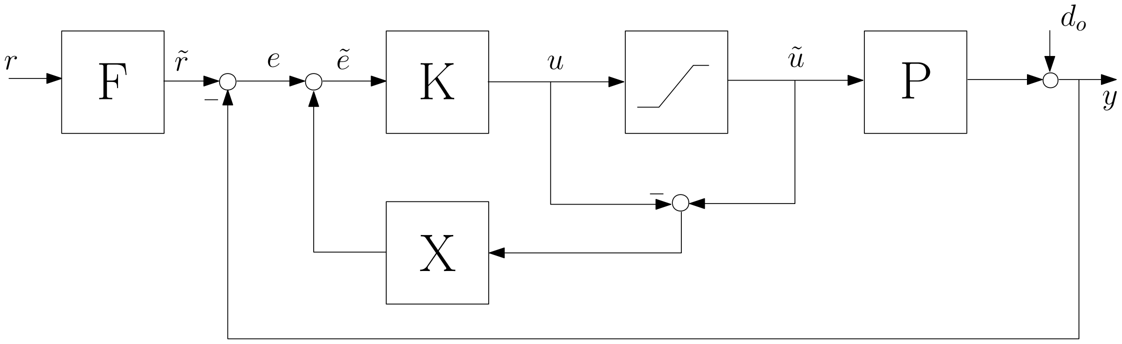

Figure 6.7: Figure illustrating the block diagram of a conventional anti-windup scheme

Kothare et al. [25] presents a unification of anti-windup bump-less transfer (AWBT) techniques. AWBT is an approach which can mitigate the effects of controller windup and improve closed-loop performance. The approach set out [25], which is of importance to this project is the conventional anti-windup shown in Figure 6.7.

The CAW architecture works by artificially decreasing the error signal **e** until such a time that the signal $\tilde{e}K$ is equal to the saturation limit. The feedback structure drives the signal $\hat{u} - u$ to zero when saturation occurs through the gain X >>1, as illustrated in Figure 6.7.

6.4.2 Loop Shaping

This section deals with the design for the outer loop controller (K) and the pre-filter (F). The QFT Toolbox on MATLAB was used to design the robust controller. The first step is to shape the loop of the response based on the specifications detailed in (6.17)(6.18)(6.20). The Nichols chart is the main design domain for loop-shaping. Figure 6.8 shows the resultant nominal plant and the design bounds based on the specifications.

The first step in the design was to introduce a gain (K) to meet the specifications at low frequencies as seen in Figure 6.8 and this was a negative gain for plant sign correction. Computing on the Nyquist plot, an additional gain adjustment of $47dB$ meet all the closed-loop specifications for the system.

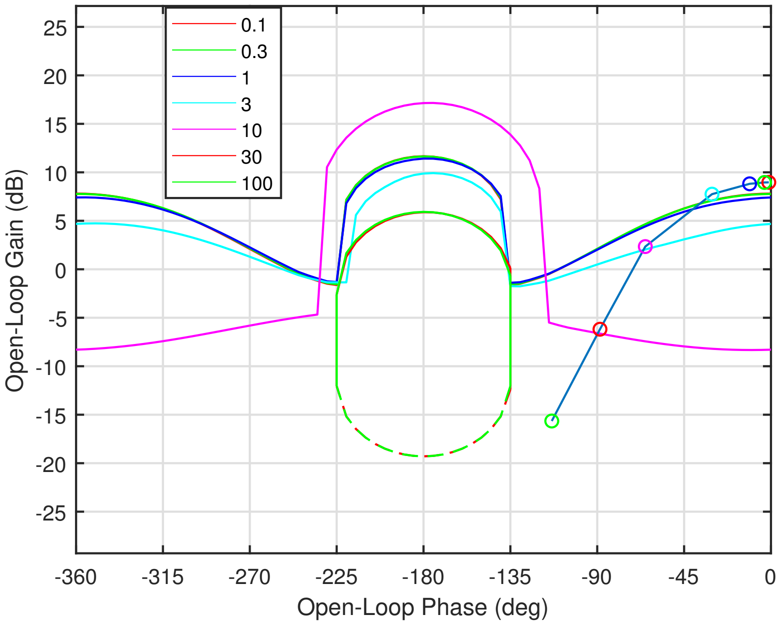

Figure 6.8: An image illustrating the closed-loop bounds on the Nichols chart over the design frequency range and the resultant closed-loop controller performance K

The designed proportional controller, K, in the w-domain is described by

$$K(w) = -216 \tag{6.23}$$

A steady state specification was not included because the system is in constant motion while brachiating i.e. it will only have steady-state position at the start and end of swings. Since there is no steady-state specification, it was unnecessary to incorporate an integrator instead, the designed pre-filter bounds the error dynamics to a reasonable margin (10%). The filter does not have a dependence on w hence the discrete-time filter and the continuous-time filter are equivalent,

$$K(z) = K(w)$$

6.4.3 Tracking Design

Pre-filter design or tracking design addresses the issue of closed-loop tracking. The design is performed using bode plots, and the idea is to shape the tracking behaviour of the system through pole/zero placements. Shown below in Figure 6.9 are the Bode plots of the system before the pre-filter (left) and after the pre-filter is introduced.

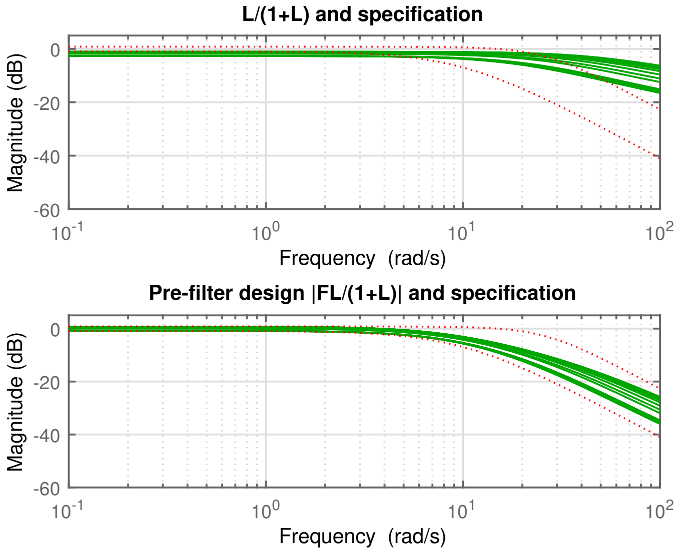

Figure 6.9: Bode plots of the tracking behaviour of the system before the pre-filter (left) and after the pre-filter (right)

It is seen in Figure 6.9 that the response before the pre-filter is largely within the specification at lower frequencies. This is not the case for the higher frequencies where the desired roll-off of $-40dB/decade$ begins around $8rad/s$. The system response instead rolls off at around $50rad/s$ at $-20dB/decade$. The roll-off requirement necessitates the introduction of a pole at a frequency of $8rad/s$ before the peak of the bode plot. The pole ensures that the roll-off of the plants is $-40dB/decade$ which is in line with the desired bode envelope.

$$F(w) = \frac{10.61}{w + 8.616} \tag{6.24}$$

The addition of a pole necessitated a minor gain adjustment of $1.8dB$ to meet specifications. The gain adjustment ensures that the lower bound of the plants are within the tracking bounds.

6.5 Results

This section presents simulation results for the closed-loop control system. It is important to note the key technical specifications of the closed-loop system are:

1. Steady-state tracking error of $\leq 10\%$
2. Settling time of $\leq 0.39s$
3. Control action not exceeding $220Nm$.
4. Input and Output Disturbance rejection

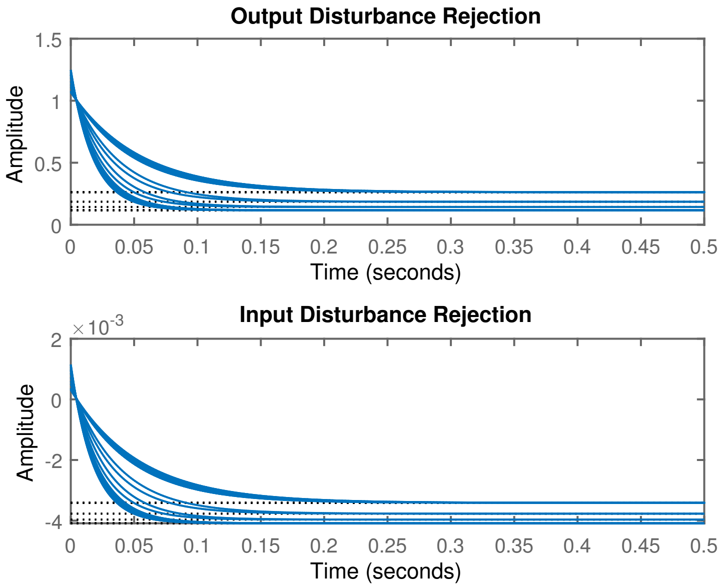

Figure 6.10: An image illustrating the closed-loop input (bottom) and output (top) disturbance response of the system with controller K, and the pre-filter F

The output response of the system to a unit step disturbance (input/output) illustrate sufficient capabilities to reject the disturbance within the specified settling time of 0.39s. The output disturbance response converges on zero within 0.15s which is twice as fast as the specification. The input disturbance rejection achieves this in a similar amount of time however it should be noted that the magnitude of the input disturbance on the output is approximately $4mrad =$ or less than $1°$.

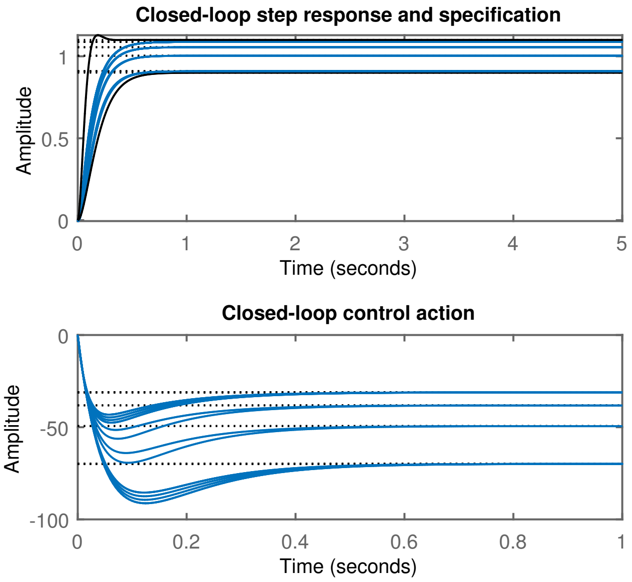

Figure 6.11: An image illustrating the robust position reference tracking behaviour of the system for the plant family (blue) versus the specifications (black)

The output tracking performance shown in Figure 6.11 shows that the designed closed loop system (blue) against the specifications of the design (black). The response shows that the closed-loop system meets the closed-loop tracking specifications, particularly 10% steady-state error as well as the settling time of ¡0.39s. The control action required is also well within specification of $220Nm$ achieving steady-state tracking, settling time and disturbance rejection while requiring maximum control action of 100Nm.

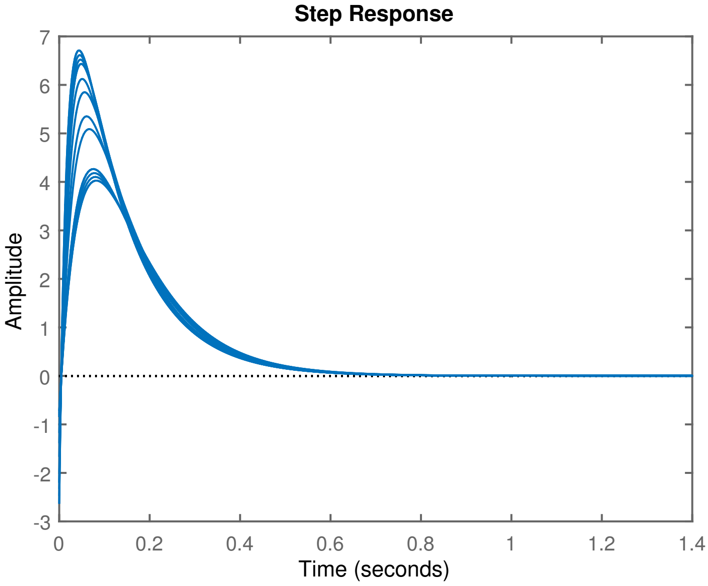

Figure 6.12: An image illustrating the velocity response of q_2 to a unit step. The steady-state error converges on zero

Lastly, it should be noted that the velocity of q_2 converges on zero the system response settles. This is important due to the requirement that the BPLIR reach the target point with zero velocity to prevent mechanical damage.

6.6 Discussion

The controller presented in this section stabilised the plants $P_i \in \mathbf{P}$. The resultant controller was a simple proportional controller with sign correction.

The closed-loop tracking response shows that the plant behaves as per technical specifications, especially for a unit step. The step test is a benchmark for controller performance. However, the physical system is unlikely to be subjected to a constant step input. The input, as detailed in Chapter 7 is a time-varying adaptive signal. The adaptive nature of the trajectory generator ensures that the difference between the reference signal and the current state is small.

The more concerning the result of this controller is the disturbance rejection capabilities. Zero steady-state error is not be designed for because it does not make sense for the operational requirements of the BPLIR. The position of the end-effector does not reach a 'steady-state' because the position is not stable along the trajectory given the under-actuated nature of the BPLIR. Added to this is that the only equilibrium points for the system are vertically down and vertically up, two modes which are not of interest for brachiation.

Another reason for keeping the controller simple is the nature of the zero-dynamics of link 1. Figure 6.3 shows that the zero dynamics are stable under unknown friction parameters and enter a limit cycle for zero friction. Hence if the controller is proportional, there is no alteration to the zero dynamics of the system because the controller is an algebraic scaling on the torque signal; hence it does not alter the zero dynamics of the system.

The input disturbances are simply the inverse partial feedback linearization on any inner-loop disturbances. The translation of the input torque disturbance to the outer loop simplifies analysis for the controller. A maximum inner-loop torque disturbance of 20 Nm translates to a maximum outer-loop input disturbance 220 Nm as per equation 6.19. This disturbance of 220 Nm would attenuate to 0.88 or by 99.6% according to the closed-loop response in Figure 6.10.

6.7 Conclusion

This chapter has presented the control architecture of the BPLIR, which comprise of partial feedback linearisation, loop shaping controller and pre-filter. It was shown how an AWBT framework in the form of CAW could work to mitigate the effects of actuator saturation.

The inner-loop position controller met all three specifications, which were a control effort (6.20), robust tracking (6.17) and robust stability to input and output disturbances (6.18).

Chapter 7

Trajectory Generation

7.1 Introduction

Robot motion or trajectory planning is calculating feasible configurations through which a robot manipulator can move from the start point to the desired endpoint. It forms the basis of autonomous robots which need to navigate a dynamic environment such as the real world. This navigation needs to take into consideration the changing environment within which the robot is operating and incorporate dynamic constraints into planning the trajectory.

In the context of the BPLIR, this would mean avoiding obstacles on the line such as dampers, spacers and performing pylon-to-pylon locomotion. Path generation involves finding a series of points in the configuration or joint space which efficiently avoid any obstacles. The trajectory generation scheme proposed in this chapter starts by presenting a path in the configuration space and showing that it does not need to be converted to a trajectory to accomplish the task.

The main inspiration is [42][10] who have shown that for the horizontal structural member, an orbit or trajectory which admits reverse time symmetry can simplify the control of an under-actuated dynamic system such as the acrobot. Applying collocated feedback linearization allows direct control of the relative angle between the links θ_2 as shown in Figure 5.2. A trajectory which admits RTS is presented based on the arc-tangent function.

An essential point in the design of the trajectory generator is the problem of friction. Given that the system friction is uncertain, it is challenging to generate a feasible feedforward trajectory given the time-varying nature of the parameters. The parameter T, representing the duration of a single swing, is unknown and varies depending on the initial geometric configuration and initial dynamic behaviour of the robot. The uncertainty

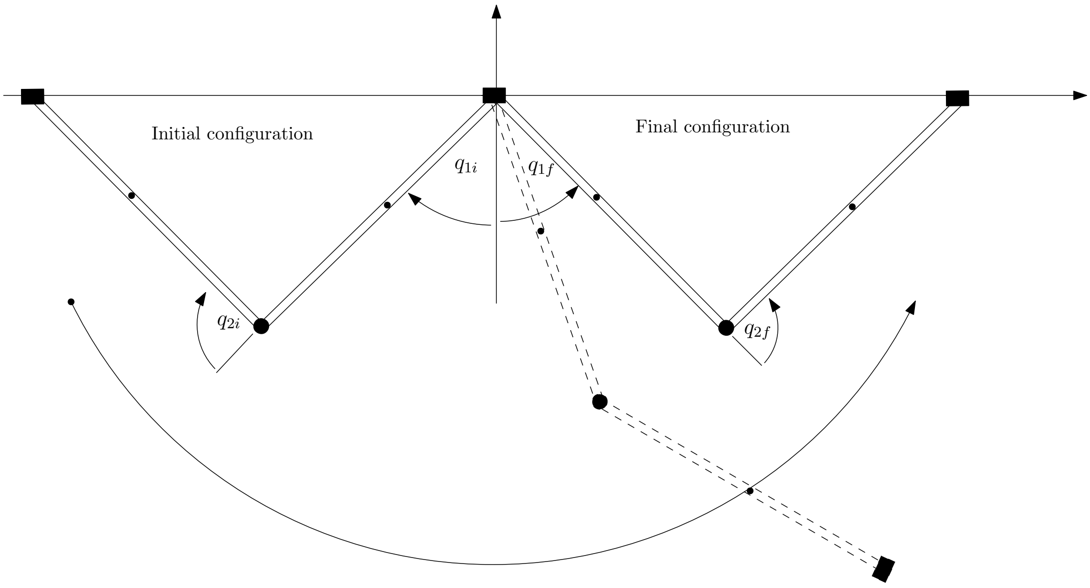

Figure 7.1: An image illustrating a brachiation manoeuvre for the BPLIR on a horizontal structural member

of the environment as well as physical parameter variations makes it difficult to find an explicit time-based trajectory equation. The proposed adaptive trajectory generator counteracts this limitation by compensating for the energy loss due to friction online. The parameters of the path are adjusted during a swing in response to the energy loss in the system.

7.2 Path Planning

Path planning generates a feasible path from a starting configuration $\mathbf{q}_{init}$ to the goal configuration $\mathbf{q}_{final}$ which avoids obstacles along the line. The difference between a path and a trajectory is that a path is independent of time. Adding a timestamp to the points along a path converts it to a trajectory. A path tells the robot *where it should be*, and a trajectory tells the robot *when it should be there.*

First, we consider a path, which is bounded by the constraints (7.1)(7.2) and (7.3) . The first constraint, (7.1), states that the final configuration at time T is a mirror image of the initial configuration for the horizontal scenario ($q_{line} = 0$).

$$\mathbf{q}(0) = \mathbf{q}_{init} = -\mathbf{q}(T) \tag{7.1}$$

The second constraint (7.2) is that the velocity at the start and end of the path equal to zero. This constraint corresponds to reaching the line at zero velocity to avoid damage to both the BPLIR and the high voltage power line

$$\dot{\mathbf{q}}(0) = \dot{\mathbf{q}}(T) = 0 \quad \forall\, q_{line} \tag{7.2}$$

The last constraint (7.3) states that the desired initial and final acceleration is zero.

$$\ddot{\mathbf{q}}(0) = \ddot{\mathbf{q}}(T) = 0 \quad \forall\, q_{line} \tag{7.3}$$

There is a family of polynomials and other smooth functions that fulfils the constraints. However, an arc-tangent trigonometric function simplifies computation since it consists of fewer parameters than a polynomial. Robot initialisation addresses the problem of obstacle avoidance. Since the final and initial configurations are mirror images, if the desired final configuration overcomes an obstacle on the power line, then the initial configuration should be a mirror image of the final configuration.

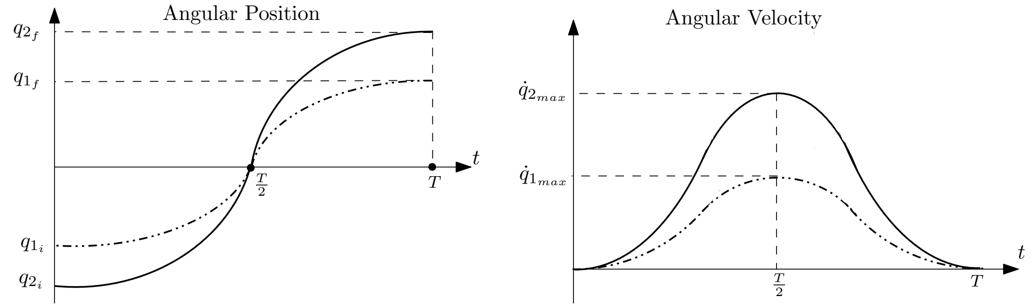

Figure 7.2: A general trajectory for q_1 and q_2 which admits reverse-time symmetry is described by an arctangent function

The trajectory of link i is described by,

$$q_i(t) = q_{i_f}\frac{2}{\pi}\arctan(t - \frac{T}{2}) \quad i = 1, 2 \tag{7.4}$$

Differentiating with respect to time produces the corresponding velocity profile

$$\dot{q}_i(t) = \frac{2}{\pi}\frac{q_{i_f}}{1 + (t - \frac{T}{2})^2} \tag{7.5}$$

If the two links pass the vertically down symmetry point at the same time, a simplified expression for the path can be found. The conversion of the trajectory into a time independent path involves making time (t) the subject of (7.4)(7.5) and equating them to one another. This then gives a time-independent relation of the angles

$$q_{2sym} = q_1\frac{q_{2_f}}{q_{1_f}} \tag{7.6}$$

And the corresponding path velocity is given by

$$\dot{q}_{2sym} = \dot{q}_1 \frac{q_{2_f}}{q_{1_f}} \tag{7.7}$$

A path which admits RTS is then determined as a function of the unactuated angle q_1. This parametrisation means that the focus is commanding q_2 in response to q_1 such that the resulting path or trajectory admits reverse-time symmetry. This approach allows the design to be more intuitive when dealing with uncertain and unknown torque disturbances which can alter the initial trajectory. Any torque disturbance on the links can be interpreted as a distortion that introduces phase shift and attenuation on the initial path. This distortion is illustrated below for an arbitrary link whereby a torque disturbance in the form of friction, aerodynamic drag or constant wind in the environment impedes the motion of the links.

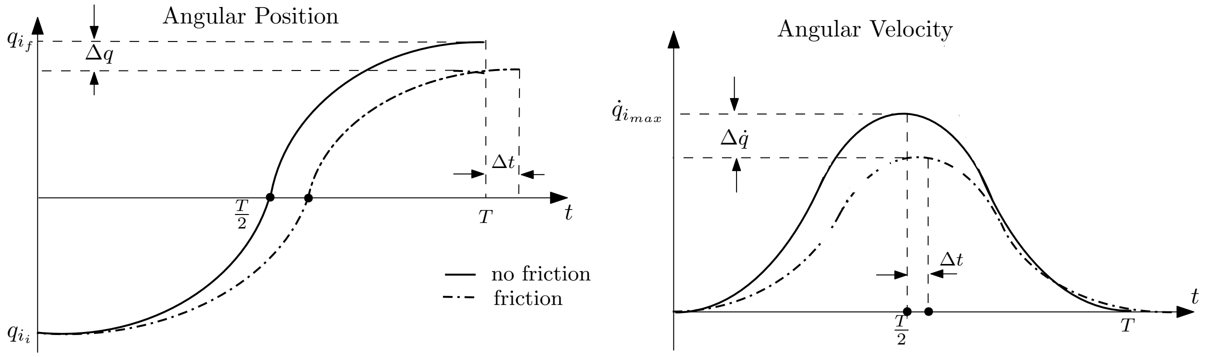

Figure 7.3: Image illustrating the trajectory distortion as a result of non-conservative torque disturbances acting on the system

It is helpful to analyse the energy rate or power dissipation of the system. It was shown in [40] that the energy rate $\dot{E} = \dot{\mathbf{q}}^T \tau$ for the frictionless case, where τ denotes the actuation vector. A minor modification is introduced in this chapter to illustrate the effect of friction $\mathbf{f}(\dot{\mathbf{q}})$. The energy of the system is given by

$$E = \frac{1}{2}\dot{\mathbf{q}}^T \mathbf{M}\dot{\mathbf{q}} + \mathbf{V}(\mathbf{q}) \tag{7.8}$$

Taking the time-derivative of (7.8) the energy rate is then given by

$$\dot{E} = \dot{\mathbf{q}}^T \mathbf{M}(\mathbf{q})\ddot{\mathbf{q}} + \mathbf{\frac{1}{2}}\dot{\mathbf{q}}^{\mathbf{T}}\dot{\mathbf{M}}(\mathbf{q})\dot{\mathbf{q}} + \dot{\mathbf{q}}^{\mathbf{T}}\mathbf{g}(\mathbf{q}) \tag{7.9}$$

Substituting (4.5) into (7.9) results in

$$\dot{E} = \dot{\mathbf{q}}^T(-\mathbf{C}(\mathbf{q},\mathbf{q})\dot{\mathbf{q}} - \mathbf{g}(\mathbf{q}) - \mathbf{f}(\dot{\mathbf{q}}) + \boldsymbol{\tau}) + \mathbf{\frac{1}{2}}\dot{\mathbf{q}}^{\mathbf{T}}\dot{\mathbf{M}}(\mathbf{q})\dot{\mathbf{q}} + \dot{\mathbf{q}}^{\mathbf{T}}\mathbf{g}(\mathbf{q}) \tag{7.10}$$

which reduces to

$$\dot{E} = \dot{\mathbf{q}}^T\big(\frac{1}{2}\dot{\mathbf{M}}(\mathbf{q}) - \mathbf{C}(\mathbf{q},\dot{\mathbf{q}})\big)\dot{\mathbf{q}} + \dot{\mathbf{q}}^{\mathbf{T}}\big(\boldsymbol{\tau} - \mathbf{f}(\dot{\mathbf{q}})\big) \tag{7.11}$$

The matrix $\frac{1}{2}\dot{\mathbf{M}}(\mathbf{q}) - \mathbf{C}(\mathbf{q},\dot{\mathbf{q}})$ is skew-symmetric [40]. An important property of skew-symmetric matrices $\mathbf{\Phi}$ is that

$$\mathbf{z^T \Phi z = 0} \quad \forall \mathbf{z}; \quad \mathbf{z} \in \mathbb{R}^{\mathbf{n}} \tag{7.12}$$

Hence the energy rate is described by

$$\dot{E} = \dot{\mathbf{q}}^T\big(\boldsymbol{\tau} - \mathbf{f}(\dot{\mathbf{q}})\big) \tag{7.13a}$$

$$\dot{E} = \dot{q}_1(\tau_1 - f_1) + \dot{q}_2(\tau_2 - f_2) \tag{7.13b}$$

Since $\tau_1 = 0$, the resulting expression for the energy rate of the system is,

$$\dot{E} = \dot{q}_1(-f_1) + \dot{q}_2(\tau_2 - f_2) \tag{7.14}$$

It is clear from (7.14) that the friction or external forces acting on link 2 can be compensated for directly through the application of torque τ_2. In addition, for energy to be pumped into the system, i.e to have a positive energy rate, the applied torque in link 2 needs to satisfy

$$\tau_2 > f_1\frac{\dot{q}_1}{\dot{q}_2} + f_2 \quad , \quad \dot{q}_2 \neq 0 \tag{7.15}$$

This analysis of the energy rate forms the basis of our adaptive path algorithm which is designed to ensure that the PLIR indeed reaches the line. The observation is that the friction in link 1 cannot be compensated for directly and as a result requires that the angle q_2 is adjusted dynamically in response to $q_1 + \Delta q_1$.

If the angle q_{target}, shown in Figure 7.4, is the angular difference between the line and the end-effector for a symmetrical BPLIR, then it can be described by (7.16)

$$q_{target} = q_1 + \frac{1}{2}q_2 \tag{7.16}$$

To maintain constant q_{target} given some unknown distortion Δq_1 to q_1 for example if

$$q_1 \rightarrow q_1 - \Delta q_1$$

then

$$q_2 \rightarrow q_2 + 2\Delta q_1$$

The above analysis offers a framework to generate a dynamic trajectory online while

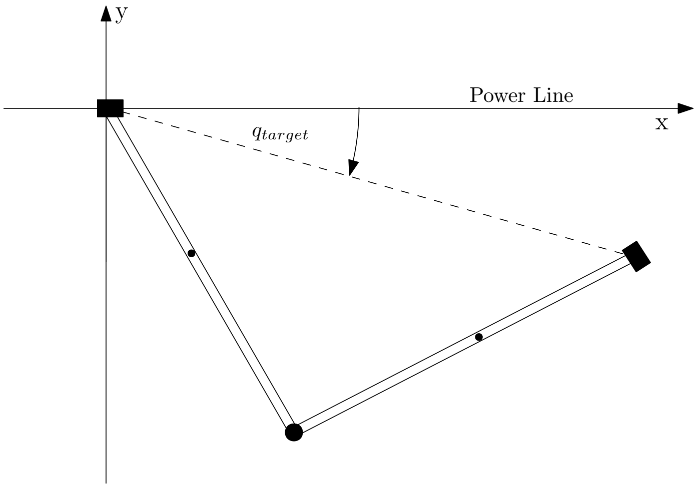

Figure 7.4: Image illustrating the angle q_{target} for a BPLIR whereby the incline of the line is zero

considering the effects of friction on the system. The difficulty in implementation is that the time-scaling of the trajectory needs to be exact. Failure to do this can result in erroneous compensation because a delayed trajectory is indistinguishable from distortion due to friction and vice versa. A path adaption algorithm that adjusts the path online overcomes the limitations of a time-dependent trajectory.

7.3 Path Adaption

The previous section proposed a reverse-time symmetrical path for solving the horizontal brachiation problem. The section further introduced the torque disturbance problem and how an adaptive trajectory might overcome it. This concept is expanded on in this section, whereby we show how the reference to link 2 can be adapted online to ensure successful brachiation regardless of friction. The adaptive path overcomes the time dependence issue, which is the main disadvantage of a trajectory.

In summary, the trajectory generator produces two paths, one which is reverse-time symmetrical and another which aims to minimise the perpendicular distance to the line. Linear interpolation that works by adjusting a weighting between the two ensures that the BPLIR responds predictably to accomplish the task of reaching the line. The methodology focuses on y because the RTS swing will ensure that the BPLIR mirrors the initial configuration when close to the target, hence the span of the BPLIR will always be sufficient. Consider the distance between the end effector and the line, given by

$$y = -l_1 \cos q_1 - l_2 \cos (q_1 + q_2) \tag{7.17}$$

If the objective is chosen such that $y = 0$ then the reference to link 2 q_{2ref} should be commanded such that

$$q_{2_{ref}} = \arccos\left(-\frac{l_1}{l_2}\cos q_1\right) - q_1 \tag{7.18}$$

If the two links are equal then 7.18 evaluates to

$$q_{2ref} = -2q_1 \tag{7.19}$$

Equations (7.6) and (7.18) are used together to determine an overall trajectory for link 2. The tricky aspect of this approach is deciding on the switching criterion between (7.6) and (7.18). It is not useful to utilise (7.18) in the first half of the swing because of the inherent symmetry in the equation. This symmetry will cause the second link to drive back to the starting point instead of forwards towards the target. Hence it makes sense to use (7.6) in the first half of the swing and gradually switch to (7.18) after the BPLIR passes the vertically down symmetry point. The switch is designed to be gradual to avoid a bump in the reference and control signal which may adversely affect the synchronicity of the swing

The switching mechanism is a linear interpolation between the two paths or *fuzzy inference.* The decision was whether to follow (7.6) or (7.18). If we create a decision weighting $\digamma$ such that,

$$\digamma = \begin{cases} 1 & \frac{1}{|q_{1f}|}|q_1| > 1 \\ 0 & \frac{1}{|q_{1f}|}|q_1| < 0 \\ \frac{1}{|q_{1f}|}|q_1| & else \end{cases} \tag{7.20}$$

Then we can generate a new trajectory $q_{2adjust}$ as

$$q_{2ref} = \begin{cases} q_{2sym} & q_{1i} \leq q_1 \leq 0 \\ q_{2sym} + \digamma(q_{2_{target}} - q_{2sym}) & else \end{cases} \tag{7.21}$$

Once the BPLIR is sufficiently close to the line, $\digamma \approx 1$ and $q_{2ref} \approx q_{2_{target}}$; hence the change in reference signal drives the perpendicular distance between the end-effector and the line to zero. The feedback control presented in Chapter 6 ensures that the steady-state position error for link 2 is kept below 10% (see Figure 6.11). The corresponding velocity response, shown in Figure 6.12, shows that the velocity of link 2 converges on zero at the settling time. Consider the end-effector's perpendicular velocity component $\dot{y}$,

$$\dot{y} = (l_1 sin(q_1) + l_2 sin(q_1 + q_2))\dot{q}_1 + l_2 sin(q_1 + q_2)\dot{q}_2 \tag{7.22}$$

Based on the designed step responses for link 2 position (Figure 6.11) and velocity (Figure 6.12), it is a reasonable assumption that the feedback control system drives the system such that $q_2 \approx q_{2ref}$ and $\dot{q}_2 \approx 0$. Hence the perpendicular velocity of the end-effector is approximated by

$$\dot{y} = (l_1 sin(q_1) + l_2 sin(q_1 + q_2))\dot{q}_1 \tag{7.23}$$

If another reasonable assumption is that the BPLIR is symmetrical, i.e. $l_1 = l_2$ and $q_{2ref} \approx q_2 = -q_1$ then the perpendicular velocity to the line $\dot{y}$ is

$$\dot{y} = (sin(q_1) + sin(q_1 - 2q_1))\dot{q}_1 = 0 \tag{7.24}$$

Therefore, for the horizontal case, the system converges on the line at zero velocity.

7.4 Inclined Slopes

The previous sections presented an RTS approach to achieve brachiation on a horizontal structural member. Further path adaption is presented that compensates for the energy loss due to friction. The work of this section presents a heuristic algorithm which can achieve brachiation on an inclined slope of up to 20°.

The main challenge when overcoming the inclined swing is the difference between the initial and final energy of the system. The upward inclined swing starts with lower potential energy than the final configuration. Hence it makes sense to correct for the energy difference by applying maximum torque at the beginning of the swing. The direction of the applied torque is informed by (7.14) to ensure that a positive energy rate is maintained such that,

$$\int_0^T \dot{E}\ dt \geq E_{final} - E_{initial} \tag{7.25}$$

The simulation shows that applying maximum torque during the entire first half of the swing achieved inclined brachiation successfully for up to 20°.

The second half of a swing minimises the perpendicular distance between the end-effector and the inclined line. The switching point is perpendicular to the line, i.e. it shifts with as the line inclines. The generated path interpolates between the minimisation signal and the RTS path signal. The interpolation between the two is like 7.21 whereby the only difference is that the initial part of the swing has the function of pumping energy into the system.

A second task becomes one of calculating an expression for the perpendicular distance to an inclined line. Consider the case of a line inclined by q_{line}, the perpendicular distance to the line y' can be described by

$$y' = -l_1 \cos(q_1 + q_{line}) - l_1 \cos(q_1 + q_{line} + q_2) \tag{7.26}$$

The objective is to minimise the distance between the end-effector and the line i.e. $y = 0$ therefore the reference $q_{2_{ref}}$ becomes

$$q_{2_{ref}} = \arccos(-\frac{l_1}{l_2}\cos q_1 + q_{line}) - q_1 - q_{line} \tag{7.27}$$

The expression (7.27) reduces to (7.18) if the incline of the line is zero.

7.5 Results

This section presents the results for two test cases, namely the horizontal swing test and the inclined swing test. The swings utilise the framework developed in Section 7.2, 7.3 and 7.4. The resulting trajectories shown below in Figure 7.5 which depicts the animation for a horizontal swing and Figure 7.6 where the system response is detailed further.

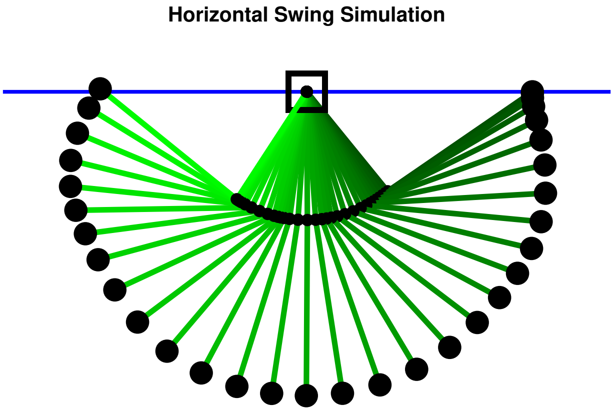

Figure 7.5: Animation (right to left) of simulation results for a horizontal swing with uncertain friction parameters

The animation shown in Figure 7.5 shows the complete brachiation manoeuvre for the BPLIR in the context of a horizontal swing. This is the result of plotting the time series of the angular position shown in Figure 7.6 (top-left) using MATLAB.

Figure 7.6 details the time series of the angular position (top-left), Angular rate (top-right), Applied torque (middle-left), torque disturbance (middle-right), displacement in Cartesian coordinates (bottom-left) and the total system energy (bottom-right). The angular position response in the top-left and the displacement response shows that the total time for a horizontal swing is approximately 1.5s. It can be seen in the displacement

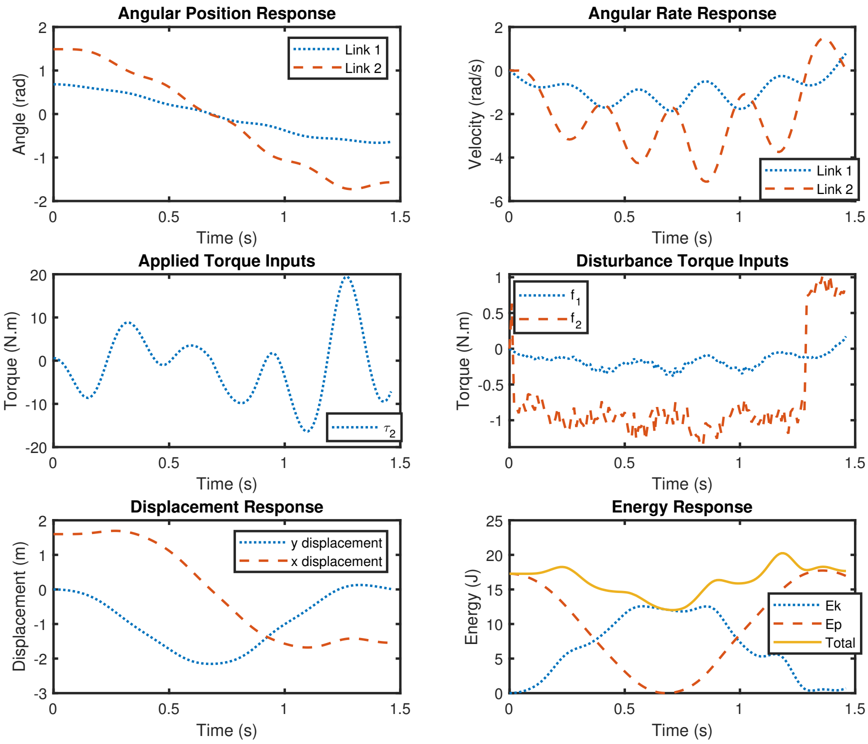

Figure 7.6: Simulation results illustrating adaptive trajectory generation with uncertain friction parameters for a horizontal swing, (top-left) depicts the angular position for both links, (top-right) shows the angular rate of both links, (middle-left) illustrates the applied torque of the BPLIR along the trajectory, (middle-right) shows the uncertain friction torques along the trajectory, (bottom-left) shows the Cartesian displacement and finally (bottom-right) shows the total system energy and a decomposition into kinetic and potential energy. ($1\ rad \approx 58°$)

response (bottom-left) that the y-component of the displacement is zero at the start and end of the swing and that the x-component shows that the x-component is negated by the end of the swing.

The applied torque (middle-left) and energy response (bottom-right) show that the energy of the system is increased towards the end of the swing due to an increase in the applied torque. This change in torque applied corresponds to the switch in trajectory objectives from maintaining RTS to minimising the vertical distance between the power line. The disturbance torques or friction (middle-right) apply a non-conservative force on the system throughout the swing resulting in a steady drop in total energy for the first half $t \leq 0.7$. However, despite a drop in energy, the system recovers in the second half of the swing without reaching the torque limit of 20Nm.

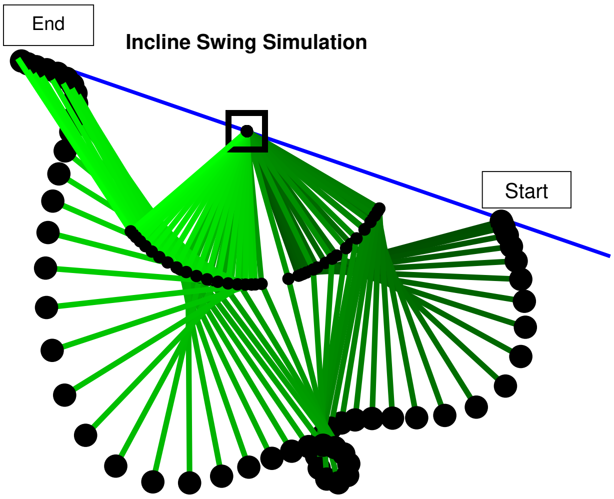

Figure 7.7: Animation illustrating brachiation on an inclined slope with an incline of 20°

The animation in Figure 7.7 and response curves in Figure 7.8 show the detail of an inclined swing. Similarly to the horizontal swing case shown above, the animation should be interpreted from right to left, starting at the point of lower potential energy. The animation shows that for the first half of the swing the BPLIR does not have a smooth movement as in the horizontal case. This is due to an energy pumping stage whereby the total energy of the system is progressively increased until the controller can switch to minimising the perpendicular distance to the power line. A key observation for this animation is the "hang-time" once the end-effector reaches the power line corresponding to the controller driving the perpendicular distance to zero.

Figure 7.7 details the time series for the inclined swing animation shown in Figure 7.7. The angular position (top-left) and velocity response (top-right) show the oscillation in joint angles for the first half or "energy-pumping" phase of the swing before switching when $t \approx 1s$ to minimising the perpendicular distance between the line and the end-effector. Also, the torque response (middle-left) shows the advantage of the AWBT framework whereby the control action (unbounded) does not deviate beyond the 20Nm mark for sustained periods. Instead, the control effort "tracks" the torque limit which improves the performance of the overall system. Lastly, the displacement response illustrates how the end-effector has effectively negated the initial y-displacement by the end of the swing i.e. the final y-displacement is the opposite of where the BPLIR started. This negation of the y-displacement is a direct result of the system progressively pumping energy and increasing the overall energy of the system resulting in a much higher

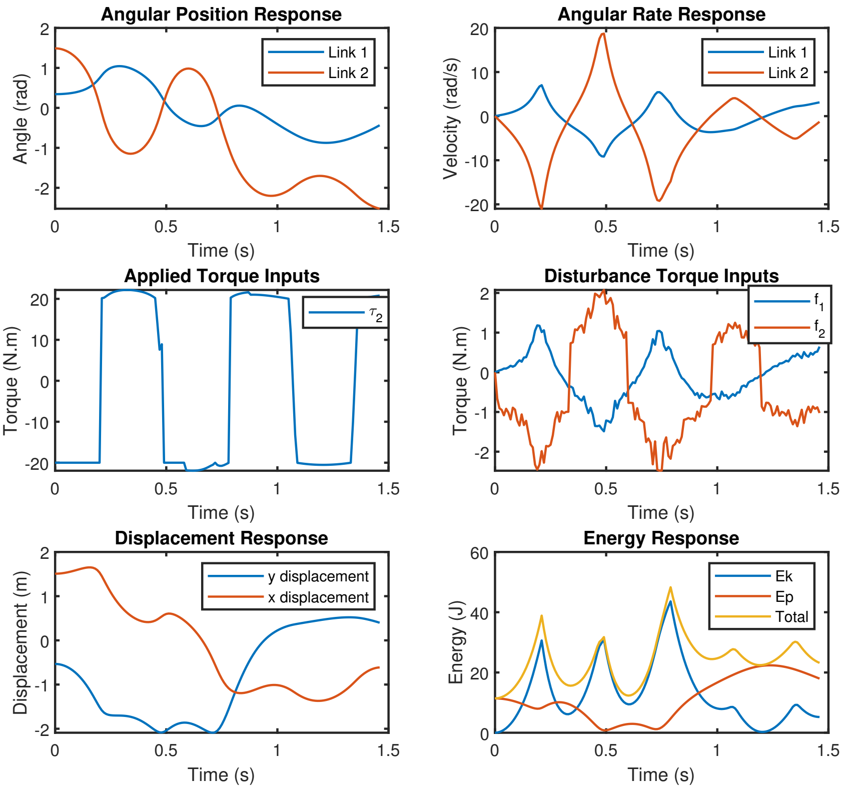

Figure 7.8: Simulation results illustrating adaptive trajectory generation with uncertain friction parameters for an incline of 20°. The graphs depict the angular position (top-left), angular rate (top-right), applied elbow torque (middle-left), friction torques (middle-right), the Cartesian displacement (bottom-left) and the energy of the system (bottom-right) over time. The end-point shows that driving the perpendicular distance to the line to zero results in the PLIR maintaining contact with the line for longer. ($1\ rad \approx 58^{\circ}$)

potential energy by the end of a swing.

7.6 Discussion

This chapter has presented two ways in which to generate a horizontal and inclined swing trajectory for a BPLIR. These trajectories were converted into paths to mitigate the effects of friction on the system. Later in the chapter, an adaptive framework was presented that adjusts the path online to ensure the perpendicular distance between the end-effector and the line converges to zero despite uncertain friction parameters. The tolerance to uncertain friction is demonstrated by the fact that the control system assumed the system to be frictionless. However, the actual friction parameters were varied by random generators on the simulation model by up to 20%.

The results shown in Figure 7.6 illustrate the method of path adjustment reduces the distance to the ceiling for the BPLIR in the second half of the swing. The perpendicular distance adjustment (between end-effector and line) in tandem with an RTS path accomplished a bump-less reference signal q_{2ref}. This continuous reference is particularly crucial for the BPLIR because there are input torque constraints on the motor which oppose any dramatic changes in torque.

The only drawback of the proposed approach is that it assumes that there is enough clearance between the obstacle and the end-effector. It is heavily reliant on the RTS aspect to put the end-effector beyond the obstacle before minimising the perpendicular distance between the line and the end-effector.

The required torque signal for the inclined brachiation is not practical for the prototype hardware. It is impractical because the required motor power from the simulation is a peak of 400W, while the motor is rated for 220W. The proposed framework did not take into consideration the power rating of the prototype.

7.7 Conclusions

This chapter presented a framework that accomplishes horizontal and inclined brachiation of the BPLIR. The proposed framework can generate a feasible path that ensures that the end-effector reaches the line through a combination of RTS and minimisation of the perpendicular distance to the line.

There were limitations on the proposed framework to anticipate constraints on the motor ratings. The constraints affect the practicality of performing inclined swings using the current hardware. Also, the amount of clearance between the obstacle is not considered but assumed to be adequate based on the symmetric nature of the path. This approach is not advised for the commercial BPLIR and stems from the underactuated nature of the system.

In future work, the proposed method can incorporate nonlinear trajectory optimisation to handle inclined swings which are essential for the commercial application of the BPLIR. Alternatively, the prototype can be adapted to incorporate a more powerful motor.

Chapter 8

Results

System integration is the process of integrating all the physical and virtual components of a mechatronic system. The previous chapters presented the state estimator, trajectory generator and the robust controller. Each of the above-mentioned chapters focused on robust design of the subsystems and the current chapter will integrate them to perform a robust brachiation swing.

The state estimator, presented in chapter 5, uses the kinematic system model and a Kalman filter to determine the system state. It was shown that the estimator is tolerant of non-zero initial conditions.

The robust controller presented in Chapter 6 , incorporates partial feedback linearisation in the inner-loop and proposes a robust feedback controller and pre-filter on the outer-loop. Simulation result showed that the controller is robust for all plant variations and this will be tested in the practical system.

The trajectory generator or path planner in Chapter 7 parameterised the path of link 2 based on the dynamics of link 1. The effects of friction were explored and found that friction impedes the motion of link 1. Since the reference for link 2 is paramterised on link 1, an adaptive algorithm was proposed to compensate for the friction.

This chapter presents the results for a brachiation manoeuvre which is performed on a horizontal structural member. The aim of the manoeuvre is for the final configuration to mirror the initial configuration of the BPLIR. Hence the obstacle avoidance algorithm is to initialise the BPLIR in a configuration which, when mirrored, overcomes the obstacle on the line.

Figure 8.1 shows the laboratory environment when the brachiation tests were being performed. The frames run sequentially from left to right and from top to bottom. In frame 1 (top-left), the BPLIR is initialised on the line, this is done by hoisting the BPLIR

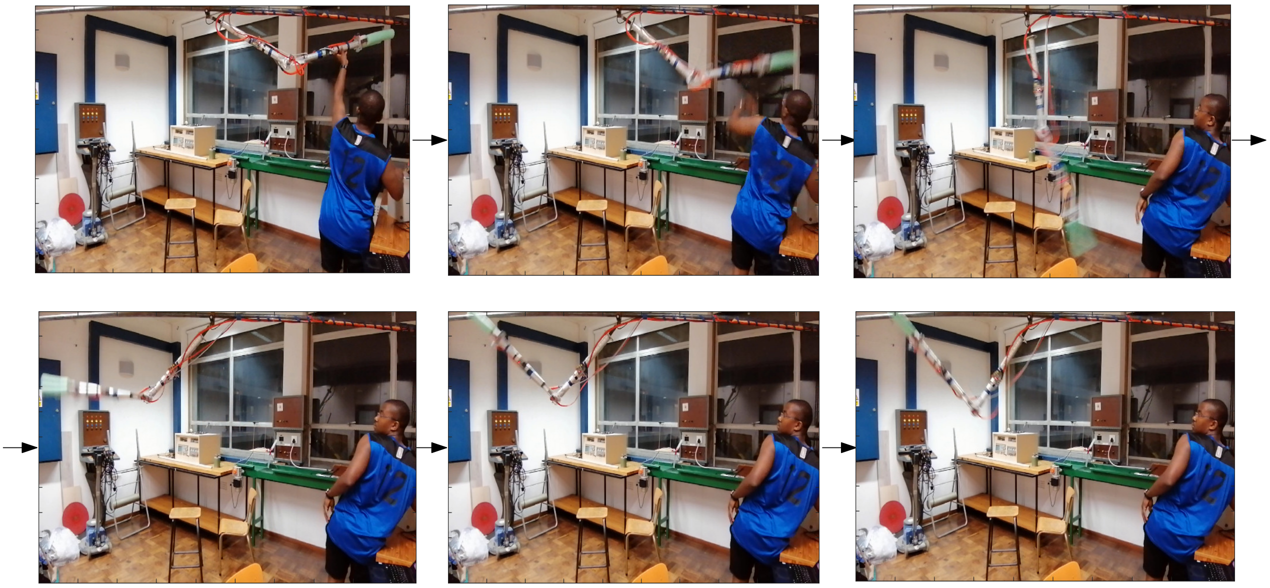

Figure 8.1: Snapshots of the BPLIR prototype performing horizontal brachiation in the laboratory

up to the same level of the line through the use of a nylon cable. Once initialised, frame 2 (middle-top) demonstrates how the brachiation sequence was initiated by simultaneously releasing the cable used to hoist the BPLIR and activating a press-button to signal to the microcontroller which in turn activates the elbow motor, control system and trajectory generator. Frames 5 to 6 detail the full horizontal brachiation manoeuvre and the corresponding measurements from the system are illustrated below in Figure 8.2.

The results in Figure 8.2 show the trajectory of the trajectory over time of the BPLIR in the lab vs a simulation with similar initial conditions on MATLAB. Additionally, the animated reconstruction of the experimental results are depicted in Figure 8.3. The total duration of the brachiation manoeuvre is 1.25s and the laboratory test lines up roughly to the simulation. The profile of the angular position (top-left) show's that the BPLIR reaches the same final configuration as the simulation in the same period however the trajectories do not line up exactly. However the initial and final angular position of the simulation and the laboratory experiment line up.

This misalignment in trajectories is also illustrated in the angular velocity profile (bottom-left) whereby mid swing the BPLIR's velocity continues to increase around 0.5s whereas the simulation has a 'kink' in the velocity. This is mainly attributed to mismatches in the simulation and the laboratory experiment due to the discontinuous nature of friction as detailed in Section 4.3 and the fact that the simulation does not account for the reaction forces applied on the line by the BPLIR and vice-versa. The main themes to call out in the velocity profile of the velocity profile is that the final and initial velocity of both

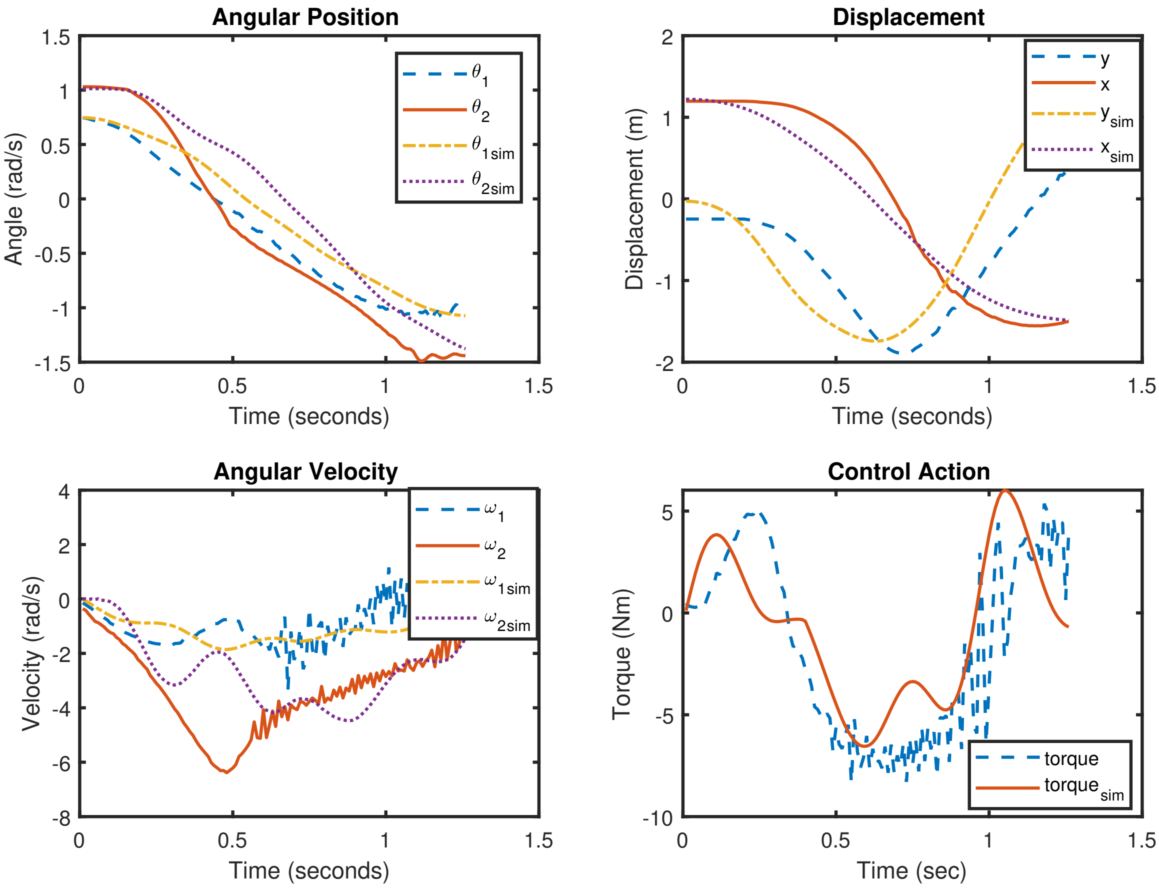

Figure 8.2: Image showing the angular position (top-left), x-y displacement (top-right), angular velocity (bottom-left) and control action (bottom-right) profiles of horizontal brachiation manoeuvre compared to simulations. ($1\ rad \approx 58°$)

the simulation and experiment converge on zero i.e. the BPLIR did not crash into the line.

The control action (bottom-right) follows the same trend whereby the simulation and the experiment have a similar overall profile with a few discrepancies mid-swing. Overall, the control action of the experiment displays high-frequency components, particularly after the $0.5s$ mark. This is not reflected in the simulations due to the smooth functions used to describe the dynamic behaviour of the system and the motor model.

The displacement over time again illustrates the same behaviour or trend between the simulation and the experiment. The trajectory profile mostly lines up for the simulation and the experiment whilst the initial and end displacement line up almost exactly. Again there are some artefacts in the middle of the swing which show some minor examples of plant-model mismatch however the experiment and the simulation results line up to show that successful brachiation was achieved.

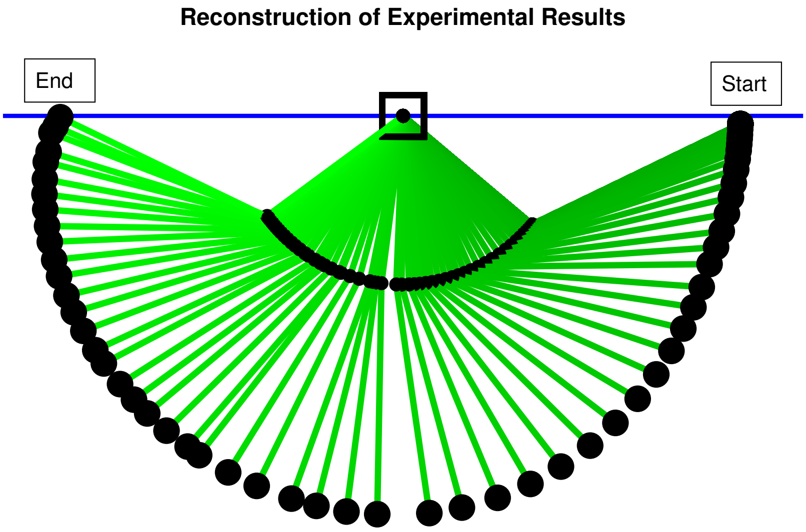

Figure 8.3: Animated reconstruction of angular position from the experimental results for a horizontal swing

Chapter 9

Discussion

The research conducted in this dissertation aimed to explore three research questions. Namely, these were

1. a system to estimate the state of a two-linked brachiating robot using inertial measurement modules
2. a robust trajectory generator which can adjust online to ensure successful brachiation
3. a robust discrete-time controller which can drive the system along a trajectory despite model uncertainty and actuator constraints

These aims culminated in the design of three sub-systems to facilitate successful brachiation. These systems were a state estimator, a robust controller and a trajectory generator. These were developed on MATLAB using a calibrated system model and implemented on an STM32F4. The project used the BPLIR prototype [70] which was the focus of a previous dissertation.

The state estimator presented in Chapter 5 demonstrated the suitability of using a 2D kinematic system model to determine the state variables, namely angular position and velocity. The kinematic modelling approach and the use of IMUs resulted in a filter which is robust to dynamic parameter uncertainty and can measure the absolute angles (w.r.t earth) of the system. The approach is advantageous over rotary encoders which are costlier, suffer from mechanical degradation and only produce relative angular measurements which are not useful for measuring the incline of a high-voltage line.

The results in Section 5.5 showed that the designed state estimator could estimate the system state despite unknown torque disturbances acting on the system. Also, the state estimator was accurate regardless of the initial conditions, which was an improvement over integrating the gyroscope signal. The convergence of the state estimator occurred within a timeframe of five seconds for an error of 1 radian. In this time frame, the filter converges on the optimal error covariance to facilitate successful estimation. The implications for a commercial robot are that a "warm-up" time which must be incorporated before operation of the robot.

A limitation for the filter was the inability to estimate the out-of-plane movement of the prototype because it was designed for a 2D plane. The assumption that the BPLIR operates in a single 2D plane was not correct, especially for the laboratory experiments. The unbalanced motor mounting resulted in lopsided swings out of the plane. Minor bending and swaying at the hinged joint caused misalignment between the gripper and the line. The misalignment contributed to gripper and line collisions and subsequent damage to the experimental setup.

Chapter 6 presented a robust controller designed using QFT techniques. The controller design accounted for actuator saturation, tracking capabilities and input disturbance rejection. An anti-windup framework [25] addressed the issue of actuator saturation in the case of an integral term in the controller. The design accounted for a saturated actuator by placing a maximum bound on the control action required to drive the system to the desired reference point. The lab implementation illustrated in Figures 8.1 and 8.2 showed the controller successfully performing brachiation on a horizontal line without saturating the actuator. Actuator limitations prevented a lab implementation of the inclined swing from being performed.

The trajectory generator in Chapter 7 presented a way to utilise neutral orbits to generate an adaptive path for the BPLIR. A path instead of a trajectory was used because of the unknown time-varying nature of friction hence any dependence on time would be susceptible to failure. The laboratory experiment showcased that the generation of a path using q_1 can overcome the unknown nature of friction. The drawback with this approach is that the zero dynamics of the system may deviate from the expected system response.

The overall performance of the designed control system was satisfactory for a horizontal swing case. It ensured that the BPLIR end-effector reached the target point regardless of friction in the system. The limitations of the approach were that it is dependent on the BPLIR following a neutral or reverse-time symmetrical trajectory which may not always be possible. This vulnerability is especially true if the BPLIR experiences high-frequency torque disturbance which is not approximated as a constant disturbance over the trajectory.

The results presented in Chapter 8 illustrate the discrepancies between the system model and the physical system. The simulated model deviates from the experimental system, particularly for angular velocity curves which are not in sync with the physical model. This is attributed to the simulation model performing aggressive path tracking along the trajectory, which is enabled by the relatively understated and uncertain friction model. This tight trajectory tracking is also seen in Figure 8.2 whereby the simulated angle for link 2 lags behind the experiment.

The under-actuated nature of the BPLIR, although adequate for a single swing, is not the best way forward for a commercial BPLIR. The prototype as subjected to multiple failed tests which reached the target with a misaligned gripper resulting in a crash. The result of these crash tests was that the mechanical integrity (bending and misalignment) of the BPLIR was compromised. The misalignment of the linkages resulted in uncontrollable out-of-plane motion as a result of the single actuator between the links. The uncontrollable out-of-plane swaying is dangerous for the commercial application where it can result in a short-circuit between two phases of the overhead transmission line. The cost implications for such a failure event can be a hindrance to the wide-scale adoption of the technology.

Chapter 10

Conclusion and Recommendations

The research presented a state estimator, controller and trajectory generator for a brachiating power line robot. The research has answered the research questions set out in Section 1.6 as follows:

1. A kinematic state estimator and Kalman filter can estimate the full state of a brachiating robot using low-cost IMUs regardless of uncertain external torques acting on the system
2. A QFT controller and an adaptive path which starts by admitting reverse-time symmetry and subsequently minimising the perpendicular distance to the line can achieve brachiation under uncertain friction conditions.

The state estimator showed, for the 2D case, that the use of low-cost IMUs is viable for estimating the state of the BPLIR prototype. Recommendations are that the state estimator expands to encompass 3D motion. The assumption to model solely 2D motion in this dissertation was incorrect due to the excessive swaying and collisions that occurred due to misalignment of the line and end-effector. The modelling of 3D motion can mitigate against these observed effects of misalignment. It will also aid in the development of BPLIR with additional degrees of freedom. Recommendations are that the kinematic equations be expanded to incorporate 3D motion. The extension to 3D is to model future robots with more degrees of freedom which can perform out-of-plane manoeuvres. Other considerations are an explicit description of the gyroscope drift and bias in the Kalman filter. This will increase the reliability of the filter over long operational distances and aid the marketability of a long-distance autonomous robot.

The QFT approach to controller design in conjunction with collocated feedback linearization proved robust to model perturbation. The robustness is illustrated in the Results presented in Chapter 8 whereby the controller did not incorporate an explicit definition of the friction. It is recommended that the BPLIR be designed with more degrees of freedom. Although successful brachiation was achieved, it is difficult to control the underactuated BPLIR using only a wrist motor. The out-of-plane swaying is an example of the uncontrolled manoeuvres that can result in severe failure modes for the commercial robot. Also, the operating environment will require that the BPLIR be able to do controlled out-of-plane manoeuvres in response to the power line infrastructure. Another consideration is the use of a small wrist (fixed gripper) torque to aid the elbow (between the links) motor during a brachiation manoeuvre.

The trajectory generator showed that it is possible to generate a trajectory online which would achieve the task of brachiation on a horizontal and inclined power line. The benefit was that the trajectory generator is adaptive in the sense that it can drive the BPLIR from an arbitrary start point to an endpoint online. Although successful in simulation and experiment, the trajectory generator can be improved by incorporating online optimisation or the trajectory. The decreasing cost and increasing computational power of micro-controllers suggest that in future online optimisation may be practical on a micro-controller. Nonlinear optimisation techniques and online model calibration can offer a performance improvement for the BPLIR. The ability to intelligently generate a feasible trajectory in real-time will ensure that the robot can negotiate complex obstacles. Real-time trajectory generation will boost the reliability and hence commercially viability of the BPLIR.

The experimental results obtained in Chapter 8 provide evidence of the viability of the proposed framework for brachiation. The resultant subsystems are capable of robust state estimation, trajectory generation and control of a brachiating robot with uncertain parameters. Recommendations for the laboratory experiment is that the size of the BPLIR prototype is reduced. The reduction in size can speed up algorithm implementation cost through a reduction of development costs. During testing, the BPLIR experienced a large number of crashes and failed brachiation which resulted in damage to the original gripper. Additionally, the twisting and bending at the joints resulted in misaligned swings. Scaling the prototype down using additive manufacturing technologies (3D printing) will reduce the time-cost of development. Strength can be improved by reinforcement with metal rods through the manufactured 3D parts. The reduction in size will also allow the use of a smaller motor to test inclined swing a manoeuvres which currently requires large torques and easily adjustable line infrastructure.

Appendix A

Appendix

A.1 Acrobot Dynamic Model Derivation

This section derives the standard manipulator equations using the Euler-Lagrange formulation. The Lagrangian (L) comprises of the system's kinetic energy ($T(\mathbf{q}, \dot{\mathbf{q}})$) and potential energy ($V(\mathbf{q})$) such that

$$L = T(\mathbf{q}, \dot{\mathbf{q}}) - \mathbf{V}(\mathbf{q}) \tag{A.1}$$

The Lagrangian is used in (A.2) to find the dynamic equations of the system where Φ_i represents the generalised external forces acting on the system.

$$\frac{d}{dt}\Big(\frac{\partial L}{\partial \dot{q}_i}\Big) - \frac{\partial L}{\partial q_i} = \Phi_i \tag{A.2}$$

The first step is to find the energy of the system in terms of the generalised coordinates. It is convenient to represent the coordinate system in rectangular coordinates for this purpose, hence

$$\begin{aligned}
x_1 &= l_{c_1} s_1, & \dot{x_1} &= l_{c_1} c_1 \dot{q}_1 \\
y_1 &= -l_{c_1} c_1, & \dot{y_1} &= l_{c_1} s_1 \dot{q}_1 \\
x_2 &= l_1 s_1 + l_{c_2} s_{12}, & \dot{x_2} &= l_1 c_1 \dot{q}_1 + l_{c_2} c_{12}(\dot{q}_1 + \dot{q}_2) \\
y_2 &= -l_1 c_1 - l_{c_2} c_{12}, & \dot{y_2} &= l_1 s_1 \dot{q}_1 + l_{c_2} s_{12}(\dot{q}_1 + \dot{q}_2)
\end{aligned} \tag{A.3}$$

The kinetic energy of the system is given by the rotational energy and translational energy of the system,

$$\begin{aligned}T(\mathbf{q},\dot{\mathbf{q}}) &= \frac{1}{2}m_1(\dot{x}_1^2+\dot{y}_1^2)+\frac{1}{2}I_1\dot{q}_1^2+\frac{1}{2}m_2(\dot{x}_2^2+\dot{y}_2^2)+\frac{1}{2}I_2(\dot{q}_1+\dot{q}_2)^2 \\ &= \frac{1}{2}m_1(l_{c_1}\dot{q}_1)^2+\frac{1}{2}I_1\dot{q}_1^2+\frac{1}{2}I_2(\dot{q}_1+\dot{q}_2)^2+\frac{1}{2}m_2(l_1\dot{q}_1)^2+\frac{1}{2}m_2(l_{c_2}(\dot{q}_1+\dot{q}_2))^2 \\ &\quad + m_2l_1l_{c_2}\dot{q}_1(\dot{q}_1+\dot{q}_2)c_2\end{aligned} \tag{A.4}$$

And the potential energy is given by

$$V(\mathbf{q}) = -m_1gl_{c_1}c_1 - m_2g(l_1c_1+l_{c_2}c_{12}) \tag{A.5}$$

The solution to (A.2) will be solved by focusing on each link individually starting with link 1.

$$\frac{\partial L}{\partial \dot{q}_1} = m_1l_{c_1}^2\dot{q}_1 + I_1\dot{q}_1 + I_2(\dot{q}_1+\dot{q}_2) + m_2l_1^2\dot{q}_1 + m_2l_{c_2}^2(\dot{q}_1+\dot{q}_2) + m_2l_1l_{c_2}(2\dot{q}_1+\dot{q}_2)c_2 \tag{A.6}$$

$$\begin{aligned}\frac{d}{dt}\Big(\frac{\partial L}{\partial \dot{q}_1}\Big) &= m_1l_{c_1}^2\ddot{q}_1 + I_1\ddot{q}_1 + I_2(\ddot{q}_1+\ddot{q}_2) + m_2l_1^2\ddot{q}_1 + m_2l_{c_2}^2(\ddot{q}_1+\ddot{q}_2) \\ &\quad + m_2l_1l_{c_2}(2\ddot{q}_1+\ddot{q}_2)c_2 - m_2l_1l_{c_2}(2\dot{q}_1\dot{q}_2+\dot{q}_2^2)s_2\end{aligned} \tag{A.7}$$

$$\frac{\partial L}{\partial q_1} = -m_1gl_{c_1}s_1 - m_2g(l_1s_1+l_{c_2}s_{12}) \tag{A.8}$$

Combining the above (A.7)(A.8) using (A.2) and grouping like terms results in the dynamic equations of link 1 (A.9). Since no external forces act on link 1 the external fores are zero hence,

$$\begin{aligned}0 &= \ddot{q}_1(m_1l_{c_1}^2 + I_1 + I_2 + m_2l_1^2 + m_2l_{c_2}^2 + 2m_2l_1l_{c_2}c_2) + \ddot{q}_2(I_2 + m_2l_{c_2} + m_2l_1l_{c_2}c_2) \\ &\quad - m_2l_1l_{c_2}(2\dot{q}_1\dot{q}_2+\dot{q}_2^2)s_2 + m_1gl_{c_1}s_1 + m_2g(l_1s_1+l_{c_2}s_{12})\end{aligned} \tag{A.9}$$

The same procedure is followed for link 2,

$$\frac{\partial L}{\partial \dot{q}_2} = I_2(\dot{q}_1+\dot{q}_2) + m_2l_{c_2}^2(\dot{q}_1+\dot{q}_2) + m_2l_1l_{c_2}\dot{q}_1c_2 \tag{A.10}$$

$$\frac{d}{dt}\Big(\frac{\partial L}{\partial \dot{q}_2}\Big) = I_2(\ddot{q}_1+\ddot{q}_2) + m_2l_{c_2}^2(\ddot{q}_1+\ddot{q}_2) + m_2l_1l_{c_2}\ddot{q}_1c_2 - m_2l_1l_{c_2}\dot{q}_1s_2\dot{q}_2 \tag{A.11}$$

$$\frac{\partial L}{\partial q_2} = -m_2l_1l_{c_2}\dot{q}_1(\dot{q}_1+\dot{q}_2)s_2 - m_2gl_{c_2}s_{12} \tag{A.12}$$

Combining (A.11)(A.12) using (A.2) produces the dynamic equations for link 2 A.13. The external forces acting on the system are the torque at the elbow joint τ_2 hence grouping like terms results in

$$\tau_2 = \ddot{q}_1(I_2 + m_2 l_{c_2}^2 + m_2 l_1 l_{c_2}) + \ddot{q}_2(I_2 + m_2 l_{c_2}^2) - m_2 l_1 l_{c_2} \dot{q}_1 s_2 - m_2 g l_{c_2} s_{12} \tag{A.13}$$

The standard manipulator form for a kinematic chain is given by

$$\mathbf{M}(\mathbf{q})\ddot{\mathbf{q}} + \mathbf{C}(\mathbf{q}, \dot{\mathbf{q}})\dot{\mathbf{q}} + \mathbf{g}(\mathbf{q}) = \boldsymbol{\tau} - \mathbf{f}(\dot{\mathbf{q}}) \tag{A.14}$$

where $\mathbf{M}(\mathbf{q}) \in \mathbb{R}^{\mathbf{nxn}}$ is the inertia matrix, $\mathbf{C}(\mathbf{q}, \dot{\mathbf{q}}) \in \mathbb{R}^{\mathbf{nxn}}$ is the Coriolis matrix, $\mathbf{g}(\mathbf{q}) \in \mathbb{R}^{\mathbf{n}}$ is the gravity vector, $\boldsymbol{\tau} \in \mathbb{R}^n$ denotes the actuation vector and $\mathbf{f}(\dot{\mathbf{q}}) \in \mathbb{R}^n$ represents the velocity dependent disturbance torque vector due friction and other disturbances.

$$\mathbf{M}(\mathbf{q}) = \begin{bmatrix} m_1 l_{c_1}^2 + I_1 + I_2 + m_2 l_1^2 + m_2 l_{c_2}^2 + 2 m_2 l_1 l_{c_2} c_2 & I_2 + m_2 l_{c_2}^2 + m_2 l_1 l_{c_2} c_2 \\ I_2 + m_2 l_{c_2}^2 + m_2 l_1 l_{c_2} & I_2 + m_2 l_{c_2}^2 \end{bmatrix} \tag{A.15}$$

$$\mathbf{C}(\mathbf{q}, \dot{\mathbf{q}}) = -m_2 l_1 l_{c_2} s_2 \begin{bmatrix} \dot{q}_2 & \dot{q}_2 + \dot{q}_1 \\ \dot{q}_1 & 0 \end{bmatrix} \tag{A.16}$$

$$\mathbf{g}(\mathbf{q}) = \begin{bmatrix} m_1 g l_{c_1} s_1 + m_2 g(l_1 s_1 + l_{c_2} s_{12}) \\ m_2 g l_{c_2} s_{12} \end{bmatrix} \tag{A.17}$$

$$\boldsymbol{\tau} = \begin{bmatrix} \tau_1 \\ \tau_2 \end{bmatrix} \tag{A.18}$$

A.2 Code

Find the MATLAB and STM32F4 project code on: `https://github.com/Lindokuhle-Shongwe/BPLIR`

A.3 Electrical Circuit

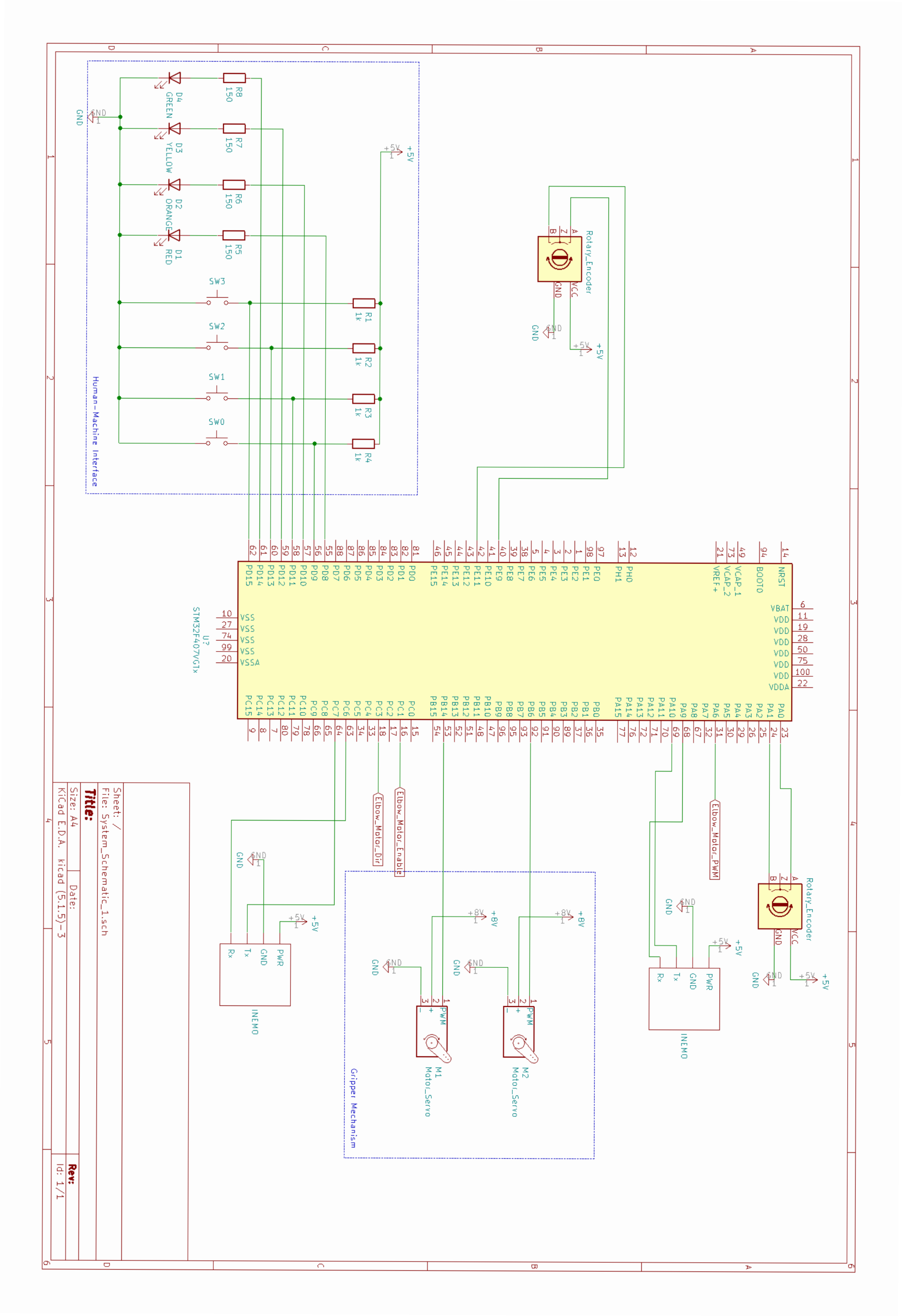

Figure A.1: Circuit diagram of prototype

Bibliography

[1] Harry Nyquist. “Regeneration theory”. In: *Bell system technical journal* 11.1 (1932), pp. 126–147.

[2] Harold S Black. “Stabilized feedback amplifiers”. In: *Bell System Technical Journal* 13.1 (1934), pp. 1–18.

[3] Hendrik W Bode et al. “Network analysis and feedback amplifier design”. In: (1945).

[4] Rudolf Emil Kalman et al. “Contributions to the theory of optimal control”. In: *Bol. soc. mat. mexicana* 5.2 (1960), pp. 102–119.

[5] David G Luenberger. “Observing the state of a linear system”. In: *IEEE transactions on military electronics* 8.2 (1964), pp. 74–80.

[6] Laurence Charles Ward Dixon. “Nonlinear optimisation”. In: (1972).

[7] Duncan Dowson. *History of tribology*. Addison-Wesley Longman Limited, 1979.

[8] Isaac Horowitz. “Quantitative feedback theory”. In: *IEE Proceedings D (Control Theory and Applications)*. Vol. 129. 6. IET. 1982, pp. 215–226.

[9] Holger Preuschoft. “Biomechanics of brachiation”. In: *The Lesser Apes.* (1984), pp. 96–118.

[10] Marc H Raibert. *Legged robots that balance*. MIT press, 1986.

[11] O Yaniv and I Mt Horowitz. “A quantitative design method for MIMO linear feedback systems having uncertain plants”. In: *International Journal of Control* 43.2 (1986), pp. 401–421.

[12] Michael Zeitz. “The extended Luenberger observer for nonlinear systems”. In: *Systems & Control Letters* 9.2 (1987), pp. 149–156.

[13] Russell L Andersson. *A Robot Ping-pong Player: Experiment in Real-time*. MIT Press, 1988.

[14] J Birk and M Zeitz. “Extended Luenberger observer for non-linear multivariable systems”. In: *International Journal of Control* 47.6 (1988), pp. 1823–1836.

[15] Barry W Boehm. “A spiral model of software development and enhancement”. In: *Computer* 5 (1988), pp. 61–72.

[16] Hugh F Durrant-Whyte. “Uncertain geometry in robotics”. In: *IEEE Journal on Robotics and Automation* 4.1 (1988), pp. 23–31.

[17] MW Spong and M Vidyasagar. *Dynamics and Control of Robot Manipulators.* 1989.

[18] PJ Campo and M Morari. “Robust control of processes subject to saturation nonlinearities”. In: *Computers & Chemical Engineering* 14.4-5 (1990), pp. 343–358.

[19] Sheng Chen, SA Billings, and PM Grant. “Non-linear system identification using neural networks”. In: *International journal of control* 51.6 (1990), pp. 1191–1214.

[20] John Hauser and Richard M Murray. “Nonlinear controllers for non-integrable systems: The acrobot example”. In: (1990).

[21] Bruno Siciliano. “Kinematic control of redundant robot manipulators: A tutorial”. In: *Journal of intelligent and robotic systems* 3.3 (1990), pp. 201–212.

[22] Toshio Fukuda, H Hosokai, and Yuji Kondo. “Brachiation type of mobile robot”. In: *Fifth International Conference on Advanced Robotics' Robots in Unstructured Environments.* IEEE. 1991, pp. 915–920.

[23] SABS Chen and SA Billings. “Neural networks for nonlinear dynamic system modelling and identification”. In: *International journal of control* 56.2 (1992), pp. 319–346.

[24] Brian Armstrong-Hélouvry, Pierre Dupont, and Carlos Canudas De Wit. “A survey of models, analysis tools and compensation methods for the control of machines with friction”. In: *Automatica* 30.7 (1994), pp. 1083–1138.

[25] Mayuresh V Kothare et al. “A unified framework for the study of anti-windup designs”. In: *Automatica* 30.12 (1994), pp. 1869–1883.

[26] Fuminori Saito, Toshio Fukuda, and Fumihito Arai. “Swing and locomotion control for a two-link brachiation robot”. In: *IEEE Control Systems Magazine* 14.1 (1994), pp. 5–12.

[27] Mark W Spong. “Partial feedback linearization of underactuated mechanical systems”. In: *Proceedings of IEEE/RSJ International Conference on Intelligent Robots and Systems (IROS'94).* Vol. 1. IEEE. 1994, pp. 314–321.

[28] Mark W Spong. “Energy based control of a class of underactuated mechanical systems”. In: *1996 IFAC World Congress.* Citeseer. 1996, pp. 431–435.

[29] Janine M Benyus. *Biomimicry: Innovation inspired by nature.* 1997.

[30] Scott C Brown and Kevin M Passino. “Intelligent control for an acrobot”. In: *Journal of Intelligent and Robotic Systems* 18.3 (1997), pp. 209–248.

[31] Simon J Julier and Jeffrey K Uhlmann. “New extension of the Kalman filter to nonlinear systems”. In: *Signal processing, sensor fusion, and target recognition VI.* Vol. 3068. International Society for Optics and Photonics. 1997, pp. 182–193.

[32] Klaus Schröer, Stephen L Albright, and Michael Grethlein. “Complete, minimal and model-continuous kinematic models for robot calibration”. In: *Robotics and Computer-Integrated Manufacturing* 13.1 (1997), pp. 73–85.

[33] Karl J Åström. “Control of systems with friction”. In: *Proceedings of the Fourth International Conference on Motion and Vibration Control.* 1998, pp. 25–32.

[34] Henrik Olsson et al. “Friction models and friction compensation”. In: *Eur. J. Control* 4.3 (1998), pp. 176–195.

[35] Konrad Reif et al. “Stochastic stability of the discrete-time extended Kalman filter”. In: *IEEE Transactions on Automatic control* 44.4 (1999), pp. 714–728.

[36] Oded Yaniv. *Quantitative feedback design of linear and nonlinear control systems.* Springer Science & Business Media, 1999.

[37] M Abderrahim and AR Whittaker. “Kinematic model identification of industrial manipulators”. In: *Robotics and Computer-Integrated Manufacturing* 16.1 (2000), pp. 1–8.

[38] RK Aggarwal et al. “An overview of the condition monitoring of overhead lines”. In: *Electric Power systems research* 53.1 (2000), pp. 15–22.

[39] Seong-Il Cho and In-Joong Ha. “A learning approach to tracking in mechanical systems with friction”. In: *IEEE Transactions on Automatic Control* 45.1 (2000), pp. 111–116.

[40] Isabelle Fantoni, Rogelio Lozano, and Mark W Spong. “Energy based control of the pendubot”. In: *IEEE Transactions on Automatic Control* 45.4 (2000), pp. 725–729.

[41] Project Management Institute. *A guide to the project management body of knowledge (PMBOK guide).* Vol. 2. Project Management Inst, 2000.

[42] Jun Nakanishi, Toshio Fukuda, and Daniel E Koditschek. “A brachiating robot controller”. In: *IEEE Transactions on Robotics and Automation* 16.2 (2000), pp. 109–123.

[43] Hassan K Khalil. “Nonlinear systems”. In: *Upper Saddle River* (2002).

[44] Mathukumalli Vidyasagar. *Nonlinear systems analysis.* Vol. 42. Siam, 2002.

[45] Edward Boje. “Pre-filter design for tracking error specifications in QFT”. In: *International Journal of Robust and Nonlinear Control: IFAC-Affiliated Journal* 13.7 (2003), pp. 637–642.

[46] Craig Borghesani, Yossi Chait, and Oded Yaniv. "The QFT Frequency domain control design toolbox". In: (2003).

[47] Robert C Michelson and Messam A Naqvi. "Beyond biologically inspired insect flight". In: *von Karman Institute for Fluid Dynamics RTO/AVT Lecture Series on Low Reynolds Number Aerodynamics on Aircraft Including Applications in Emergening UAV Technology* (2003), pp. 1–19.

[48] James R Usherwood and John EA Bertram. "Understanding brachiation: insight from a collisional perspective". In: *Journal of Experimental Biology* 206.10 (2003), pp. 1631–1642.

[49] John EA Bertram. "New perspectives on brachiation mechanics". In: *American journal of physical anthropology* 125.S39 (2004), pp. 100–117.

[50] John Reap, Dayna Baumeister, and Bert Bras. "Holism, biomimicry and sustainable engineering". In: *ASME 2005 International Mechanical Engineering Congress and Exposition.* American Society of Mechanical Engineers Digital Collection. 2005, pp. 423–431.

[51] Donald T Greenwood. *Advanced dynamics.* Cambridge University Press, 2006.

[52] Serge Montambault and Nicolas Pouliot. "LineScout technology: Development of an inspection robot capable of clearing obstacles while operating on a live line". In: *ESMO 2006-2006 IEEE 11th International Conference on Transmission & Distribution Construction, Operation and Live-Line Maintenance.* IEEE. 2006.

[53] Dan Simon. *Optimal state estimation: Kalman, H infinity, and nonlinear approaches.* John Wiley & Sons, 2006.

[54] Charu Makkar et al. "Lyapunov-based tracking control in the presence of uncertain nonlinear parameterizable friction". In: *IEEE Transactions on Automatic Control* 52.10 (2007), pp. 1988–1994.

[55] *(Video) High-Voltage Cable Inspection.* Apr. 2007. URL: `https://www.techeblog.com/video-high-voltage-cable-inspection/`.

[56] X Xin and M Kaneda. "Analysis of the energy-based swing-up control of the Acrobot". In: *International Journal of Robust and Nonlinear Control: IFAC-Affiliated Journal* 17.16 (2007), pp. 1503–1524.

[57] Paulo Debenest et al. "Expliner-Robot for inspection of transmission lines". In: *2008 IEEE International Conference on Robotics and Automation.* IEEE. 2008, pp. 3978–3984.

[58] Jaka Katrasnik, Franjo Pernus, and Bostjan Likar. "New robot for power line inspection". In: *2008 IEEE Conference on Robotics, Automation and Mechatronics.* IEEE. 2008, pp. 1195–1200.

[59] Joseph W Mitchell. “Power lines and catastrophic wildland fire in southern California”. In: *Proceedings of the 11th International Conference on Fire and Materials*. Citeseer. 2009, pp. 225–238.

[60] Russell Tedrake. “6.832 Underactuated Robotics”. In: *Online, Spring* (2009).

[61] Karl Johan Åström and Richard M Murray. *Feedback systems: an introduction for scientists and engineers*. Princeton university press, 2010.

[62] Marcello Calisti et al. “An octopus-bioinspired solution to movement and manipulation for soft robots”. In: *Bioinspiration & biomimetics* 6.3 (2011), p. 036002.

[63] Moustapha Doumiati et al. *Vehicle dynamics estimation using Kalman filtering: experimental validation*. John Wiley & Sons, 2012.

[64] Trevor Lorimer and Ed Boje. “A simple robot manipulator able to negotiate power line hardware”. In: *2012 2nd International Conference on Applied Robotics for the Power Industry (CARPI)*. IEEE. 2012, pp. 120–125.

[65] Sachin C Patwardhan et al. “Nonlinear Bayesian state estimation: A review of recent developments”. In: *Control Engineering Practice* 20.10 (2012), pp. 933–953.

[66] Henry W Stone. *Kinematic modeling, identification, and control of robotic manipulators*. Vol. 29. Springer Science & Business Media, 2012.

[67] Michael Bloesch et al. “State estimation for legged robots-consistent fusion of leg kinematics and IMU”. In: *Robotics* 17 (2013), pp. 17–24.

[68] Alberto Isidori. “The zero dynamics of a nonlinear system: From the origin to the latest progresses of a long successful story”. In: *European Journal of Control* 19.5 (2013), pp. 369–378.

[69] Katherine Fu et al. “Bio-inspired design: an overview investigating open questions from the broader field of design-by-analogy”. In: *Journal of Mechanical Design* 136.11 (2014), p. 111102.

[70] Javaad Patel and Edward Boje. “Brachiating power line inspection robot”. In: *Proceedings of the 2014 3rd International Conference on Applied Robotics for the Power Industry*. IEEE. 2014, pp. 1–6.

[71] M Cianchetti et al. “Bioinspired locomotion and grasping in water: the soft eight-arm OCTOPUS robot”. In: *Bioinspiration & biomimetics* 10.3 (2015), p. 035003.

[72] Callen Fisher. “State estimation of a cheetah spine and tail using an inertial sensor network”. University of Cape Town, 2015.

[73] Javaad Patel. “Design, modelling and control of a brachiating power line inspection robot”. University of Cape Town, 2016.

[74] Edward Boje. *Lecture notes in Quantitative Feedback Theory (QFT) design.* Feb. 2017.

[75] Matthew P Kelly. "Transcription Methods for Trajectory Optimization: a beginners tutorial". In: *arXiv preprint arXiv:1707.00284* (2017).

[76] *Video of Brachiating Orangutan.* Aug. 2018. URL: `https://twitter.com/DodgerAmes/status/1033443308004143105`.

[77] Norman S Nise. *Control systems engineering.* John Wiley & Sons, 2020.

[78] *iNemo M1.* URL: `http://www.st.com/web/en/resource/technical/%20document/datasheet/DM00056715.pdf`.

[79] *Matrice 200 Series: Increased Aerial Efficiency - DJI.* URL: `https://www.dji.com/matrice-200-series`.

[80] *The key to transmission: worldwide trends.* URL: `http://www.growthmarkets-power.com/features/featurethe-key-to-transmission-worldwide-trends-4622437/`.